DIRECT AND INVERSE PROBLEMS FOR TRANSPORT IN HIGH CONTRAST MEDIA

A DISSERTATION
SUBMITTED TO THE PROGRAM
IN SCIENTIFIC COMPUTING AND COMPUTATIONAL MATHEMATICS
AND THE COMMITTEE ON GRADUATE STUDIES
OF STANFORD UNIVERSITY
IN PARTIAL FULFILLMENT OF THE REQUIREMENTS
FOR THE DEGREE OF
DOCTOR OF PHILOSOPHY

By
Liliana Borcea
June 1996

I certify that I have read this dissertation and that in my opinion it is fully adequate, in scope and in quality, as a dissertation for the degree of Doctor of Philosophy.

George C. Papanicolaou
(Principal Adviser)

I certify that I have read this dissertation and that in my opinion it is fully adequate, in scope and in quality, as a dissertation for the degree of Doctor of Philosophy.

James G. Berryman

I certify that I have read this dissertation and that in my opinion it is fully adequate, in scope and in quality, as a dissertation for the degree of Doctor of Philosophy.

George M. Homsy

Approved for the University Committee on Graduate Studies:

Dean of Graduate Studies

Pentru Lucian, Nicu, mama şi tata,
cu toată dragostea.

Abstract

In this thesis we investigate direct and inverse problems for transport in media with strong spatial variability of the electric or hydraulic conductivity, the dielectric permittivity, etc. The mathematical problem is to solve elliptic or hyperbolic partial differential equations with coefficients that take very large and very small values. Both direct and inverse problems for such partial differential equations pose difficult analytical and computational questions.

We introduce a simplified description of transport phenomena in high contrast media that is based on a suitable asymptotic analysis of the partial differential equations in the static and quasistatic approximations. For media with static excitation, the analysis shows that the overall transport properties of the high contrast media are asymptotically like those of a discrete resistor network. For a time harmonic excitation, the asymptotic behavior is described by the transport in a resistor-capacitor network. The analysis is based on recently obtained min-max variational principles and the network approximation is tested numerically and shown to be accurate to within a few percent provided that the local contrast is about 10^2 or *higher*. For media that display high contrast only in some regions and have smoothly varying properties elsewhere, the asymptotic network theory alone does not give an accurate description of the flow. We present a hybrid numerical method that uses the asymptotic solution in the high contrast regions and matches it with the numerically computed flow elsewhere. The method is tested extensively and compared with other numerical schemes.

The static asymptotic network theory is also used in formulating and solving inverse problems for media with strong spatial variability of the electric or hydraulic conductivity. An iterative least-squares method for recovering the asymptotic network of resistors from the boundary data is presented. The algorithm is tested with numerically generated data from several high contrast models and is shown to be successful in recovering the high contrast structure of the conductivity, independently of the initial guess. The conductivity obtained in this step of the inversion is then used as a starting point in a second step that tries to recover details of the conductivity that are not reflected by the resistor network.

Acknowledgements

I would like to express my appreciation and gratitude to my advisor, Professor George Papanicolaou, for his assistance, guidance and enthusiasm. To him I owe more than I can say. He introduced me to very interesting and rewarding projects and helped me all the way through. Working with him has been a great pleasure and privilege and I am looking forward to future collaborations.

My gratitude also goes to Dr. James Berryman for his many constructive comments and constant interest in my work. I was privileged to collaborate with him and learn from his experience and deep insight in the inverse problems field. Last but not least I want to thank him for serving on my dissertation reading committee.

I would also like to thank Professor Gene H. Golub for his warm friendship, constant interest in my academic career and for agreeing to serve on my University oral examination committee.

I thank Professor Joseph B. Keller for taking the time to serve on my oral defense committee and Professor George M. Homsy for serving on both my University oral examination and dissertation reading committees.

To Professor Jon F. Claerbout, for agreeing to be the chairman of my University oral examination committee, I am very thankful.

To Professor Joseph Oliger, for encouraging me to apply to the Scientific Computing and Computational Mathematics Program, I owe a special thank you. I also want to thank Professor Andrew Stuart for his help and friendship throughout the years I spent as a graduate student. Finally, I would like to thank Professor Robert Street for his help during the first year of my studies at Stanford.

Special thanks are due to my friends, Professors Patrick Hamill and Alejandro

Garcia for their constant help and encouragement during my difficult first years in the United States. I also thank my colleagues and friends Eric Boman, Martin Gander, Margot Gerritsen, Eldar Giladi, Margus Grote, Oliver Ernst, Ronnie Sircar and Knut Solna with whom I shared many insightful discussions and good times.

The most influential and important people in my life have always been my family, to whom I would like to express my love and gratitude. To my husband Lucian, without whom I would not be where I am today, thank you for all your love, patience and constant support. To my parents, Felicia and Dumitru, and my brother Nicu, I thank you for your constant love and support.

This work was partially supported by a grant from AFOSR, F49620-94-1-0436 and by the NSF, DMS 9308471. Their support is gratefully acknowledged.

List of commonly used symbols

c	speed of light in vacuum
C	microscopic capacitance
$\overline{C}$	effective capacitance
$\mathbf{e}_1$	unit vector in the x direction
E, $\hat{E}$	electric field and its Fourier transform with respect to time
H, $\hat{H}$	magnetic field and its Fourier transform with respect to time
$\mathbf{j}$	current density
$\mathbf{j}_R, \mathbf{j}_I$	real and imaginary current density
$\overline{R}$	effective resistance
R_s	resistance of a channel formed at a saddle point $\mathbf{x}_s$ of $\rho(\mathbf{x})$
R-C	short for resistor-capacitor
$\overline{Z}$	effective impedance
ε	dielectric permittivity
ϵ	small parameter that controls the contrast
ϕ	electric potential
μ	magnetic permeability
ω	frequency
Ω	computational domain
ρ	microscopic resistance
σ	conductivity

Contents

List of Tables

List of Figures

Chapter 1

Introduction

In many physical problems, such as transport in natural porous media, there is strong spatial variability (high contrast) of properties like the electric or hydraulic conductivity, the dielectric permittivity, etc., even on mesoscopic length scales where some averaging, or homogenization, has been incorporated into the modeling [4, 3]. The research in this thesis deals with direct and inverse problems for transport in high contrast media. Mathematically this means that we have to solve elliptic or hyperbolic partial differential equations with coefficients that take very large and very small values. Both the direct and the inverse problems for such partial differential equations pose difficult analytical and computational questions. We introduce a simplified description of transport phenomena in high contrast media, based on a suitable asymptotic analysis of the partial differential equations, and an inversion algorithm that uses the simplified description to identify the media from boundary measurements.

1 High contrast impedance tomography

Impedance tomography has received a lot of attention recently, in fields like medical imaging and geophysics. This method is a promising, nondestructive imaging tool that can be used in the medical field for detection and diagnosis of diseases. In geophysical applications the principal goal is to obtain images of the subsurface electrical

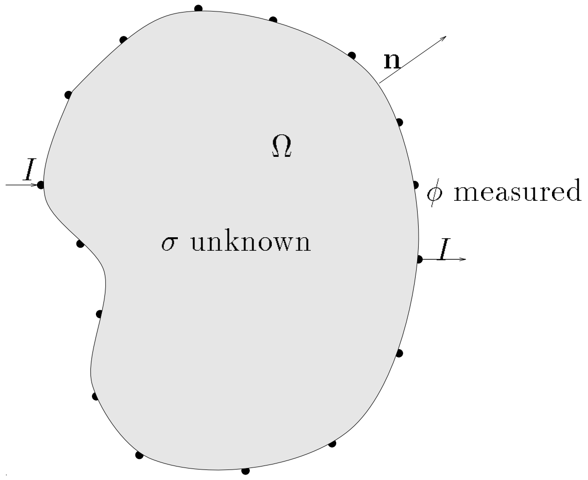

Figure 1.1.1: Tomography problem

conductivity from which important information about the geological structure, rock porosity, fluid saturation, fracture orientation and oil reservoir heterogeneity can be deduced.

1.1 Formulation of the problem

In impedance imaging, or tomography, one seeks to find the internal conductivity (or impedance) profile of a region from boundary measurements of voltages that result from prescribed current fluxes (see fig. 1.1.1). Inside the conducting region Ω there are usually no current sources or sinks so we have

$$\begin{aligned} \nabla \cdot [\sigma(\mathbf{x}) \nabla \phi(\mathbf{x})] &= 0 \quad \text{in } \Omega \\ \sigma(\mathbf{x}) \nabla \phi(\mathbf{x}) \cdot \mathbf{n} &= I(\mathbf{x}) \quad \text{on } \partial\Omega, \\ \int_{\partial\Omega} I ds &= 0 \end{aligned} \tag{1.1.1}$$

where $\sigma(\mathbf{x})$ is the unknown conductivity, $\phi(\mathbf{x})$ is the electric potential, $I(\mathbf{x})$ is the injected current, and $\mathbf{n}$ is the unit outer normal to the boundary. The inverse problem consists of determining $\sigma(\mathbf{x})$ in Ω given the Neumann to Dirichlet map

$$\Lambda(I) = \phi(\mathbf{x}) \mid_{\partial\Omega}, \tag{1.1.2}$$

which is often called the current-to-voltage map because it gives the potential at the boundary for each current distribution I. It is clear that the map between the applied current and the observed voltage depends nonlinearly on the conductivity. Thus, when the conductivity varies over several orders of magnitude, the nonlinearity of the inverse problem is very strong and linearization methods cannot be used.

Under the assumption that the solution of (1.1.1) is in $H^1(\Omega)$, the space of functions over Ω with square integrable gradient, and that the self-adjoint Neumann to Dirichlet map Λ is known ($\Lambda : H^{-1/2}(\partial\Omega) \longrightarrow H^{1/2}(\partial\Omega)$), there have been significant advances on theoretical aspects of the unique determination of σ from Λ as well as its continuous dependence on σ. [2, 42, 52, 70, 71]. The uniqueness question is very important because it tells us that we have enough data to determine the medium. In three or more dimensions, uniqueness was established by Sylvester and Uhlmann [70, 71] for smooth or piecewise smooth conductivities. However, in two dimensions the general uniqueness question remains open. There are some special uniqueness results for the two-dimensional problem when the conductivity σ is almost a constant or a harmonic function [71]. In three or more dimensions, Alessandrini [2] proved a logarithmic type stability estimate based on a-priori bounds in a high Sobolev norm of the conductivity. No such results are available in two dimensions, unless strong assumptions are made on the variability of σ.

All the uniqueness and stability results cited so far assume that the full Neumann to Dirichlet map Λ is known. In applications however, the boundary potential is measured only at discrete locations, where we have electrodes, as shown in fig. 1.1.1. Because of the limited amount of data available we can only hope to recover the unknown conductivity with a limited resolution. Curtis and Morrow [23] considered a discrete medium modeled as a resistor network and showed that, in principle, the resistances can be uniquely identified from the discrete Neumann to Dirichlet map. Their algorithm is, however, unstable and cannot be used in practice.

The reconstruction problem, that is, the identification of the conductivity in Ω from a finite number of measurements at the boundary, has also been studied and significant advances have been made in recent years [9, 64]. However, most imaging methods do not deal with the nonlinearity of the inverse problem and use instead some form of linearization (Born approximation) about a background (usually uniform). They are as follows. A background conductivity distribution σ_b, usually uniform, is assumed and the voltages ϕ_b at the boundary are computed by solving the forward problem. In the Born approximation we assume that the background is close to the actual conductivity

$$\sigma(\mathbf{x}) = \sigma_b(\mathbf{x}) + \delta\sigma(\mathbf{x}), \qquad \text{with } \delta\sigma \ll \sigma_b \tag{1.1.3}$$

so (1.1.1) is linearized to

$$\begin{aligned} \nabla \cdot [\sigma_b \nabla(\phi - \phi_b)] &\approx -\nabla \cdot (\delta\sigma \nabla \phi_b) \quad \text{in } \Omega \\ \sigma_b \nabla(\phi - \phi_b) \cdot \mathbf{n} &= 0 \quad \text{on } \partial\Omega. \end{aligned} \tag{1.1.4}$$

The conductivity perturbation $\delta\sigma$ is estimated iteratively by a linear least-squares approach that minimizes the mean square error between the measured boundary voltage ϕ and the predicted one ϕ_b. This approach requires regularization because the dimension of the solution space is larger than the dimension of the data space (underdetermined problem). Regularization is a well-known technique that goes back to Tikhonov, Levenberg, and Marquardt [72, 56, 59, 60], among others, and is an additional constraint to the least-squares problem. Convergence of the iterative process described above relies heavily on the validity of the assumption (1.1.3). When the conductivity has high contrast and (1.1.3) is not satisfied, the iterative process is generally divergent [73, 57, 4, 38].

While linearization is acceptable in medical imaging applications, it is clearly inappropriate and leads often to erroneous results in geophysical applications, where contrasts in conductivity as high as $O(10^4)$ are not unusual. Berryman [13] introduced an algorithm that deals with the nonlinearity by formulating the inverse problem as a multidimensional nonlinear constrained optimization problem. The inverse problem is formulated so the data are minima of variational principles of physical quantities and so feasibility constraints imposed on the conductivity can be found. Berryman's algorithm produces images that are superior to those of standard, damped least-squares inversion methods but remains limited to contrasts that are not higher than 100%.

Thus, even though there are studies that address the nonlinearity in the unknown parameters of the media [13, 38], the high contrast inversion problem remains open.

In this thesis we address the problem of imaging conductivities that have large contrast and introduce an inversion algorithm that is based on an asymptotic study of the transport properties of such media.

1.2 The high contrast model

Our approach to impedance tomography for high contrast media is based on a high contrast *model* for the conductivity. If, for example, we assume that the medium consists of a smooth background with highly conducting or insulating embedded inclusions, the shape of the inclusions is crucial in the analysis. In inverse problems the shape of the inclusions is unknown so we will assume that the high contrast arises in a generic manner as a continuum and let

$$\sigma(\mathbf{x}) = \sigma_0 e^{-\frac{S(\mathbf{x})}{\epsilon^2}}. \tag{1.1.5}$$

Here σ_0 is a reference constant conductivity, the logarithm of the conductivity $S(\mathbf{x})$ is a smooth function, and ϵ is a small parameter. Small variations of $S(\mathbf{x})$ are amplified by the parameter ϵ, producing logarithmic high contrast for the conductivity. Media with discontinuous conductivity, like ones with inclusions of finite size, can be viewed as particular cases of the generic model (1.1.5). Model conductivities of the form (1.1.5) were used by Kozlov [54] and Golden and Kozlov [36] for continuum percolation models of media with large variations that are exactly solvable in the asymptotic limit of infinitely high contrast.

In chapter 2 we show that when the conductivity has logarithmic high contrast in the form (1.1.5), there is strong channeling of the flow at the saddle points of σ [54, 17]. Moreover, by using variational techniques we show that in the asymptotic limit of high contrast the leading order term of the effective resistance of the medium is obtained by considering transport only in the neighborhood of saddle points of the conductivity. The transport properties of the high contrast medium are then approximated by those of a resistor network, where each resistor is identified from a local analysis in the vicinity of a saddle point of σ. Thus, if there is flow channeling in the medium we are trying to image, there is significant information in the data about the resistor network that approximates the high contrast medium. In the first step of the inversion algorithm proposed in this thesis we attempt to identify the resistor network by looking for the channels of flow. In order to do so we model the conductivity by

$$\sigma(\mathbf{x}) \longrightarrow \sigma_b + \sum_{j=1}^{m} \chi_j(\mathbf{x}, \mathbf{s}_j) f_j(\mathbf{x}, \mathbf{s}_j). \tag{1.1.6}$$

Here σ_b is a uniform background conductivity in which we embed high contrast modules of the form $f_j(\cdot) \sim e^{\frac{-S_j(\mathbf{x})}{\epsilon^2}}$ in the interior of Ω. Each high contrast module consists of a saddle point surrounded by two maxima and minima of the conductivity (chapter 3, section 3). The vector of parameters $\mathbf{s}_j$ for each module describes their structure by specifying the position of the saddle points, their orientation, the curvatures at the saddle, the contrast, etc. The modules $f_j(\cdot)$ are localized with the smooth cutoff functions $\chi_j(\cdot)$.

With this parametrization of the model, in the first step of the inversion process we find the optimal set of parameters $\mathbf{s}_j$, $j = 1, \ldots m$ that is consistent with the given boundary data. Since the number of parameters to be determined is typically much smaller than the number of unknown conductivities in a pixel by pixel discretization, introducing the model (1.1.6), parametrized by σ_b and $\mathbf{s}_j$, $j = 1, ..., m$, is a form of regularization of the inverse problem that is well suited to high contrasts.

The resistor network identified in the first step of the inversion algorithm gives only a rough estimate of the conductivity. However, even though this estimate has low resolution, the network gives a very good approximation of the flow inside the medium. In the next step of the inversion we linearize about the conductivity (1.1.6) given by the resistor network and improve the quality of the background of σ. This is a usual Born inversion step.

Network models were used before in tomographic imaging by discretizing the medium into a resistor network. For example, Dines and Lytle [27] approximate the medium by a resistor network obtained from the five-point numerical discretization of Ohm's law for time independent fields and then linearize and recover the unknown, low contrast conductivity. Their approach fails when the conductivity has large variations so that linearization cannot be used. Curtis and Morrow [23] solve a network inverse problem by a marching algorithm from the corners of a square region towards the interior. This does not involve linearization but the marching algorithm is highly unstable, both when the number of resistors is large and when there is high contrast. The inversion algorithm introduced in this thesis is very different from all the previous network approaches. This is because the approximating resistor network comes from the high contrast medium, and the resulting flow concentration, and is different from a direct resistor network representation.

2 Direct problem for transport in high contrast media

While in inverse problems the medium is unknown and has to be recovered from boundary measurements, in forward problems the material properties are given and the goal is to obtain the flow inside with given boundary conditions. Direct problems for transport in high contrast media are important in inversions because they suggest a good way to model the unknown conductivity. Another important application of the forward problem is upscaling or homogenization [45, 11] where we want to calculate the effective transport properties of inhomogeneous materials with high contrast. In this thesis we address the forward problem for media under static or time-harmonic, low frequency excitation and look at how high contrast affects overall transport behavior.

2.1 Overview of previous work

One of the earliest analytical calculations of effective conductivities in high contrast media is due to J.B. Keller [47]. He considered the effective conductivity of a periodic array of perfectly conducting cylinders or spheres that are nearly in contact, in a poorly conducting background. Keller's results were extended by Batchelor and O'Brien [10] to random arrangements of highly conducting grains in, or nearly in, contact with each other and immersed in a connected uniform matrix. These studies show that when the contrast is high and the impurities are packed closely together, transport occurs primarily through small gaps or channels connecting the conducting regions. Such nearly discrete behavior of current flow reduces the calculation of the effective conductivity of the medium to a local problem around the channels of strong flow concentration. Keller [48] studied also current flow in high contrast periodic checkerboard geometries and showed that when computing the effective resistance of the material it is sufficient to analyze the flow concentrated around the corners connecting the conducting regions.

Kozlov [54] studied random two dimensional checkerboard models where the conductivity is assigned the value $\delta \ll 1$ with probability p and the value 1 with probability $1-p$. He showed that when the contrast is very high, $\delta \longrightarrow 0$, the effective conductivity behaves like

$$\overline{\sigma}(p,\delta) = \begin{cases} O(1), & p \in [0, 1-p_c) \\ O(\sqrt{\delta}), & p \in (1-p_c, p_c) \\ O(\delta), & p \in (p_c, 1]. \end{cases} \tag{1.2.7}$$

Here $p_c \approx 0.59$ is the site percolation probability for the square lattice in two dimensions. The model allows two types of connection of the conducting cells that influence the behavior of the effective conductivity $\overline{\sigma}$. In the first type of connection two cells share a common side whereas in the second they share a common side or vertex. Thus, when $p < 1-p_c$ there are infinitely long conducting chains of the first type through which most flow passes so that $\overline{\sigma} = O(1)$. When $1-p_c < p < p_c$ infinite chains of the second type coexist. Flow still passes through the conducting chains but the overall conductivity is determined by that of the corners of the checkerboard which was shown by Keller [48] to be $O(\sqrt{\delta})$. Finally, when p is increased even further the conducting chains become isolated in an insulating matrix and the effective conductivity is $O(\delta)$. Kozlov's results were extended by Berlyand and Golden [12] who showed, using the Keller-Dykhne [48, 28] duality, that $\overline{\sigma} \approx \sqrt{\delta}$ as $\delta \longrightarrow 0$ for all p where corner connections dominate, not just at $p = \frac{1}{2}$. This technique was used for random cellular convection-diffusion in [31].

Kozlov [54] first formulated and analyzed high contrast conductivity problems in a continuum, using variational methods. He considered only simple situations with one region of flow channeling in the medium. The extension of this result to random high contrast conductivities is given in [19].

These studies show that flows in materials with high contrast conductivity concentrate in narrow channels and behave like current through a discrete resistor network. The effective resistance of each resistor is calculated by analyzing the flow in the vicinity of the associated channel. Network or discrete circuit approximations have been used in the past as a heuristic modeling tool for flow in high contrast media. A widely used model for simulating flow in porous media is to treat them as a network of open pores of various sizes and throats of various cross sections that connect the pores [53]. In the limit of low Reynolds number flow, the network becomes equivalent to a linear resistor network since in each throat the linear relationship between the fluid flux and the pressure drop given by Darcy's law is equivalent to Ohm's law. In general, porous media display a wide range of pore and neck sizes through which the fluid flows so one must consider a broad distribution for the local conductivity in the associated network model [53, 35].

Another class of examples are resistor network models of hopping conductivity in amorphous semiconductors. Here random localized or trapping sites (i and j) are connected by conductances σ_{ij} that have a large range of variation. Ambegaokar, Halperin and Langer [6] estimate the effective conductivity of such semiconductors based on a critical path analysis. They proposed that transport in a medium with a broad range of local conductances σ is dominated by a critical value σ_c defined as the smallest conductance such that the set of all bonds of conductance larger than σ_c percolates, or forms a connected cluster (critical path) that spans the medium. Kozlov and Golden [36] examine more carefully the ideas proposed by Halperin et al. [6] for a continuum percolation model of conducting and porous random media, which is exactly solvable in the asymptotic limit of high disorder. They generalize the random checkerboard model in $\mathbb{R}^2$ and their analysis is based on the variational formulation of the effective conductivity and its dual.

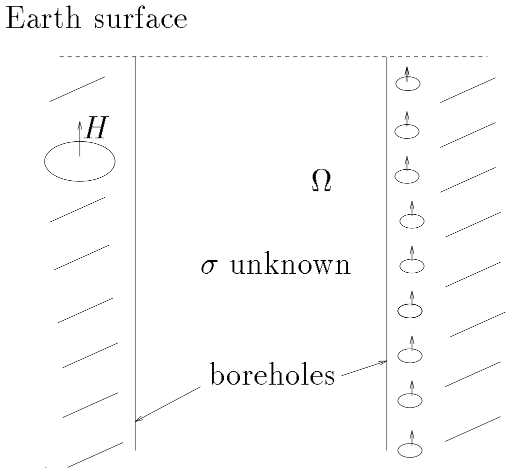

Figure 1.2.2: Experimental setup for electromagnetic induction tomography

2.2 Time harmonic excitation. Electromagnetic induction tomography

In both direct and inverse problems for transport in high contrast media, most analytical work has been done for the static case. However, in many applications time dependent problems are of great interest. In this thesis we consider the forward problem for transport in high contrast media with time-harmonic excitation. When the frequency of the electric and magnetic fields is sufficiently low, we can use a quasistatic approximation which leads to equations like (1.1.1) for complex fields and complex conductivities. The study of high contrast quasistatic transport problem is interesting both from the mathematical and practical point of view. We introduce a new way of using recently discovered saddle-point variational principles [22, 30] to compute the effective impedance of high contrast dielectric media. The only results known so far about the bulk effective parameters of the medium are bounds [62, 33] that diverge from each other when the contrast is very high.

The time-harmonic problem is also important in electromagnetic induction tomography [4, 66]. This is a promising new tool for imaging electrical conductivity in the earth. The excitation consists of a magnetic field $\mathbf{H}$ generated by current through an induction coil in one borehole (see fig. 1.2.2). An array of magnetometers in another borehole measures the small magnetic fields induced in the medium to be imaged. Electromagnetic induction data have been collected at various sites in the US [4, 3] and several studies show that this technique is promising [3, 4, 38]. Inversion of electromagnetic data is a relatively new area and so it is still based on linearization (Born or Rytov approximation) [3, 38, 4], even though the values of the conductivity to be imaged can vary over several orders of magnitude. While a substantial amount of theoretical work has been done for the d.c. (static) conductivity inverse problem (see §1.1), very little is known about the quasistatic electromagnetic inverse problem. Thus, no uniqueness or stability results are available at present.

2.3 Asymptotic analysis of flow in high contrast media

Even though network approximations for transport in high contrast media were used in the past, the mathematical analysis that leads from the continuum to the network was not done. In this thesis we look at how high contrast in material properties affects overall transport behavior and obtain general network approximations using variational principles. We consider Dirichlet-type variational principles for the static approximation and saddle point variational principles [22, 30] for quasistatic transport problems where the equations have complex coefficients. We formulate the effective transport problem as one in the asymptotic analysis of partial differential equations with coefficients that depend exponentially on a large parameter that measures the contrast (see (1.1.5)). For media with static excitation, the analysis shows that the gradients of the solution are large only near narrow channels that connect highly conducting regions. The overall transport properties are asymptotically like those of a discrete resistor network with the resistance of each resistor calculated locally near the channels. When the excitation is time harmonic, the asymptotic analysis shows that the overall transport properties are like those of a discrete resistor-capacitor network. The properties of each network element are again calculated locally in the vicinity of regions of strong flow. The network approximation was tested numerically and shown to be accurate to within a few percent provided that the contrast was about 10^2 or higher.

3 Numerical computations

In general, materials display high contrast in some regions and have smoothly varying properties elsewhere in the flow regime. In such situations, the resistor-capacitor network theory alone does not give an accurate description of the flow. However, the asymptotic results are still useful because they describe quite accurately the flow locally, near the channels. Standard numerical methods cannot resolve the flow in the channels because the potential undergoes abrupt changes in their vicinity. For this reason, we developed a hybrid numerical method that uses the asymptotic form of the solution in the channels along with the numerically computed flow elsewhere. Extensive numerical tests and comparisons with other numerical schemes show that the hybrid method is accurate, efficient and superior to other methods in many situations.

The hybrid method presented in this thesis requires a lot of human input and needs to be automated in order to be used in inversion algorithms. So far we have used it primarily to test the high contrast behavior of the multigrid numerical solver PLTMG (see [7]) that we used in all our inversion computations.

4 Overview

This thesis is organized as follows. In chapter 2 we study the forward problem and present the asymptotic network theory that approximates flow in media with high contrast properties. We introduce variational principles that we use extensively throughout. We present a proof of the validity of the network approximation as well as results of numerical experiments. In chapter 3, we introduce a new algorithm for imaging conductivities that have large variations in magnitude over the domain of interest. We assess carefully its performance with numerous numerical experiments. In chapter 4, we introduce a hybrid numerical method that combines the asymptotic results with the use of standard numerical schemes. We test its performance and compare it with other numerical methods.

Chapter 2

The forward problem

In this chapter we study the transport properties of dielectric conducting media with high contrast. We begin with Maxwell's equations for the electric and magnetic fields and introduce the low frequency, quasistatic approximation that we will use throughout. We then show that the effective complex impedance of materials with conductivity and dielectric permittivity that have high contrast can be calculated approximately by solving a suitable resistor-capacitor network. We use extensively variational principles for the analysis and we assess the accuracy of the network approximation by numerical computations.

1 Formulation of the problem

We consider the system of Maxwell's equations in a domain Ω

$$\begin{aligned} \nabla \times \mathbf{H} &= \sigma \mathbf{E} + \varepsilon \frac{\partial \mathbf{E}}{\partial t} \\ \nabla \times \mathbf{E} &= -\mu \frac{\partial \mathbf{H}}{\partial t} \\ \nabla \cdot (\varepsilon \mathbf{E}) &= 0 \\ \nabla \cdot (\mu \mathbf{H}) &= 0, \end{aligned} \tag{2.1.1}$$

where $\mathbf{H}(\mathbf{x}, t)$ and $\mathbf{E}(\mathbf{x}, t)$ are the magnetic and electric fields, $\sigma(\mathbf{x})$ is the electric conductivity, $\varepsilon(\mathbf{x})$ is the dielectric permittivity, μ is the assumed constant magnetic permeability and we also assume that there are no free charges or current sources in the domain. The electric and magnetic fields have a time harmonic behavior, so they have the form

$$\mathbf{E}(\mathbf{x}, t) = \mathrm{real}(\hat{\mathbf{E}}(\mathbf{x})e^{-i\omega t}), \tag{2.1.2}$$

$$\mathbf{H}(\mathbf{x}, t) = \mathrm{real}(\hat{\mathbf{H}}(\mathbf{x})e^{-i\omega t}), \tag{2.1.3}$$

where ω is the frequency of oscillation. The complex valued field amplitudes $\hat{\mathbf{E}}$ and $\hat{\mathbf{H}}$ satisfy the system

$$\begin{aligned} \nabla \times \hat{\mathbf{H}} &= \sigma\hat{\mathbf{E}} - i\omega\varepsilon\hat{\mathbf{E}} \\ \nabla \times \hat{\mathbf{E}} &= i\omega\mu\hat{\mathbf{H}} \\ \nabla \cdot (\varepsilon\hat{\mathbf{E}}) &= 0 \\ \nabla \cdot (\mu\hat{\mathbf{H}}) &= 0. \end{aligned} \tag{2.1.4}$$

From (2.1.4), the electric field can be expressed in terms of the magnetic field in the form

$$\hat{\mathbf{E}} = (\frac{\sigma}{\sigma^2 + \omega^2\varepsilon^2} + i\frac{\omega\varepsilon}{\sigma^2 + \omega^2\varepsilon^2})\nabla \times \hat{\mathbf{H}}. \tag{2.1.5}$$

The coefficient in (2.1.5) is the complex impedance which consists of a resistance (real part) and a capacitance or capacitive reactance (imaginary part). We use the notation

$$\rho(\mathbf{x}, \omega) = \frac{\sigma}{\sigma^2 + \omega^2\varepsilon^2}, \tag{2.1.6}$$

$$C(\mathbf{x}, \omega) = \frac{\omega\varepsilon}{\sigma^2 + \omega^2\varepsilon^2}, \tag{2.1.7}$$

and from (2.1.4) - (2.1.7) we obtain

$$\nabla \times [(\rho + iC)\nabla \times \hat{\mathbf{H}}] = i\omega\mu\hat{\mathbf{H}}. \tag{2.1.8}$$

The system of equations (2.1.4) takes into account the conducting, dielectric and magnetic properties of the material. If we have a strongly conducting material, then for low frequencies we have $\sigma \gg \omega\varepsilon$ and the dielectric term in (2.1.4) can be neglected. In this case only the magnetic and conducting properties of the material are important. However, if our material is a poor conductor (e.g. glass, semiconductors, etc.), we cannot neglect the dielectric term. Let us consider a dielectric material for which the conductivity σ is of the same order as $\omega\varepsilon$. We see from (2.1.6) and (2.1.7) that both ρ and C are of order $1/\omega\epsilon$. If L is a typical length scale then the right hand side in (2.1.8) can be neglected when

$$\frac{\rho + iC}{L^2} \sim \frac{1}{L^2\omega\varepsilon} \gg \omega\mu. \tag{2.1.9}$$

The dielectric permittivity can be written as $\varepsilon = \varepsilon_0\varepsilon_r$, where ε_0 is the permittivity of free space, and ε_r is the relative permittivity. For dielectrics ε_r is of order one. Similarly, the magnetic permeability can be written as $\mu = \mu_0\mu_r$, where μ_0 is the permeability of free space and μ_r is the relative permeability. As long as our material is not ferromagnetic, the relative permeability is of order one. For example, if we have a diamagnetic material then μ_r is a positive number less than one and with the speed of light in vacuum $c = \frac{1}{\sqrt{\varepsilon_0\mu_0}} \approx 3 \cdot 10^8 \frac{m}{s}$, condition (2.1.9) becomes

$$c^2 \gg \omega^2\varepsilon_r\mu_r L^2. \tag{2.1.10}$$

If the size of the domain is in the range of kilometers, we may take L to be 1 km. We assume that ε_r and μ_r are O(1) and therefore for frequencies up to kHz we can neglect the magnetic properties of such a material and obtain a simplified system of equations which we consider throughout the rest of the chapter:

$$\begin{aligned} \hat{\mathbf{E}} &= (\rho + iC)\nabla \times \hat{\mathbf{H}} \\ \nabla \times \hat{\mathbf{E}} &= 0 \\ \nabla \cdot (\varepsilon\hat{\mathbf{E}}) &= 0 \\ \nabla \cdot (\mu\hat{\mathbf{H}}) &= 0. \end{aligned} \tag{2.1.11}$$

By combining the first two equations in (2.1.11) we also obtain:

$$\nabla \times [(\rho + iC)\nabla \times \hat{\mathbf{H}}] = 0. \tag{2.1.12}$$

In the two-dimensional case, the curl operator $\nabla\times$ is equivalent to the perpendicular gradient operator $\nabla^\perp = (-\partial_y, \partial_x)$ and since $\nabla \times \hat{\mathbf{H}}$ is a current density we use the notation $\nabla \times \hat{\mathbf{H}} = \mathbf{j}(\mathbf{x})$. Equation (2.1.12) becomes therefore

$$\begin{aligned} \nabla^{\perp} \cdot [(\rho + iC)\mathbf{j}] &= 0 \\ \nabla \cdot \mathbf{j} = 0. \end{aligned} \tag{2.1.13}$$

Equations (2.1.12) or (2.1.13) can be used for composite materials with fine scale structure. In this context the microscopic fields can be averaged leading to an effective medium describing the large scale behavior of the material. In materials with periodic structure [11, 45] the effective impedance of the composite can be obtained by solving (2.1.13) over a period cell when the average current over the cell is equal to a unit vector. Even though the method we describe in this chapter is quite general, we will present it in the context of the periodic homogenization problem in two dimensions. Therefore we take

$$< \mathbf{j} >= \mathbf{e}_1, \tag{2.1.14}$$

where $< \mathbf{j} >$ stands for the integral of $\mathbf{j}$ over the domain Ω, normalized by the area of Ω and $\mathbf{e}_j,\ j = 1, 2$ are unit vectors in the coordinate directions. According to (2.1.13) the field $\mathbf{j}$ is divergence free and so it can be expressed as the perpendicular gradient of a complex scalar function $w(\mathbf{x})$, $\mathbf{j}(\mathbf{x}) = \nabla^{\perp} w(\mathbf{x})$. The scalar function $w(\mathbf{x})$ is the component of the magnetic field perpendicular to the plane of the domain Ω (i.e. $\mathbf{H}(\mathbf{x}) = w(\mathbf{x})\mathbf{e}_3$). With this notation the system of equations (2.1.13) becomes

$$\begin{aligned} \nabla^{\perp} \cdot [(\rho + iC)\nabla^{\perp} w] &= 0 \\ < \nabla^{\perp} w > &= \mathbf{e}_1, \end{aligned} \tag{2.1.15}$$

where $\rho(\mathbf{x}), C(\mathbf{x})$, and $\nabla^{\perp} w(\mathbf{x})$ are periodic functions in the domain Ω as shown in fig. 2.1.1. Equations (2.1.15) define the direct cell problem. Independently, by applying the divergence operator to the first equation in (2.1.11), and recalling that $\hat{\mathbf{E}}$ is curl free so that $\hat{\mathbf{E}} = -\nabla\phi$ is the gradient of the potential ϕ, we obtain the dual cell problem:

$$\begin{aligned} \nabla \cdot [\frac{1}{\rho + iC} \nabla \phi(\mathbf{x})] &= 0 \\ < \nabla \phi(\mathbf{x}) > &= \mathbf{e}_1. \end{aligned} \tag{2.1.16}$$

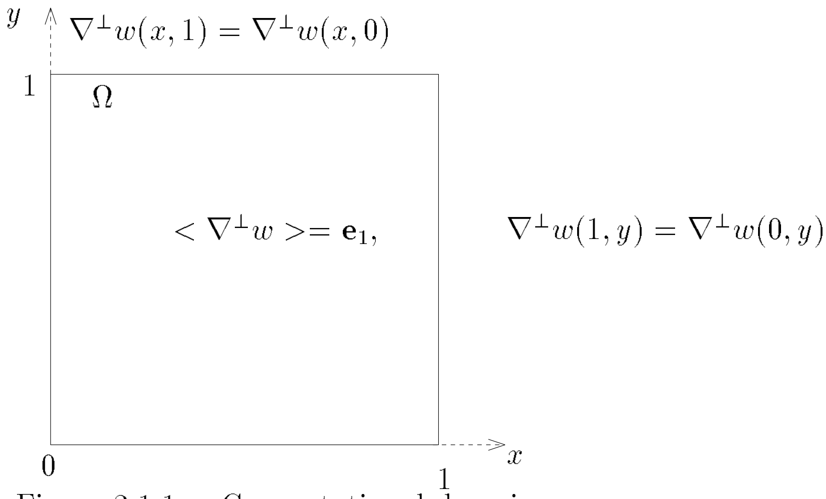

Figure 2.1.1: Computational domain

We will concentrate on the direct problem and rewrite the complex system of equations (2.1.15) as a system of real equations

$$\begin{aligned}
\nabla^\perp \cdot [\rho \nabla^\perp u - C\nabla^\perp v] &= 0 \\
\nabla^\perp \cdot [C\nabla^\perp u + \rho \nabla^\perp v] &= 0 \\
< \nabla^\perp u > &= \mathbf{e}_1 \\
< \nabla^\perp v > &= \mathbf{0},
\end{aligned} \tag{2.1.17}$$

where we separated the function w into its real and imaginary parts $w(\mathbf{x}) = u(\mathbf{x}) + iv(\mathbf{x})$. The system of equations (2.1.17) is elliptic and has a unique solution up to an additive constant if $\rho + C > 0$. It is easily shown [6] that the resistive part (ρ) of the microscopic impedance should always be greater than or equal to zero so that the dissipation energy averaged over a period of oscillations is positive

$$E_{dissip} = \frac{1}{2}\rho(\mid \text{real}(\hat{\mathbf{E}}) \mid^2 + \mid \text{imag}(\hat{\mathbf{E}}) \mid^2) \geq 0. \tag{2.1.18}$$

In our analysis, both ρ and C are greater than or equal to zero, with the constraint that they cannot vanish at the same location in Ω.

The effective impedance associated with the direct problem is computed as the average flux in the direction of the driving

$$\overline{Z} =< (\rho + iC)(\nabla^\perp u + i\nabla^\perp v) \cdot \mathbf{e}_1 > . \tag{2.1.19}$$

From equations (2.1.17) we conclude that the imaginary function v is periodic in Ω, whereas the real function u can be written as $u(\mathbf{x}) = -y + \psi(\mathbf{x})$, where $\psi(\mathbf{x})$ is a periodic function in Ω. The identity $\nabla^\perp \cdot (\phi \mathbf{a}) = \mathbf{a} \cdot \nabla^\perp \phi + \phi \nabla^\perp \cdot \mathbf{a}$, valid for any vector $\mathbf{a}$ and scalar function ϕ, and the periodicity of ρ, C, v, and ψ give

$$\begin{aligned} < (\rho + iC)(\nabla^\perp u + i\nabla^\perp v) \cdot (\nabla^\perp \psi + i\nabla^\perp v) > \;&=\\ < \nabla^\perp \cdot [(\rho + iC)(\nabla^\perp u + i\nabla^\perp v)(\psi + iv)] > - & \\ < (\psi + iv)\nabla^\perp \cdot [(\rho + iC)(\nabla^\perp u + i\nabla^\perp v)] > \;&= \;0. \end{aligned} \tag{2.1.20}$$

Consequently,

$$\overline{Z} =< (\rho + iC)(\nabla^\perp u + i\nabla^\perp v) \cdot (\nabla^\perp u + i\nabla^\perp v) > . \tag{2.1.21}$$

From (2.1.21) we obtain expressions for the effective resistance and capacitive reactance

$$\overline{R} = \mathrm{real}(\overline{Z}) =< \rho \mid \nabla^\perp u \mid^2 > -2 < C\nabla^\perp u \cdot \nabla^\perp v > - < \rho \mid \nabla^\perp v \mid^2 >, \tag{2.1.22}$$

$$\overline{C} = \mathrm{imag}(\overline{Z}) =< C \mid \nabla^\perp u \mid^2 > +2 < \rho\nabla^\perp u \cdot \nabla^\perp v > - < C \mid \nabla^\perp v \mid^2 > . \tag{2.1.23}$$

The real and imaginary part of the effective impedance $\overline{Z}$ can also be obtained by using the following saddle-point variational principles:

$$\begin{aligned} \overline{R} = \min_{<\nabla^\perp u> = \mathbf{e}_1} \max_{<\nabla^\perp v> = \mathbf{0}} (< \rho \mid \nabla^\perp u \mid^2 > -2 < C\nabla^\perp u \cdot \nabla^\perp v > - & \\ < \rho \mid \nabla^\perp v \mid^2 >), & \end{aligned} \tag{2.1.24}$$

$$\begin{aligned} \overline{C} = \min_{<\nabla^\perp u> = \mathbf{e}_1} \max_{<\nabla^\perp v> = \mathbf{0}} (< C \mid \nabla^\perp u \mid^2 > +2 < \rho\nabla^\perp u \cdot \nabla^\perp v > - & \\ < C \mid \nabla^\perp v \mid^2 >) & \end{aligned} \tag{2.1.25}$$

since the Euler equations for (2.1.24) and (2.1.25) coincide with equations (2.1.17). Variational principles of this and related forms were introduced by Gibiansky and

Cherkaev [22] and by Fannjiang and Papanicolaou [30]. A discussion of other variational principles associated with this problem as well as why we chose (2.1.24) and (2.1.25) is given in appendix A.

Our aim in this chapter is to study the behavior of the effective resistance and capacitance when the microscopic resistance and capacitance have logarithmic high contrast behavior. We will model this behavior by assuming that [54]

$$\begin{aligned} \rho(\mathbf{x}) &= \rho_0 e^{-\frac{S(\mathbf{x})}{\epsilon^2}}, \\ C(\mathbf{x}) &= C_0 e^{-\frac{P(\mathbf{x})}{\epsilon^2}} \end{aligned} \tag{2.1.26}$$

where $S(\mathbf{x})$ and $P(\mathbf{x})$ are smooth, periodic functions defined on Ω, ϵ is a small parameter and ρ_0, C_0 are constants which can be viewed as the microscopic resistance and capacitive reactance of a homogeneous reference medium. In the following sections we analyze the behavior of the effective impedance and the current flow in Ω when ρ and C have the form (2.1.26) and ϵ is small. The variational principles (2.1.24) and (2.1.25) play an important role in the analysis.

2 Some basic high contrast problems

To understand better the behavior of the effective impedance in high-contrast composites we will first analyze some simpler problems. This will also explain the physical meaning of the results.

2.1 Effective conductivity of some special two component periodic composites.

In the static case $\omega = 0$, from (2.1.6) and (2.1.7) we have that $\rho(\mathbf{x}) = \frac{1}{\sigma}, C = 0$ and the medium is purely resistive. The direct cell problem (2.1.15) reduces then to

$$\begin{aligned} \nabla^{\perp} \cdot (\rho \mathbf{j}) &= 0 \\ \nabla \cdot \mathbf{j} &= 0 \\ < \mathbf{j} > &= \mathbf{e}_1. \end{aligned} \tag{2.2.1}$$

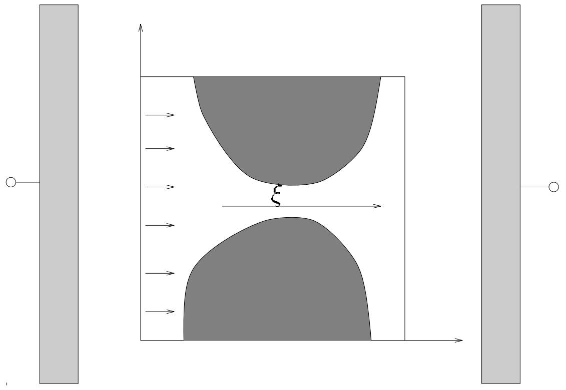

Figure 2.2.2: Flow channeling in a high contrast, two component medium

The current flowing in the domain Ω is real and the effective resistance is

$$\overline{R} = < \rho \mathbf{j} \cdot \mathbf{j} > . \tag{2.2.2}$$

The dual of this problem for the electric potential ϕ has from (2.1.16) the form

$$\begin{aligned} &\nabla \cdot (\sigma \nabla \phi) = 0 \\ &< \nabla \phi >= \mathbf{e}_1, \end{aligned} \tag{2.2.3}$$

with the effective conductivity given by

$$\overline{\sigma} = < \sigma \nabla \phi \cdot \nabla \phi > . \tag{2.2.4}$$

It is well known, and shown in section 2.4.1 for completeness, that $\overline{\sigma} = \frac{1}{\overline{R}}$.

Before attempting to solve this problem in the continuous high contrast case, we study it first for some discontinuous two component composites. We consider problems like the one shown in fig. 2.2.2 where the resistance of the material in the period cell can take only two values ρ_1 (for the black region) and ρ_2 (for the white region). Since we are interested in high contrast, we assume that $\rho_1 \gg \rho_2$. Between the left and right boundaries of the domain, we apply a potential difference $\nabla \Phi$, in the x direction, and study the flow of electric current through the cell. We expect that

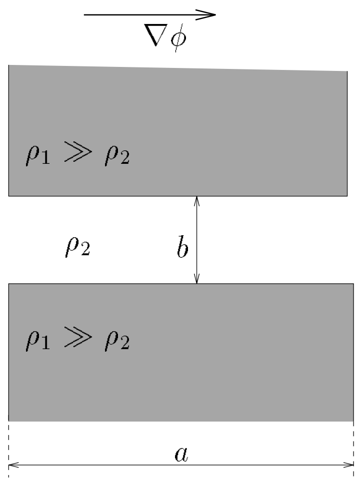

Figure 2.2.3: Current flow in a channel

the current will tend to pass through regions of small resistance. Since we assumed the resistance in the black region (ρ_1) to be very high, the only way the current can pass through the barrier shown in fig. 2.2.2 is by concentrating in the channel near the point ξ. In the rest of the domain, the current will be diffuse in the white region and will be much smaller than its value near the point ξ. It will be negligible in the black region. The effective resistance of this composite is determined by the resistance (R) of the channel. We expect R to decrease if the width of the channel increases or the radius of curvature of the isolating regions decreases. If the width of the channel is b and the radius of curvature of the isolating regions is a, we expect a result of the form $R \approx \rho_2 f(\frac{a}{b})$, where f is a monotone increasing function. At the point ξ we can take the curvature in the y direction to be $k_1 = \frac{1}{b}$ and the curvature in the x direction to be $k_2 = \frac{1}{a}$ and obtain

$$\overline{R} \approx \rho_2 f(\frac{a}{b}) = \rho_2 f(\frac{k_1}{k_2}). \tag{2.2.5}$$

We do not know the exact form of the function $f(\cdot)$ but we expect it to depend on the geometry of the problem. To illustrate (2.2.5) we consider some simple geometries.

We start with the case shown in figure 2.2.3. We have a conducting channel of resistance ρ_2 embedded in an insulating background ($\rho_1 \gg \rho_2$). When we apply a

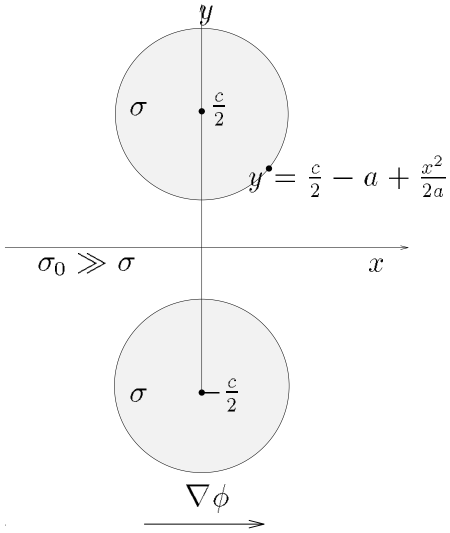

Figure 2.2.4: Insulating cylinders in a conducting background

unit potential difference $\nabla\phi$ between the ends of the channel all the current will flow through it. The electric current density is $\mathbf{j} = \rho_2^{-1}\mathbf{e}_1$ and its average over the domain is $<\mathbf{j}>= \rho_2^{-1}b\mathbf{e}_1$. The effective resistance is computed from (2.2.2)

$$\overline{R} \approx \frac{1}{(b\rho_2^{-1})^2}\int_{-b}^{b}\int_{-\frac{a}{2}}^{\frac{a}{2}} \rho_2(\rho_2^{-1})^2 dxdy = \rho_2\frac{a}{b}. \tag{2.2.6}$$

This result agrees with the heuristic form (2.2.5) if we take the function $f(x) = x$.

The next problem was analyzed by Keller [47]. We consider a periodic array of nonconducting cylinders ($\sigma = 0$) embedded in a conducting uniform background (σ_0)(see fig. 2.2.4). The cylinders have a radius a and their axes are at distance c apart. We assume that an electric field is applied in the x direction and compute the effective resistance of the composite. When the cylinders touch each other it is clear that the effective conductivity is zero so we are interested in the case of a narrow channel (i.e., $b = c - 2a$ small). The electric current concentrates in the channel and the effective resistance is approximately equal to the resistance of the channel. In order to compute $\overline{R}$, we view the gap as a collection of thin vertical slabs connected

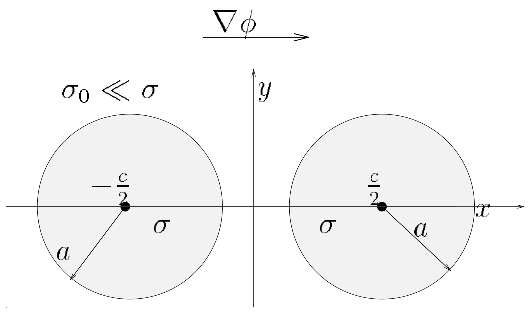

Figure 2.2.5: Conducting cylinders in an insulating background

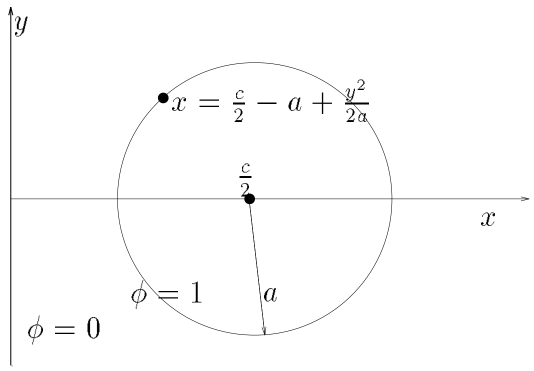

Figure 2.2.6: Enlarged view of the gap between a plane midway between two cylinders and one of the cylinders

in series. The resistance dR of each slab dx is

$$dR = \sigma_0^{-1}\frac{dx}{2y} = \sigma_0^{-1}\frac{dx}{2(\frac{c}{2} - a + \frac{x^2}{2a})}$$

and by integrating we have

$$\overline{R} \approx \sigma_0^{-1}\int_{-c}^{c}\frac{dx}{2(\frac{c}{2} - a + \frac{x^2}{2a})} \approx \sigma_0^{-1}\pi\sqrt{\frac{a}{c-2a}} = \sigma_0^{-1}\pi\sqrt{\frac{a}{b}}, \tag{2.2.7}$$

where b is the width of the channel. This result agrees with (2.2.5) with $f(x) = \pi\sqrt{x}$, which differs from the previous case.

Another configuration, also analyzed by Keller [47], is shown in fig. 2.2.5. We have again a periodic array of perfectly conducting cylinders ($\sigma \to \infty$) embedded in a uniform insulating background ($\sigma_0 \ll \sigma$). The cylinders have their axes a distance c apart and their radii are equal to a. When we apply an electric field in the x direction we have current flowing through the gap between the cylinders. When the cylinders touch each other the effective conductivity is infinite so we are interested in narrow gaps. The effective resistance of this composite is practically equal to the resistance of the gap $R = 1/(C\sigma_0)$, where C is the capacity per unit length of the parallel cylinders in vacuum. To compute C we note that it is equal to half the capacity of one cylinder and the plane midway between the cylinders (see fig. 2.2.6). To find C we must first find the harmonic function ϕ which satisfies $\phi = 0$ on the plane, $\phi = 1$ on the cylinder and $\phi = 0$ at infinity. The capacity is just the charge on the plane or the surface integral of the normal derivative of ϕ on the plane. Since we assume a narrow gap, $\nabla\phi$ is like the electric field between two plates of nonuniform separation. Thus,

$$\phi \sim \frac{x}{\frac{c}{2} - a + \frac{y^2}{2a}}$$

and

$$C \approx \frac{1}{2}\int_{-a}^{a} \nabla\phi \cdot \mathbf{e}_1 dy \approx \frac{1}{2}\int_{-a}^{a} \frac{dy}{\frac{c}{2} - a + \frac{y^2}{2a}} \approx \pi\sqrt{\frac{a}{c-2a}}.$$

The effective resistance is then

$$\overline{R} \approx \sigma_0^{-1}\pi^{-1}\sqrt{\frac{c-2a}{a}} = \sigma_0^{-1}\pi^{-1}\sqrt{\frac{b}{a}}, \tag{2.2.8}$$

which is the reciprocal of (2.2.7).

All the cases considered so far confirm the result (2.2.5), with different forms for the function $f(\cdot)$, the common feature being current channeling in regions of high contrast. If the conducting cylinders in figure 2.2.5 have radii a_1 and a_2, with c the intercenter distance and $b = c - (a_1 + a_2)$ the gap, then the effective resistance is given by

$$\overline{R} \approx \sigma_0^{-1}\pi^{-1}\sqrt{\frac{(a_1 + a_2)b}{2a_1 a_2}}, \tag{2.2.9}$$

which reduces to (2.2.8) when the radii are equal $a_1 = a_2 = a$.

If there are several conducting cylinders in the region (fig. 2.2.7) then the overall conductivity can be calculated by solving the resistor network, shown in fig. 2.2.7, in which each resistance is given by a formula like (2.2.9).

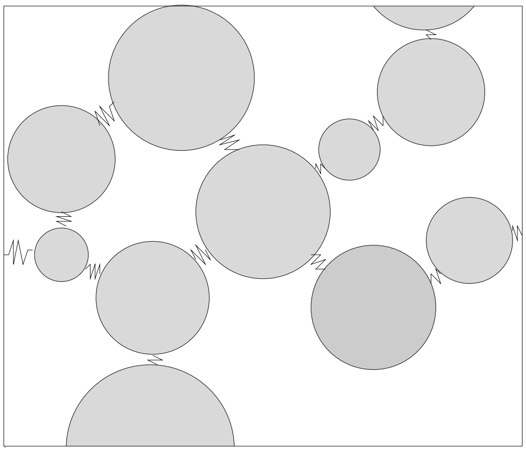

Figure 2.2.7: The effective resistor network for high-conductivity cylindrical inclusions.

We consider now another two component configuration that is different from the previous ones because there are no channels. It is the checkerboard geometry shown in fig. 2.2.8 and analyzed by Keller in [48]. The rectangles have conductivities σ_1 and σ_2 with $\sigma_2 \gg \sigma_1$. The effective conductivity tensor $\overline{\sigma}$ has its principal axes in the x and y directions and is diagonal. For a unit applied electric field in the x direction, the potential difference between the planes $x = \pm h_1/2$ is $\Delta\phi = h_1$. Because $\sigma_2 \gg \sigma_1$, the current flows from one conducting region to another across the corner and it has the magnitude $I = \sigma_c h_1$, where σ_c is the conductivity of the corner. The current density is obtained by normalizing I so that $j = \sigma_c h_1/h_2$ and the effective conductivity of the composite is $\overline{\sigma} \approx \sigma_c h_1/h_2$. It is easy to see that the conductivity of the corner is equal to the effective conductivity of a composite with the same component conductivities but with a square checkerboard geometry (i.e. $h_1 = h_2$). In two dimensions we have the Keller-Dykhne reciprocity relation (see [49, 28, 51])

$$\sigma_x(\sigma_1, \sigma_2) = \frac{1}{\sigma_y(\sigma_1^{-1}, \sigma_2^{-1})}, \tag{2.2.10}$$

where $\sigma_x(\sigma_1, \sigma_2)$ is the effective conductivity of the composite in the x direction, with component conductivities σ_1 and σ_2. Similarly, $\sigma_y(\sigma_1^{-1}, \sigma_2^{-1})$ is the effective conductivity in the y direction with component conductivities σ_1^{-1} and σ_2^{-1}. The

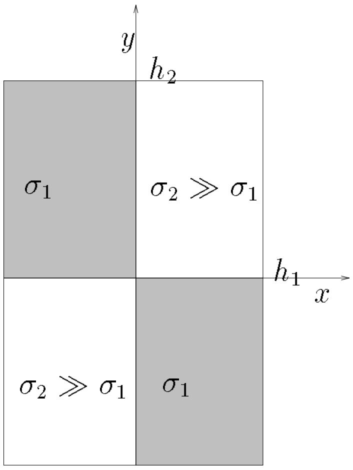

Figure 2.2.8: Rectangular checkerboard

effective conductivity is a linear function in its arguments so

$$\sigma_1\sigma_2 \cdot \sigma_y(\sigma_1^{-1}, \sigma_2^{-1}) = \sigma_y(\sigma_2, \sigma_1) \tag{2.2.11}$$

and

$$\sigma_x(\sigma_1, \sigma_2) = \frac{\sigma_1\sigma_2}{\sigma_y(\sigma_2, \sigma_1)}. \tag{2.2.12}$$

Because the material is isotropic we have

$$\sigma_x(\sigma_1, \sigma_2) = \sigma_y(\sigma_2, \sigma_2) = \sigma_c \tag{2.2.13}$$

which leads to

$$\sigma_c = \sqrt{\sigma_1\sigma_2}. \tag{2.2.14}$$

From (2.2.14) it follows that the effective resistance of the composite with rectangular checkerboard geometry is

$$\overline{R} \approx \frac{1}{\sqrt{\sigma_1\sigma_2}}\frac{h_2}{h_1}. \tag{2.2.15}$$

This result is different from (2.2.5). While the factor h_2/h_1 suggests a geometry dependent function $f(x) = x$, the absence of a channel leads to an effective resistance depending on the geometric average of the component resistances rather than on the resistance of only one component.

Similar asymptotic techniques can be used in the computation of effective conductivity of high contrast discontinuous materials in three dimensions. Keller [47] studied such a problem for a dense cubic periodic array of perfectly conducting identical spheres immersed in a material of small uniform conductivity σ_0. For a dense packing, Keller shows that most of the current flows across narrow gaps separating adjacent spheres. The local analysis of the flow problem in the gaps is similar to the examples presented in this section and the leading term in the asymptotic approximation of the effective conductivity is

$$\overline{\sigma} \approx \frac{\sigma_0 \pi}{2} \log(\frac{a}{h}), \tag{2.2.16}$$

where a is the radius of the spheres and h is the width of the gap. The asymptotic approximation (2.2.16) agrees with the heuristic result (2.2.5) stated in the two-dimensional case and shows that when the spheres touch each other the effective conductivity has a logarithmic singularity.

Batchelor and O'Brien [10] extended Keller's results to the case of a random arrangement of highly conducting particles immersed in a matrix of uniform conductivity σ_0. When the contrast becomes infinite and the volume fraction of the particles is large, they show that if the surface of the inclusions is approximately spherical, the effective conductivity is given by

$$\overline{\sigma} \approx \frac{\sigma_0 \pi}{2} [\log(\frac{a}{h}) + \log(\frac{R^2}{a^2})]. \tag{2.2.17}$$

In formula (2.2.17) h represents the width of the gap, $a = 2R_0R_1/(R_0 + R_1)$ where R_0 and R_1 are the radii of locally spherical surfaces of two adjacent particles and R is chosen such that $R^2 \gg ha$. The first term in (2.2.17) is identical to the one obtained by Keller and the second term is independent of the width of the gap and is of order one.

Batchelor and O'Brien [10] also studied the case of a very high but finite contrast (σ/σ_0). If the width of the gap h is such that $\lambda = (\frac{\sigma}{\sigma_0})^2 \frac{h}{a} \gg 1$, they show that the result (2.2.17) is still valid. However, when h is so small that $\lambda \ll 1$ the effective

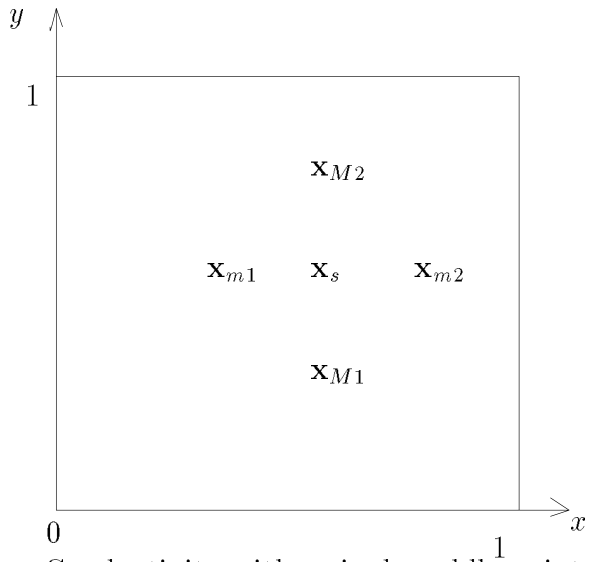

Figure 2.2.9: Conductivity with a single saddle point in the domain

conductivity has the expression

$$\overline{\sigma} \approx 2\pi\sigma_0 \log(\frac{\sigma}{\sigma_0}) + K, \tag{2.2.18}$$

where K is of order one and is independent on the contrast and width of the gap. From (2.2.18) one can draw the interesting conclusion that when the immersed particles have very high but finite conductivity and are separated by small gaps, the effective conductivity is mainly influenced by the conductivity of the matrix (σ_0) and not the contrast (σ/σ_0).

We consider next continuous media with logarithmic high contrast properties.

2.2 The effective conductivity of a composite with high contrast coefficients.

We restrict attention first to a purely resistive problem (equations (2.2.1), (2.2.2)) for a continuous medium with the microscopic resistance $\rho(\mathbf{x}) = \rho_0 e^{-\frac{S(\mathbf{x})}{\epsilon^2}}$. The geometry of the composite is sketched in figure 2.2.9. The microscopic resistance $\rho(\mathbf{x})$ has two minima at $\mathbf{x}_{m1}$ and $\mathbf{x}_{m2}$, two maxima at $\mathbf{x}_{M1}$ and $\mathbf{x}_{M2}$, and a saddle point

$\mathbf{x}_s$. At this point the function $\rho(\mathbf{x})$ is maximum in the x direction and minimum in the y direction. In a small neighborhood of $\mathbf{x}_s$, the function S has the approximate expression

$$S(\mathbf{x}) \approx S(\mathbf{x}_s) + \frac{k^-(x-x_s)^2}{2} - \frac{k^+(y-y_s)^2}{2}. \tag{2.2.19}$$

The geometry we consider here is the continuous equivalent of the discrete case we presented before and, therefore, we expect the following flow behavior.

The effective resistance is given by $\overline{R} \approx \rho(\mathbf{x}_s)\sqrt{\frac{k^+}{k^-}}$ *with the flow concentrated in the driving direction around the saddle point* $\mathbf{x}_s$ *.*

We give a heuristic derivation of this result motivated by the previous examples and return in section 2.4 to give a proof based on variational principles. Just like in the previous cases the current will be small in regions with high resistance and in particular in the vicinity of the maxima $\mathbf{x}_{M1}$ and $\mathbf{x}_{M2}$. Around the minima $\mathbf{x}_{m1}$ and $\mathbf{x}_{m2}$, the bowl shaped resistance function $\rho(\mathbf{x})$ will cause the flow to stall. The only way for the current to pass through the highly resistive region created by the two maxima of $\rho(\mathbf{x})$ is by concentrating itself in a small neighborhood of the saddle point $\mathbf{x}_s$. The small neighborhood of the saddle-point acts like a bottleneck for the current flow, so it is sufficient to solve the cell problem (2.2.1) in the vicinity of $\mathbf{x}_s$ and to look for a current in the x direction. The current is given by $\mathbf{j} = \nabla^\perp u$, where u can be viewed as the magnetic field in the direction perpendicular to Ω. In order for the current to be in the x direction, u must be a function of y only. In a small neighborhood of $\mathbf{x}_s$, where $S(\mathbf{x})$ has the expression (2.2.19), the direct cell problem (2.2.1) simplifies to

$$\frac{d}{dy}[\exp(\frac{k^+(y-y_s)^2}{2\epsilon^2})\frac{du}{dy}] = 0, \tag{2.2.20}$$

with the normalization condition

$$\int_{|y-y_s|\le\delta}(-\frac{du}{dy})dy = 1. \tag{2.2.21}$$

Equation (2.2.20) gives $u'(y) = -D\cdot\exp(-\frac{k^+(y-y_s)^2}{2\epsilon^2})$, where D is a constant obtained from (2.2.21): $D\sqrt{\frac{2\pi\epsilon^2}{k^+}} = 1$. The solution of the direct problem (2.2.1) is

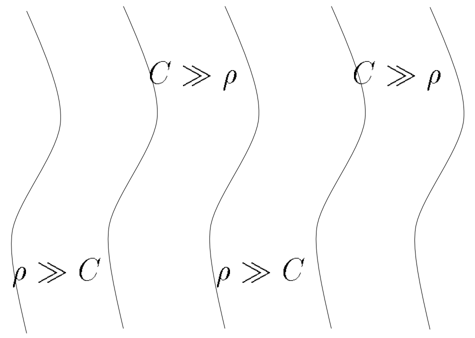

Figure 2.2.10: Medium layered across the driving direction

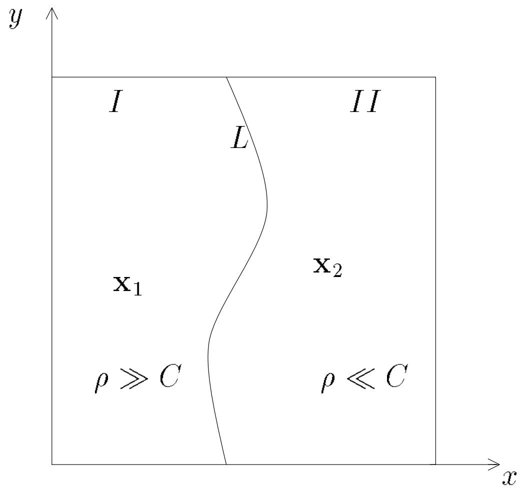

Figure 2.2.11: Enlarged view of the interface between two layers

then

$$\mathbf{j} \approx \frac{1}{\sqrt{\frac{2\pi}{k^+}}\epsilon} \exp(-\frac{k^+(y-y_s)^2}{2\epsilon^2})\mathbf{e}_1, \tag{2.2.22}$$

and by substituting it in (2.2.2) we obtain the effective resistance

$$\overline{R} \approx \rho(\mathbf{x}_s)\sqrt{\frac{2\pi}{k^-}}\epsilon\frac{1}{2\pi\epsilon^2}k^+ \int_{y_s-\delta}^{y_s+\delta} \exp(\frac{k^+(y-y_s)^2}{2\epsilon^2} - \frac{k^+(y-y_s)^2}{\epsilon^2})dy \approx$$
$$\rho(\mathbf{x}_s)\sqrt{\frac{2\pi}{k^-}}\epsilon\frac{1}{2\pi\epsilon^2}k^+\sqrt{\frac{2\pi}{k^+}}\epsilon = \rho(\mathbf{x}_s)\sqrt{\frac{k^+}{k^-}}. \tag{2.2.23}$$

Since the curvatures k^+, k^- have dimensions of $1/L^2$, this result for the effective resistance of the composite agrees with (2.2.5) with $f(x) = x$. In fact the result obtained here is more typical because the saddle points are just continuous versions of the channels, gaps or corners occurring in the discontinuous problems.

2.3 The effective impedance of a composite with high contrast coefficients

Case A: Series connection

We consider the direct problem (2.1.17) with the coefficients ρ and C given by (2.1.26), defined in a medium with the geometry shown in fig. 2.2.10. The medium consists of alternate layers of dominant resistance and capacitance which repeat periodically in the x direction. The functions $\rho(\mathbf{x})$ and $C(\mathbf{x})$ given by (2.1.26) are smooth and periodic and they equal each other along the curves separating the layers. In each layer there is a single saddle point of the dominant resistance or capacitance. For simplicity, we assume that the saddles are oriented along the x direction but the results derived in this section apply to more general orientations, as well. We apply a driving potential difference in the x direction and study the flow through the layered medium. From (2.1.17) we obtain that, in each one of the regions of dominant capacitance or resistance, the problem reduces to the one studied in section 2.2.2. Thus, the current flow is concentrated at the saddle points of ρ and C and oriented in the driving direction x. The question that remains is how the layered regions connect with each other. From fig. 2.2.10 we see that it is sufficient to study the connection between two adjacent layers; the connection between the remaining resistive and capacitive regions is similar. Thus, we concentrate attention on the local problem illustrated in fig. 2.2.11. The functions $\rho(\mathbf{x})$ and $C(\mathbf{x})$ given by (2.1.26) are periodic in the y direction and they equal each other along the dividing curve L. In region I the resistance dominates and has a saddle point $\mathbf{x}_1$ oriented in the driving direction $\mathbf{e}_1$. In region II the capacitance is dominant and has a saddle point $\mathbf{x}_2$ oriented along direction $\mathbf{e}_1$, as well.

From the periodicity in y of the current and the lack of concentration of the vertical flow in both regions I and II, we have

$$< \mathbf{j} >_I = < \mathbf{j} >_{II} = \mathbf{e}_1. \tag{2.2.24}$$

Thus, in region I, where the resistance is dominant, the problem reduces to

$$\begin{aligned} \nabla^\perp[\rho(\mathbf{j}_R + i\mathbf{j}_I)] &= 0 \\ \nabla \cdot \mathbf{j}_R &= \nabla \cdot \mathbf{j}_I = 0 \\ < \mathbf{j}_R > &= \mathbf{e}_1, \quad < \mathbf{j}_I > = \mathbf{0}, \end{aligned} \tag{2.2.25}$$

where $\mathbf{j}_R$, $\mathbf{j}_I$ are the real and imaginary current densities. It is easy to see that the imaginary current is zero, and that the problem reduces to the one studied in section

2.2.2. A similar conclusion applies to region II where the capacitive reactance is dominant. Consequently, the flow behavior in regions I and II is exactly the one studied in section section 2.2.2.

In the vicinity of the curve L, the function $\rho(\mathbf{x})$ ($C(\mathbf{x})$) is continuously decreasing (increasing) with x. Because the flow is driven in the x direction, it must cross the curve L. The current will be diffuse in regions of this neighborhood where ρ and C are fairly flat, and it will concentrate close to the possible common minima of ρ and C along L. This current concentration is weaker than the one at saddle points because it occurs only along one direction (i.e. along L). There is no concentration in the direction perpendicular to the boundary interface and this leads to a lower order term in the effective impedance. In the asymptotic limit of infinitely high contrast, the saddle points of ρ and C will dominate and the contribution of other features like the minima along L are negligible. This conclusion is supported by numerical experiments (see section 2.3.2) and it is proved in section 2.4 using variational principles. We should point out that the same kind of features can occur in the purely resistive problem and exactly as we concluded above they are negligible in the computation of the effective resistance for very high contrast. The validity of this is again demonstrated by variational principles (see section 2.4.1). When the contrast is not very high, features other than the saddle points become important in the computation of $\overline{Z}$ as is seen in chapter 4.

Thus, for computing the effective impedance we need only consider small neighborhoods of the saddle points of $\rho(\mathbf{x})$ and $C(\mathbf{x})$ in regions I, and II. Near these points we have

$$\rho(\mathbf{x}) \approx \rho(\mathbf{x}_1)\exp(\frac{k_1^+(y-y_1)^2}{2\epsilon^2} - \frac{k_1^-(x-x_1)^2}{2\epsilon^2}), \quad \mid \mathbf{x}-\mathbf{x}_1 \mid < \delta \tag{2.2.26}$$

$$C(\mathbf{x}) \approx C(\mathbf{x}_2)\exp(\frac{k_2^+(y-y_2)^2}{2\epsilon^2} - \frac{k_2^-(x-x_2)^2}{2\epsilon^2}), \quad \mid \mathbf{x}-\mathbf{x}_2 \mid < \delta. \tag{2.2.27}$$

In these small regions we can solve our cell problem by separation of variables,

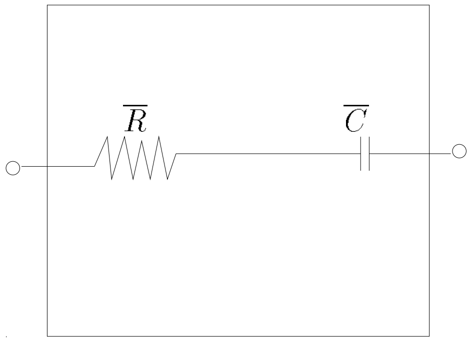

Figure 2.2.12: Equivalent series network

exactly as in section 2.2.2:

$$\begin{aligned}
\mathbf{j}_R &\approx \frac{1}{\sqrt{\frac{2\pi}{k_1^+}}\epsilon}\exp(-\frac{k_1^+(y-y_1)^2}{2\epsilon^2})\mathbf{e}_1, \quad |\mathbf{x}-\mathbf{x}_1| < \delta \\
\mathbf{j}_R &\approx \frac{1}{\sqrt{\frac{2\pi}{k_2^+}}\epsilon}\exp(-\frac{k_2^+(y-y_2)^2}{2\epsilon^2})\mathbf{e}_1, \quad |\mathbf{x}-\mathbf{x}_2| < \delta \qquad (2.2.28) \\
\mathbf{j}_I &\approx 0.
\end{aligned}$$

We use the expression (2.1.21) for the effective impedance and obtain

$$\begin{aligned}
\overline{Z} &\approx \rho(\mathbf{x}_1)\int_{y_1-\delta}^{y_1+\delta}\int_{x_1-\delta}^{x_1+\delta}\frac{1}{\frac{2\pi\epsilon^2}{k_1^+}}\exp(-\frac{k_1^+(y-y_1)^2}{2\epsilon^2}-\frac{k_1^-(x-x_1)^2}{2\epsilon^2})dxdy + \\
&\quad iC(\mathbf{x}_2)\int_{y_2-\delta}^{y_2+\delta}\int_{x_2-\delta}^{x_2+\delta}\frac{1}{\frac{2\pi\epsilon^2}{k_2^+}}\exp(-\frac{k_2^+(y-y_2)^2}{2\epsilon^2}-\frac{k_2^-(x-x_2)^2}{2\epsilon^2})dxdy \qquad (2.2.29) \\
&\approx \rho(\mathbf{x}_1)\sqrt{\frac{k_1^+}{k_1^-}} + iC(\mathbf{x}_2)\sqrt{\frac{k_2^+}{k_2^-}}.
\end{aligned}$$

This result, together with the observation that the current has the same normalized average over regions I or II as over the entire cell, tells us that our problem is asymptotically equivalent to the discrete series circuit shown in fig. 2.2.12. We have only two network elements: one resistor $\overline{R} = \rho(\mathbf{x}_1)\sqrt{\frac{k_1^+}{k_1^-}}$ placed at $\mathbf{x}_1$, and a capacitor $\overline{C} = C(\mathbf{x}_2)\sqrt{\frac{k_2^+}{k_2^-}}$ placed at $\mathbf{x}_2$. The current passing through $\overline{R}$ is $< \mathbf{j}_R + i\mathbf{j}_I >_I = \mathbf{e}_1$, and the current passing through $\overline{C}$ is $< \mathbf{j}_R + i\mathbf{j}_I >_{II} = \mathbf{e}_1$.

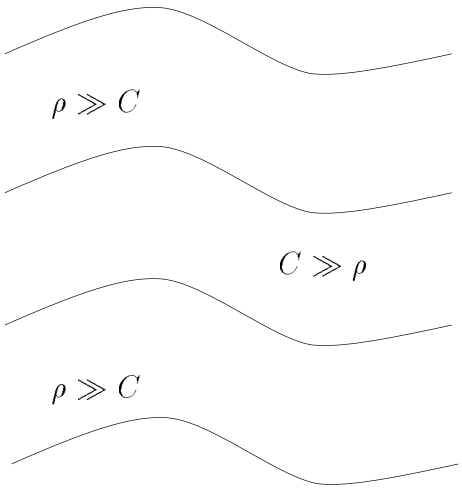

Figure 2.2.13: Medium layered along the driving direction

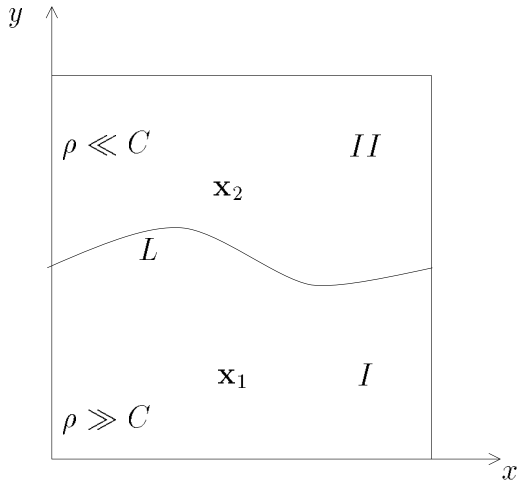

Figure 2.2.14: Enlarged view of the interface between two layers

Case B: Parallel connection

We consider the direct problem (2.1.17) with the coefficients ρ and C given by (2.1.26), defined in a medium with the geometry shown in fig. 2.2.13. The medium consists of alternate layers of dominant resistance and capacitance which repeat periodically in the y direction. The functions $\rho(\mathbf{x})$ and $C(\mathbf{x})$ given by (2.1.26) are smooth and periodic and they equal each other along the curves separating the layers. In each layer there is a single saddle point of the dominant resistance or capacitance. For simplicity, we assume that the saddles are oriented along the x direction but the results derived in this section apply to more general orientations, as well.

We apply a driving potential difference in the x direction and study the flow through the layered medium. From (2.1.17) we obtain that

$$\begin{aligned} \nabla^{\perp} \cdot [\rho(\mathbf{j}_R + i\mathbf{j}_I)] &= 0 \text{ for } \mathbf{x} \in \text{region with } \rho \gg C \\ \nabla^{\perp} \cdot [C(\mathbf{j}_R + i\mathbf{j}_I)] &= 0 \text{ for } \mathbf{x} \in \text{region with } C \gg \rho, \end{aligned} \tag{2.2.30}$$

where $\mathbf{j}_R$ and $\mathbf{j}_I$ are the real and imaginary current densities. The flow is driven in the x direction so we have $< \mathbf{j}_R + i\,\mathbf{j}_I >= K\mathbf{e}_1$, where K is a complex constant flux.

We can rewrite the current densities as

$$\mathbf{j}_R = \mathrm{real}(K)\mathbf{e}_1 + \nabla^\perp u, \; \mathbf{j}_I = \mathrm{imag}(K)\mathbf{e}_1 + \nabla^\perp v,$$

where u and v can be viewed as the real and imaginary parts of the magnetic field. The functions $u(\mathbf{x})$ and $v(\mathbf{x})$ are periodic in the domain and satisfy the conditions

$$< \nabla^\perp u >=< \nabla^\perp v >= \mathbf{0}.$$

From the periodicity in x of both u and v, it follows that in each region there is no net flux in the y direction. For the flow in the x direction we have

$$\begin{aligned} \int_i \mathbf{j}_R \cdot \mathbf{e}_1 d\mathbf{x} &= \alpha_i \mathbf{e}_1, \; i \text{ denotes any layer} \\ \int_i \mathbf{j}_I \cdot \mathbf{e}_1 d\mathbf{x} &= \beta_i \mathbf{e}_1 \\ \sum_i \alpha_i &= \mathrm{real}(K), \\ \sum_i \beta_i &= \mathrm{imag}(K). \end{aligned} \tag{2.2.31}$$

Equations (2.2.30) with the driving conditions (2.2.31) are very similar to the problem studied in section 2.2.2 and show that the flow in each region of the domain is concentrated at the saddle points of ρ and C, respectively. The remaining question is how the regions connect with each other. From fig. 2.2.13 we see that it is sufficient to study the connection between two adjacent layers; the other layers connect in a similar way. Thus, we concentrate attention on the local problem shown in fig. 2.2.14. In the resistive region I, ρ has a saddle point $\mathbf{x}_1$ oriented in the x direction and in the capacitive region II, C has a saddle point $\mathbf{x}_2$ oriented in the x direction, as well. The functions $\rho(\mathbf{x})$ and $C(\mathbf{x})$ given by (2.1.26) are periodic in x and they equal each other along the curve L. For simplicity we assume that the average flow over regions I and II is

$$\int_I \mathbf{j} d\mathbf{x} + \int_{II} \mathbf{j} d\mathbf{x} = \mathbf{e}_1.$$

A different driving condition with both real and imaginary net fluxes does not affect the expression of the effective impedance, it just modifies the fluxes of current in the channels (saddles). Consequently, we have

$$\begin{aligned} \nabla^{\perp} \cdot [\rho(\mathbf{j}_R + i\mathbf{j}_I)] &= 0 \\ < \mathbf{j}_R > &= \alpha_1 \mathbf{e}_1 \\ < \mathbf{j}_I > &= \beta_1 \mathbf{e}_1 \\ \nabla \cdot \mathbf{j}_R &= \nabla \cdot \mathbf{j}_I = 0 \\ \mathbf{x} &\in \text{region } I, \end{aligned} \tag{2.2.32}$$

$$\begin{aligned} \nabla^{\perp} \cdot [iC(\mathbf{j}_R + i\mathbf{j}_I)] &= 0 \\ < \mathbf{j}_R > &= \alpha_2 \mathbf{e}_1 \\ < \mathbf{j}_I > &= \beta_2 \mathbf{e}_1 \\ \nabla \cdot \mathbf{j}_R &= \nabla \cdot \mathbf{j}_I = 0 \\ \mathbf{x} &\in \text{region } II. \end{aligned} \tag{2.2.33}$$

In the vicinity of the curve L the function $\rho(\mathbf{x})$ ($C(\mathbf{x})$) is continuously decreasing (increasing) with y. In this region the current is diffuse and small where ρ and C are fairly flat. If for example ρ and C have two maxima along L and a minimum in between, because we have no driving force in the y direction the current avoids the two maxima and is relatively small at the minimum as well. Consequently, the behavior of the flow for this problem is dictated by what happens in regions I, and II, for which we already know the result. This case is a little more complicated than case A because the current is divided between the two regions of our domain. Since the average current over the domain shown in fig. 2.2.14 is $\mathbf{e}_1$, we must have

$$\begin{aligned} \alpha_1 + \alpha_2 &= 1 \\ \beta_1 + \beta_2 &= 0. \end{aligned} \tag{2.2.34}$$

We already know that, in order to obtain the effective impedance of the regions I and II, it is sufficient to look only in small neighborhoods of saddle points of ρ and C. In the vicinity of these points we have

$$\rho(\mathbf{x}) \approx \rho(\mathbf{x}_1) \exp(\frac{k_1^+(y-y_1)^2}{2\epsilon^2} - \frac{k_1^-(x-x_1)^2}{2\epsilon^2}), \quad | \mathbf{x} - \mathbf{x}_1 | < \delta, \tag{2.2.35}$$

$$C(\mathbf{x}) \approx C(\mathbf{x}_2)\exp(\frac{k_2^+(y-y_2)^2}{2\epsilon^2} - \frac{k_2^-(x-x_2)^2}{2\epsilon^2}), \quad |\mathbf{x}-\mathbf{x}_2| < \delta \tag{2.2.36}$$

and by using separation of variables in (2.2.32) and (2.2.33) we obtain

$$\mathbf{j}_R + i\mathbf{j}_I \approx \frac{\alpha_1}{\sqrt{\frac{2\pi}{k_1^+}}\epsilon}\exp(-\frac{k_1^+(y-y_1)^2}{2\epsilon^2}) + i\frac{\beta_1}{\sqrt{\frac{2\pi}{k_1^+}}\epsilon}\exp(-\frac{k_1^+(y-y_1)^2}{2\epsilon^2}), \quad |\mathbf{x}-\mathbf{x}_1| < \delta$$

$$(2.2.37)$$

$$\mathbf{j}_R + i\mathbf{j}_I \approx \frac{\alpha_2}{\sqrt{\frac{2\pi}{k_2^+}}\epsilon}\exp(-\frac{k_2^+(y-y_2)^2}{2\epsilon^2}) + i\frac{\beta_2}{\sqrt{\frac{2\pi}{k_2^+}}\epsilon}\exp(-\frac{k_2^+(y-y_2)^2}{2\epsilon^2}), \quad |\mathbf{x}-\mathbf{x}_2| < \delta.$$

We can use these results in the formula for the effective impedance (2.1.21) and, after performing straightforward computations, we obtain

$$\overline{Z} = [\overline{R}(\alpha_1^2 - \beta_1^2) - 2\overline{C}\alpha_2\beta_2] + i[\overline{C}(\alpha_2^2 - \beta_2^2) + 2\overline{R}\alpha_1\beta_1], \tag{2.2.38}$$

where $\overline{R} \approx \rho(\mathbf{x}_1)\sqrt{\frac{k_1^+}{k_1^-}}$ and $\overline{C} \approx C(\mathbf{x}_2)\sqrt{\frac{k_2^+}{k_2^-}}$. In order to determine the fluxes $\alpha_i, \beta_i, \quad i = 1,2$ we look at the potential gradient $\nabla\Phi(\mathbf{x})$ which is given by

$$\nabla\Phi(\mathbf{x}) = (\rho + iC)(\mathbf{j}_R + i\mathbf{j}_I). \tag{2.2.39}$$

We multiply equation (2.2.39) by $\mathbf{e}_1$ and average over the domain to obtain

$$< \nabla\Phi \cdot \mathbf{e}_1 >= \Delta U =< (\rho + iC)(\mathbf{j}_R + i\mathbf{j}_I)\cdot \mathbf{e}_1 >= \overline{Z}. \tag{2.2.40}$$

We can do the same thing for regions I and II. Because $\nabla\Phi$ is periodic over the cell and regions I and II have the same boundaries as the cell in the x direction, the average potential difference for the entire cell equals the average potential difference over regions I and II. Consequently we have

$$\Delta U = \overline{Z} = \overline{R}(\alpha_1 + i\beta_1) = i\overline{C}(\alpha_2 + i\beta_2). \tag{2.2.41}$$

Relations (2.2.41) and (2.2.34) form a linear system of four equations and four unknowns with solution

$$\alpha_1 = \frac{\overline{C}^2}{\overline{R}^2 + \overline{C}^2},$$

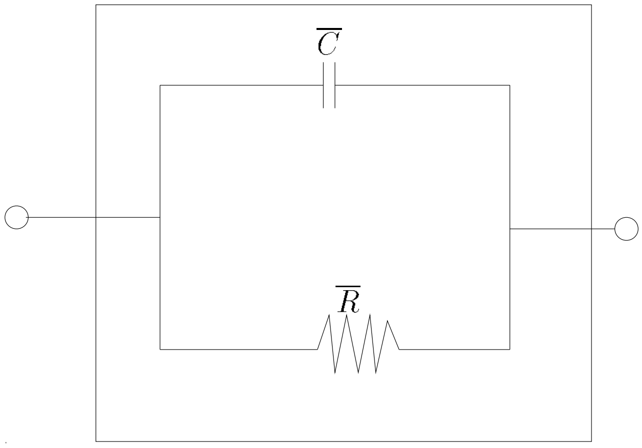

Figure 2.2.15: Equivalent parallel network

$$\begin{aligned} \beta_1 &= \frac{\overline{RC}}{\overline{R}^2 + \overline{C}^2}, \\ \beta_2 &= -\frac{\overline{RC}}{\overline{R}^2 + \overline{C}^2}, \\ \alpha_2 &= \frac{\overline{R}^2}{\overline{R}^2 + \overline{C}^2}. \end{aligned} \tag{2.2.42}$$

Using (2.2.42) in (2.2.38) we obtain the following expression for the effective impedance

$$\overline{Z} = \frac{\overline{RC}^2}{\overline{R}^2 + \overline{C}^2} + i\frac{\overline{R}^2\overline{C}}{\overline{R}^2 + \overline{C}^2} = \left(\frac{1}{\overline{R}} + \frac{1}{i\overline{C}}\right)^{-1}. \tag{2.2.43}$$

This result suggests that the continuous problem is asymptotically equivalent to the discrete network shown in fig. 2.2.15, where a resistor $\overline{R}$ placed at $\mathbf{x}_1$ is connected in parallel with a capacitor $\overline{C}$ placed at $\mathbf{x}_2$. The current passing through $\overline{R}$ is $< \mathbf{j}_R + i\mathbf{j}_I >_I = \alpha_1\mathbf{e}_1 + i\beta_1\mathbf{e}_1$, and the current passing through $\overline{C}$ is $< \mathbf{j}_R + i\mathbf{j}_I >_{II} = \alpha_2\mathbf{e}_1 + i\beta_2\mathbf{e}_1$.

3 Numerical computations

We will now present the results of numerical experiments which illustrate the analytical results in section 2.2. We compute the effective impedance associated with the direct problem by solving (2.1.15) with a spectral method, as explained in appendix B. In all computations we used a resolution of 64×64 grid points and the size of the periodic cell was $2\pi \times 2\pi$.

3.1 Static fields - resistive circuit

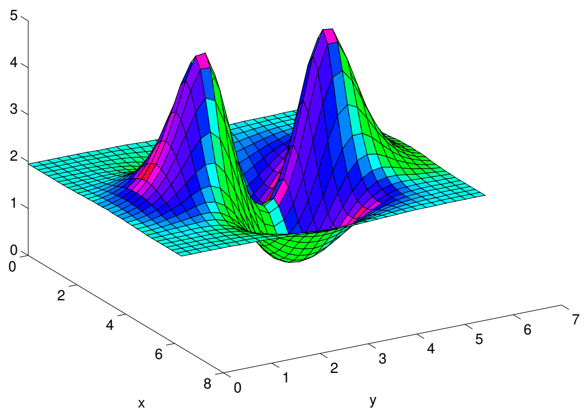

Figure 2.3.16: Microscopic resistance $\rho(\mathbf{x})$

The first set of numerical experiments we present is for static fields which are purely resistive. We consider the simple geometry presented in section 2.2.2. The microscopic resistance $\rho(\mathbf{x})$ has a saddle point at $\mathbf{x}_s = (\pi, \pi)$, two minima at $\mathbf{x}_{m1} = (2.432, \pi)$ and $\mathbf{x}_{m2} = (4.054, \pi)$ and two maxima at $\mathbf{x}_{M1} = (\pi, 2.432)$ and $\mathbf{x}_{M2} = (\pi, 4.054)$ as shown in fig. 2.3.16. Around the saddle point $\mathbf{x}_s$, the microscopic resistance can be approximated by

$$\rho(\mathbf{x}) \approx \rho(\mathbf{x}_s) \exp(-\frac{k^-(x-x_s)^2}{2\epsilon^2} + \frac{k^+(y-y_s)^2}{2\epsilon^2}), \tag{2.3.1}$$

where ϵ, $\rho(\mathbf{x}_s)$, k^- and k^+ will be specified for each experiment. The contrast in ρ (i.e., $\max(\rho)/\min(\rho)$) can be controlled by changing the curvatures k^+, k^- and the parameter ϵ. Our analysis tells us that the current is in the driving direction and concentrated in a small neighborhood of the saddle point. The effective resistance is

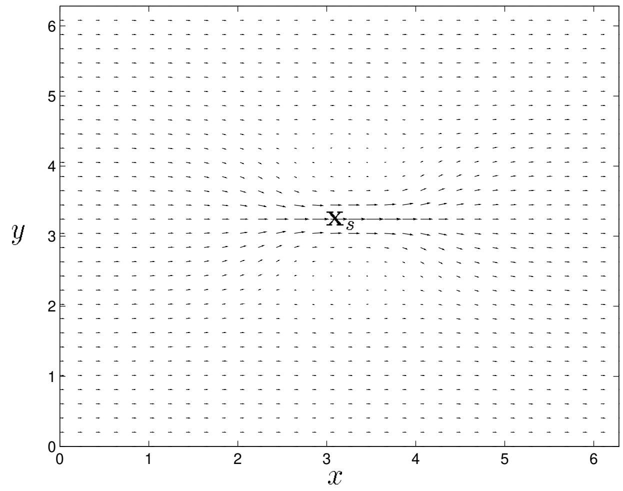

Figure 2.3.17: Real current flow in purely resistive medium

Contrast	$\rho(\mathbf{x}_s)$	k^+	k^-	$\overline{R}$	$\overline{R}_{num}$	Rel. error (%)
70	1.	1.4	1.8	1.1339	1.2011	5.39
83	4.1727	2.6	3.4	3.6489	3.4714	-4.86
97	2.0427	0.8	2.	1.2919	1.3478	4.33
200	4.1727	2.4	1.6	5.1105	5.2114	1.97

Table 2.3.1: Dependence of $\overline{R}$ on the conductivity and curvatures at the saddle point

given by $\overline{R} \approx \rho(\mathbf{x}_s)\sqrt{\frac{k^+}{k^-}}$ and we have a simple discrete network that consists of only one resistor.

In the first experiment we want to test the formula we obtained for $\overline{R}$. We fix $\epsilon^2 = 0.06$ and vary the height of the saddle as well as the curvatures k^- and k^+. We compute numerically the current $\mathbf{j}$ as explained in appendix B. The effective resistance $\overline{R}_{num} = \int_\Omega \rho(\mathbf{x})\mathbf{j}(\mathbf{x}) \cdot \mathbf{j}(\mathbf{x}) d\mathbf{x}$ is obtained by the trapezoidal rule for numerical integration. The parameters used in each numerical test and the results are shown in the table 2.3.1. For the cases presented in this table the contrast increased progressively from 70 to 200. The agreement between the effective resistance obtained numerically

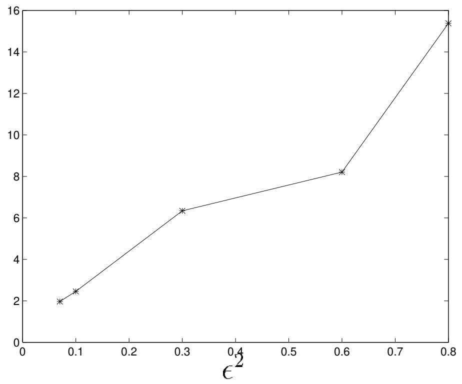

Figure 2.3.18: Relative error in $\overline{R}$ (%)

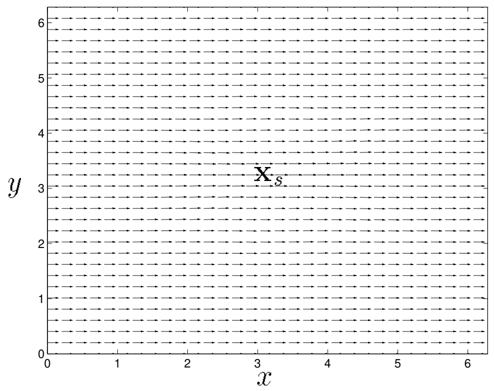

Figure 2.3.19: Real current flow in low contrast resistive medium $\epsilon^2 = 0.8$

and the asymptotic one was very good, with an error $\sim 5\%$ for the lowest contrast and $\sim 1\%$ for the highest contrast. We also performed tests for higher contrasts and observed that for contrasts in the range $10^2 \div 10^4$ the relative error remained in the range 1%. For contrasts higher than 10^4 we obtained numerical instabilities; in order to obtain better results we need a better numerical method (see chapter 4). For all four cases summarized in the table the current flow looked very similar and in fig. 2.3.17 we present one of them. We use arrows with length proportional to the magnitude of the current in order to indicate the direction and strength of the flow. The behavior of the current is as predicted by the theory.

In order to check the behavior of the solution as $\epsilon \to 0$, we consider several numerical experiments in which we fix the constants $k^- = 1.6$ and $k^+ = 2.4$ and vary ϵ. The data and results are presented in the table below. In fig. 2.3.18 we show the dependence of the relative error on ϵ and we see that as $\epsilon \to 0$ we have confirmation of the validity of the asymptotic result. The contrast of the resistance varies between 9.1 for the first experiment and 209.2 for the last experiment. For contrasts of order 10^2 the relative error stays within a few percent but as the contrast decreases the error increases dramatically. While for the last four tests (contrast ~ 50 to 209.2) the error is less than 10%, for the last test (contrast $= 9$) the error jumped to 15%. The real current flow for the last experiment in the table is shown in fig. 2.3.17 and, as predicted, the current is concentrated at the saddle point and is in the

Contrast	$\rho(\mathbf{x}_s)$	ϵ^2	$\overline{R}$	$\overline{R}_{num}$	Rel. error (%)
9.1	1.1331	0.8	1.3878	1.1744	15.38
50	1.1814	0.6	1.4469	1.3281	-8.21
65	1.3956	0.3	1.7093	1.8176	6.34
165	2.7183	0.1	3.3292	3.4212	2.46
209.2	4.1727	0.07	5.1105	5.2114	1.97

Table 2.3.2: Accuracy of the resistor network approximation versus the contrast

driving direction. The effective resistance obtained numerically also agreed with the theoretical one within 1%. For the case with $\epsilon^2 = 0.8$ (i.e., contrast 9.1) we see from fig. 2.3.19 that the current has approximately the same magnitude throughout the domain. The contrast in this case is too low for our analysis to apply and we obtain an effective resistance which is quite different from the one given by the asymptotic formula.

3.2 Quasistatic limit - series connection

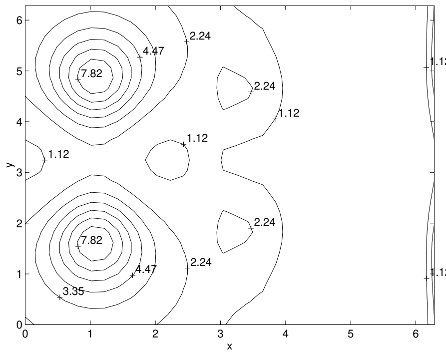

Figure 2.3.20: Microscopic resistance $\rho(\mathbf{x})$

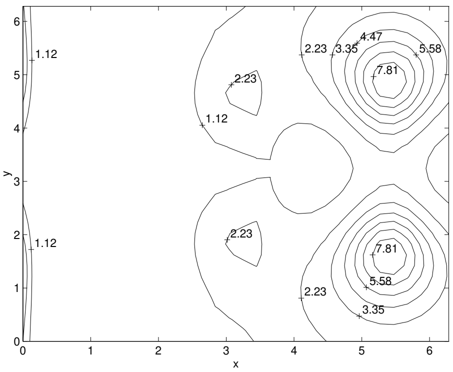

Figure 2.3.21: Microscopic capacitance $C(\mathbf{x})$

In the second set of computations we consider the quasistatic limit of the fields and illustrate the equivalence of continuum high contrast problems with a discrete series network. The geometry we consider is similar to the one in section 2.2.3, Case

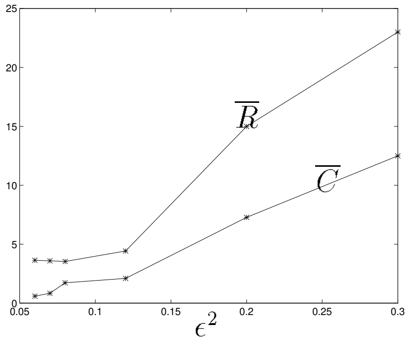

Figure 2.3.22: Relative error in $\overline{R}$ and $\overline{C}$ (%) as $\epsilon \to 0$

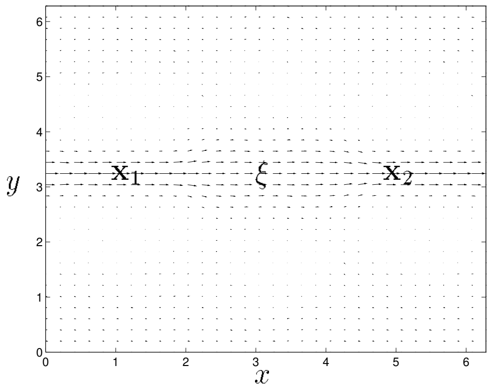

Figure 2.3.23: Real current flow ($\epsilon^2 = 0.06$); series R-C network

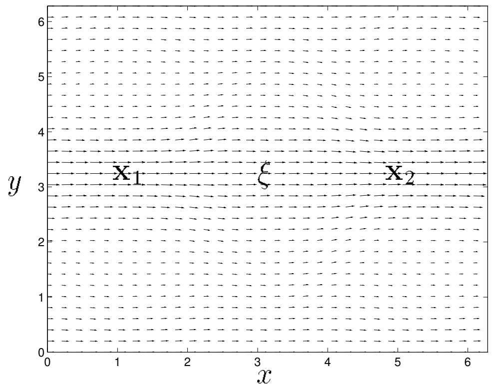

Figure 2.3.24: Real current flow ($\epsilon^2 = 0.3$); series R-C network

A. The microscopic resistance ρ has a saddle point $\mathbf{x}_1$ in region I and is negligible in region II, whereas the capacitive reactance C has a saddle point $\mathbf{x}_2$ in region II and is negligible in region I. The two regions are separated by the line $x = \pi$ along which ρ and C have a common minimum at ξ. In fig. 2.3.20 and 2.3.21 we present contour plots of ρ and C for one of our experiments. These pictures are typical for the whole set of experiments where we change the height of the saddles, the curvatures and the position of the critical points in the domain. Around the saddle points the resistance and capacitance are given by (2.2.26) and (2.2.27). We saw in section 2.2.2 that in Ω we can have regions of flow concentration other than saddle points which are negligible in the computation of the effective impedance in the limit of infinitely high contrast. As an example of such a region we considered the common minimum

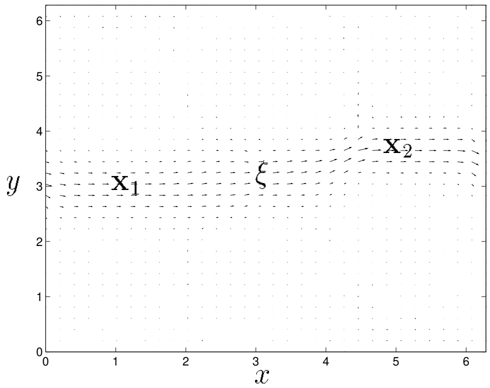

Figure 2.3.25: Real current flow ($\epsilon^2 = 0.06$); series R-C network; saddles distorted

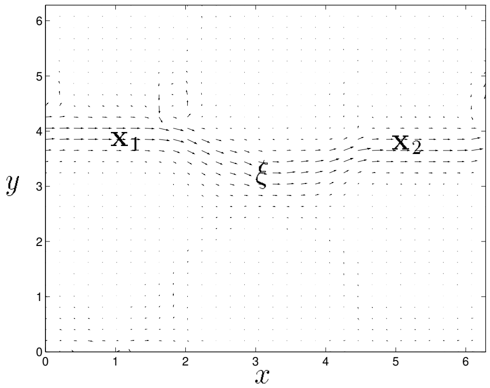

Figure 2.3.26: Real current flow ($\epsilon^2 = 0.06$); series R-C network; saddles distorted

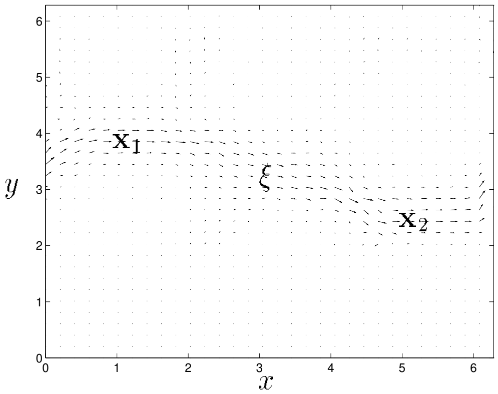

Figure 2.3.27: Real current flow ($\epsilon^2 = 0.06$); series R-C network; saddles distorted

at ξ along the boundary interface where the functions ρ and C are strictly monotonic in the x direction. In the vicinity of ξ we have

$$\begin{aligned} \rho(\mathbf{x}) &\approx \rho(\xi_m)\exp\Big(\frac{k(y-\eta)^2}{2\epsilon^2} - \frac{c(x-\xi)}{\epsilon^2}\Big), \\ C(\mathbf{x}) &\approx \rho(\xi_m)\exp\Big(\frac{k(y-\eta)^2}{2\epsilon^2} + \frac{d(x-\xi)}{\epsilon^2}\Big). \end{aligned} \tag{2.3.2}$$

Our theory predicts that the current is real, in the driving direction and concentrated around the points $\mathbf{x}_1$ and $\mathbf{x}_2$. The effective impedance is obtained from (2.2.29).

In order to test our result for different contrasts we fixed the curvatures and

$\rho(\mathbf{x}_1)$	$C(\mathbf{x}_2)$	$\rho(\xi)$	ϵ^2	$\overline{R}$	$\overline{R}_{num}$	Rel. Error	$\overline{C}$	$\overline{C}_{num}$	Rel. Error
28.0316	28.0316	1	0.06	28.0316	29.0506	3.64 %	22.1609	22.2818	0.6 %
17.4117	17.4117	0.7	0.07	17.4117	18.0364	3.59	13.7652	13.8814	0.84
12.1825	12.1825	0.6	0.08	12.1825	12.6136	3.54	9.631	9.8037	1.73
5.2945	5.2945	0.3	0.12	5.2945	5.0600	-4.43	4.1857	4.0979	-2.10
2.7183	2.7183	0.1	0.2	2.7183	2.3028	-15.	2.1490	1.9925	-7.28
1.9477	1.9477	0.08	0.3	1.9477	1.5001	-23.	1.5398	1.3472	-12.5

Table 2.3.3: Accuracy of the R-C series network approximation versus the contrast

positions of the critical points in the domain to the following values: $k_1^+ = 1., k_1^- = 1., k_2^+ = 1., k_2^- = 1.6, k = 0.8, c = 0.3, d = 0.5, \mathbf{x}_1 = (\frac{\pi}{3}, \pi), \mathbf{x}_2 = (\frac{5\pi}{3}, \pi)$ and $\xi = (\pi, \pi)$. We varied ϵ and hence the height of ρ and C at the three critical points. The table below summarizes the results. The contrast for ρ and C varied from 10^3 to 9.45. The change in the relative error with ϵ is shown in fig. 2.3.22. We see that for the first four computations where the contrast was between 10^2 and 10^3 we have very good agreement with our theoretical result (error is just a few percent). For the last two computations the contrast was about 10 and the error increased dramatically to ten or more percent. In fig. 2.3.23 we show the computed field for the first entry in the table. The current flow is in the driving direction and concentrated around the critical points as predicted. Note that at the saddle points the current concentrates in both directions (i.e. highest magnitude is at $\mathbf{x}_i, \quad i = 1, 2$) but at ξ the magnitude of the current increases only when we approach it along the y direction. At this point there is no current concentration along the x direction as can be seen analytically also. For the last experiment in the table, where we have contrast of 9.45 for ρ and C, the current flow is shown in fig. 2.3.24, and we note only small flow concentration at the critical points in the domain. The lack of current concentration at the saddle points accounts for the poor network approximation and the large errors in $\overline{Z}$. For all the computations summarized in the table the imaginary current was two orders of magnitude smaller than the real one. We note from the table that the error in

$\mathbf{x}_1$	$\mathbf{x}_2$	ξ	$\overline{R}_{num}$	Rel. Error	$\overline{C}_{num}$	Rel. Error
$(\frac{\pi}{3}, 2.9)$	$(\frac{5\pi}{3}, 3.4)$	(π, π)	18.008	3.43 (%)	13.879	0.83 (%)
$(\frac{\pi}{3}, 3.4)$	$(\frac{5\pi}{3}, 3.4)$	(π, π)	18.179	4.41	13.293	-3.43
$(\frac{\pi}{3}, 3.9)$	$(\frac{5\pi}{3}, 2.7)$	(π, π)	18.118	4.05	14.135	1.85

Table 2.3.4: Accuracy of the series network approximation versus the position of the channels in the domain

the resistance is always slightly larger than the one for the capacitive reactance. The explanation for this behavior is the higher curvatures chosen for C. We also performed experiments for contrasts higher than 10^3 and the relative error remained in the range of 1%. For contrasts higher than 10^4 we encountered numerical instabilities, as in the real case. From these computations we can conclude that for contrasts higher than 10^2 the asymptotic analysis gives the effective impedance within $\sim 1\%$. For lower contrasts, the approximation is not so good.

Since we already studied the influence of the curvatures k_i^+ and k_i^- for the purely resistive case, the next series of computations was done for $\epsilon^2 = 0.07$, $\rho(\mathbf{x}_1) = 17.4117 = C(\mathbf{x}_2)$, $\rho(\xi) = 0.7$, $k_1^+ = 1.$, $k_1^- = 1.$, $k_2^+ = 1.$, $k_2^- = 1.6, k = 0.8, c = 0.3$ and $d = 0.5$. However, the position of the critical points was changed. We again have the same series network with $\overline{Z} = 17.4117 + i \cdot 13.7652$, the only difference being the location of the network elements. The results are presented in the table below.

The contrasts for ρ and C were 500 and 700 and they were kept fixed throughout this set of computations. From the table above we see that the error between the impedance computed numerically and the predicted one remained within a few percent of each other. The current flow is shown in fig. 2.3.25, 2.3.26 and 2.3.27 and the concentration around the critical points is clear. The imaginary current was two orders of magnitude smaller than the real one. From this set of computations we may conclude that as long as the geometry of the regions of dominant ρ and C remains as shown in fig. 2.2.11, the series network is a good approximation for different positions of the saddle points.

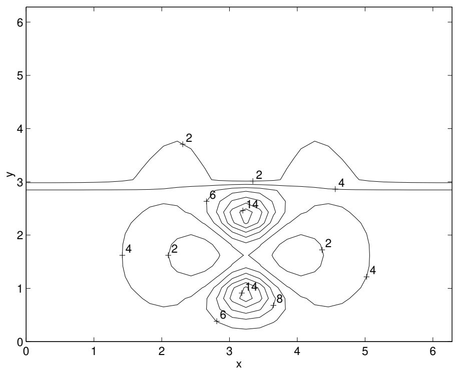

Figure 2.3.28: Microscopic resistance $\rho(\mathbf{x})$

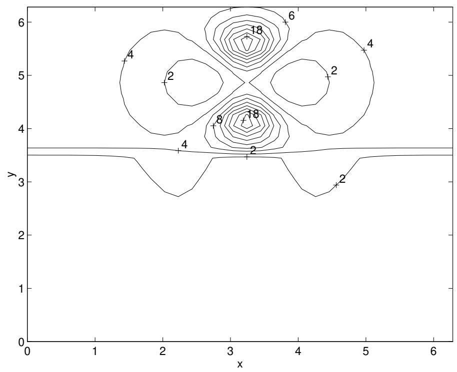

Figure 2.3.29: Microscopic capacitance $C(\mathbf{x})$

3.3 Quasistatic limit - parallel connection

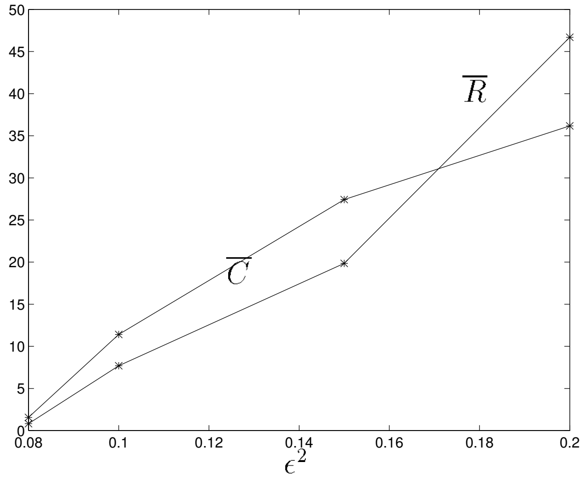

Figure 2.3.30: Relative error in $\overline{R}$ and $\overline{C}$ (%) as $\epsilon \to 0$

In the third set of numerical computations we consider the quasistatic regime and explore the approximation of the continuous problem by a parallel discrete network. The geometry is similar to the one in §2.3 Case B. The resistance ρ has a saddle point $\mathbf{x}_1$ in region I and it is negligible in region II, whereas the capacitance C has a saddle point $\mathbf{x}_2$ in region II and it is negligible in region I. regions I and II are separated by the line $y = \pi$ along which ρ and C have a common minimum at ξ. In fig. 2.3.28 and 2.3.29 we present contour plots of ρ and C for one of our experiments. These pictures

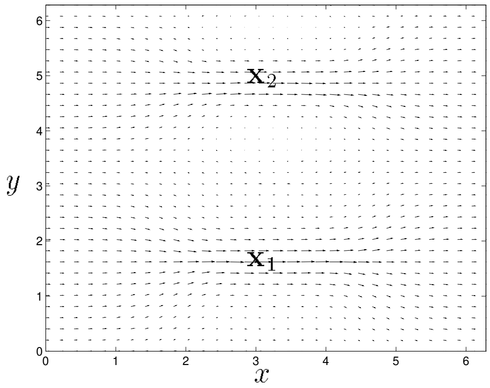

Figure 2.3.31: Real current flow ($\epsilon^2 = 0.08$); parallel R-C network

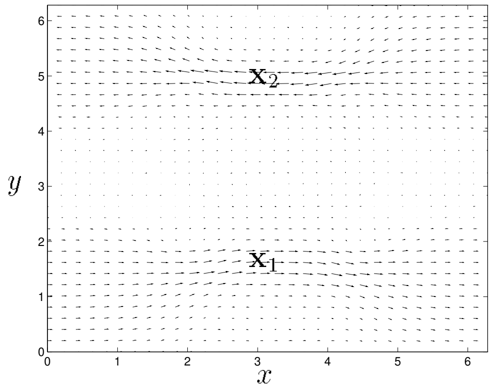

Figure 2.3.32: Imaginary current flow ($\epsilon^2 = 0.08$); parallel R-C network

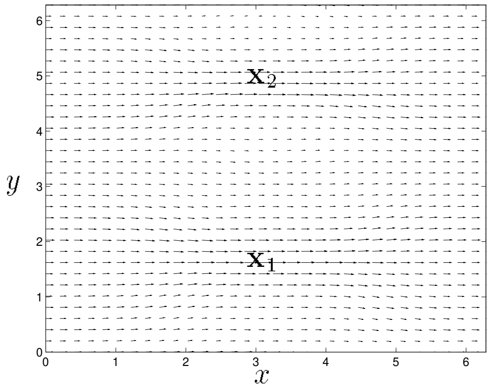

Figure 2.3.33: Real current flow ($\epsilon^2 = 0.2$); parallel R-C network

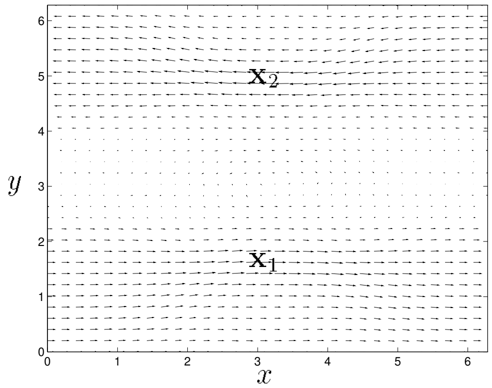

Figure 2.3.34: Imaginary current flow ($\epsilon^2 = 0.2$); parallel R-C network

are typical for all the numerical computations but we change the height of the saddles, the curvatures and the position of the critical points in the domain. Near the saddle points ρ and C are given by (2.2.26) and (2.2.27). The asymptotic theory predicts that the current is in the driving direction and concentrated around the saddle points. The current is divided between the two regions and its average over regions I or II is given by (2.2.42). The effective impedance is given by (2.2.43).

To test the validity of the network approximation for different contrasts, in the first series of computations we fixed the curvatures and positions of the critical points in the domain to the following values: $k_1^+ = 1., k_1^- = 1., k_2^+ = 1.6, k_2^- = 1., \mathbf{x}_1 =$

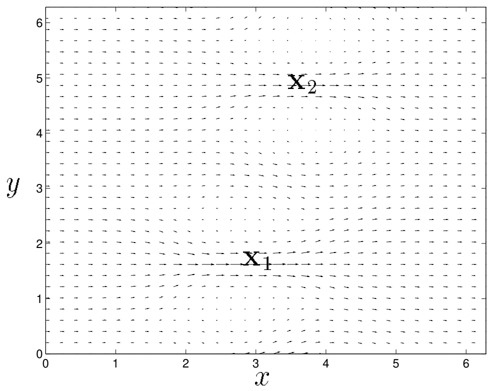

Figure 2.3.35: Real current flow; parallel R-C network; saddles distorted

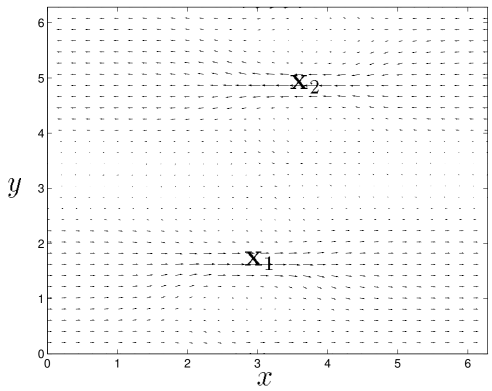

Figure 2.3.36: Imaginary current flow; parallel R-C network; saddles distorted

$\rho(\mathbf{x}_1)$	$C(\mathbf{x}_2)$	ϵ^2	real$(\overline{Z})$	real $(\overline{Z}_{num})$	Rel. Error	imag$(\overline{Z})$	imag $(\overline{Z}_{num})$	Rel. Error
12.1825	12.1825	0.08	7.4961	7.3967	-0.82 %	5.9256	5.8333	-1.56 %
7.3891	7.3891	0.1	4.5471	4.1970	-7.7	3.6955	4.1172	11.41
3.7937	3.7937	0.15	2.3346	1.8712	-19.85	1.8457	1.1394	-27.43
2.7183	2.7183	0.2	1.6728	0.8918	-46.7	1.3225	0.8442	-36.17

Table 2.3.5: Accuracy of the R-C parallel network approximation versus the contrast

$(\pi, \frac{\pi}{3}), \mathbf{x}_2 = (\pi, \frac{5\pi}{3})$ and $\xi = (\pi, \pi)$. We varied ϵ and hence the height of ρ and C at the three critical points. In the table below we show the parameters used, the asymptotic and numerical $\overline{Z}$, the relative error and the asymptotic and numerical current fluxes (i.e., α_i, β_i). The contrast varied between 300 for the first computation and 10 for the last one. The change in the relative error with ϵ is shown in fig. 2.3.30, and we see that for ϵ small enough (i.e., contrast $\geq 10^2$) we have agreement within a few percent with the network approximation (see first two experiments in the table). However, as we saw in the previous sections, for lower contrasts (i.e., larger ϵ) the error is quite large (see last two experiments in the table). The current flow for the first computation in the table is shown in fig. 2.3.31 and 2.3.32 and its behavior is the one predicted by the asymptotic theory. For the last case, where the contrast was

α_1	α_1^{num}	β_1	β_1^{num}	α_2	α_2^{num}	β_2	β_2^{num}
0.6154	0.6120	0.4865	0.4783	0.3846	0.3880	-0.4865	- 0.4783
0.6154	0.6013	0.4865	0.4592	0.3846	0.3987	-0.4865	- 0.4592
0.6154	0.5534	0.4865	0.3621	0.3846	0.4466	-0.4865	- 0.3621
0.6154	0.509	0.4865	0.2132	0.3846	0.4910	-0.4865	- 0.2132

Table 2.3.6: Flux of current through branches of the parallel network

10, the flow is shown in fig. 2.3.33 and 2.3.34 and we see that it is nearly uniformly distributed throughout the domain and therefore the asymptotic theory is not valid.

The last computation we present has the following parameters: $\mathbf{x}_1 = (2.85, 1.047)$, $\mathbf{x}_2 = (3.54, 1.047), \xi = (\pi, \pi), k_1^+ = 2.4, k_1^- = 1.4, k_2^+ = 2.8, k_2^- = 1., \rho(\mathbf{x}_1) = C(\mathbf{x}_2) = 42.5211$ (notice that we moved the saddle points). The contrasts for ρ and C were 200 and 300. The asymptotic theory predicts that this problem is equivalent to a parallel circuit with resistance $R = 42.5211 \cdot \sqrt{\frac{2.4}{1.4}} = 55.6732$ and capacitance $C = 42.5211 \cdot \sqrt{\frac{2.8}{1}} = 71.1514$. The real and imaginary current is split between the two regions and concentrates around the two saddle points. The effective impedance is given by $\overline{Z} = (\frac{1}{55.6732} + \frac{1}{i \cdot 71.1514})^{-1} = 34.4293 + i \cdot 26.9696$. The predicted constants α_i and β_i, defined in section 2.2.3, are $\alpha_1 = 0.6203$, $\beta_1 = -\beta_2 = 0.4853$ and $\alpha_2 = 0.3797$. Fig. 2.3.35 and 2.3.36 show the direction, and magnitude of the current in the domain and agree nicely with our analysis. The averages over regions I and II are $< \nabla^\perp u >_I = 0.6266 \cdot \mathbf{e}_1$, $< \nabla^\perp u >_{II} = 0.3734 \cdot \mathbf{e}_1$, $< \nabla^\perp v >_I = 0.3861 \cdot \mathbf{e}_1 = - < \nabla^\perp v >_{II}$, and agree closely with the asymptotic results. The numerical value of the effective impedance is $\overline{Z}_{num} = 32.9459 + i \cdot 28.0242$ which gives a relative error of 4.31% for the real part and 3.91% for the imaginary part.

From the results presented in this section we conclude that the network approximation introduced in section 2.2 is quite good for the effective impedance $\overline{Z}$ at high contrasts (i.e. $\geq 10^2$). When the contrast drops below 10^2 the network approximation is not so good.

4 Analysis based on variational principles

In this section we prove that in the asymptotic limit of infinitely high contrast the computation of the effective impedance can be reduced to the solution of an equivalent network of resistors and capacitors. The effective impedance is given by

$$\overline{Z} =< (\rho + iC)\mathbf{j} \cdot \mathbf{j} > \tag{2.4.1}$$

where $\rho(\mathbf{x}) = \rho_0 e^{-\frac{S(\mathbf{x})}{\epsilon^2}}$, $C(\mathbf{x}) = C_0 e^{-\frac{P(\mathbf{x})}{\epsilon^2}}$ and $\mathbf{j}$ is the complex current density which satisfies

$$\begin{aligned} \nabla^{\perp}[(\rho + iC)\mathbf{j}] &= 0 \\ \nabla \cdot \mathbf{j} &= 0 \\ < \mathbf{j} >&= \mathbf{e}_1, \end{aligned} \tag{2.4.2}$$

over the periodic cell Ω. The effective impedance can also be obtained from variational principles of saddle point type (2.1.24) and (2.1.25). The proofs presented in this section assume a logarithmic high contrast of the coefficients ρ and C, as $\epsilon \to 0$.

4.1 The high contrast approximation in the static case

We return to the problem considered in section 2.2.2 in the static, purely resistive circuit, with $\rho(\mathbf{x}) = \rho_0 e^{-\frac{S(\mathbf{x})}{\epsilon^2}}$. The function $S(\mathbf{x})$ is smooth and periodic. The geometry of the composite is sketched in figure 2.2.9. The resistance $\rho(\mathbf{x})$ has two minima at $\mathbf{x}_{m1}$ and $\mathbf{x}_{m2}$, two maxima at $\mathbf{x}_{M1}$ and $\mathbf{x}_{M2}$, and a saddle point $\mathbf{x}_s$. Near the saddle point we have

$$S(\mathbf{x}) \approx S(\mathbf{x}_s) + \frac{k^-(x - x_s)^2}{2} - \frac{k^+(y - y_s)^2}{2}. \tag{2.4.3}$$

Under these assumptions we state the following theorem:

Theorem 1. The effective resistance is given by

$$\overline{R} \approx \rho(\mathbf{x}_s)\sqrt{\frac{k^+}{k^-}}, \tag{2.4.4}$$

with the flow in the driving direction and concentrated around the saddle point $\mathbf{x}_s$.

The proof of this theorem is based on the variational principles and it was first given by Kozlov [54]. We define the direct cell problem

$$\begin{aligned} \nabla^{\perp} \cdot (\rho \mathbf{j}) &= 0 \\ < \mathbf{j} > &= \mathbf{e}_1 \\ \nabla \cdot \mathbf{j} &= 0 \end{aligned} \tag{2.4.5}$$

with the associated effective resistance

$$\overline{R} = < \rho \mathbf{j} \cdot \mathbf{j} >, \tag{2.4.6}$$

and the dual cell problem

$$\begin{aligned} \nabla \cdot (\frac{1}{\rho} \nabla \phi) &= 0 \\ < \nabla \phi > &= \mathbf{e}_1 \end{aligned} \tag{2.4.7}$$

with the effective conductivity

$$\overline{\sigma} = < \frac{1}{\rho} \nabla \phi \cdot \nabla \phi > . \tag{2.4.8}$$

The effective parameters $\overline{R}$, and $\overline{\sigma}$ can also be obtained from the Dirichlet-type variational principles

$$\overline{R} = \min_{<\nabla^{\perp} u> = \mathbf{e}_1} < \rho \nabla^{\perp} u \cdot \nabla^{\perp} u >, \tag{2.4.9}$$

$$\overline{\sigma} = \min_{<\nabla \phi> = \mathbf{e}_1} < \frac{1}{\rho} \nabla \phi \cdot \nabla \phi > \tag{2.4.10}$$

since the Euler equations associated with them are exactly (2.4.5), and (2.4.7). Note that in (2.4.9) we replaced the current density by $\mathbf{j} = \nabla^{\perp} u$, where u is the magnitude of the magnetic field which is perpendicular to the plane of Ω. We begin with a well known fact which we prove here for completeness.

Lemma 1. The effective parameters $\overline{R}$ and $\overline{\sigma}$ satisfy the relation $\overline{R} = \overline{\sigma}^{-1}$.

Proof of lemma 1. Define the quadratic form

$$\Phi(\mathbf{w}) = \frac{1}{2} \rho \mathbf{w} \cdot \mathbf{w} \tag{2.4.11}$$

and let its dual be

$$\Psi(\mathbf{z}) = \sup_{\mathbf{z}}(\mathbf{z}\cdot\mathbf{w} - \Phi(\mathbf{w})) = \frac{1}{2\rho}\mathbf{z}\cdot\mathbf{z}. \tag{2.4.12}$$

Then, assuming that we are in $\mathbb{R}^3$ so that we can use vector calculus

$$\phi(\mathbf{e}) = \frac{1}{2}\overline{R}\mathbf{e}\cdot\mathbf{e} = \inf_{\nabla\cdot\mathbf{w}=0,\ <\mathbf{w}>=\mathbf{e}} < \Phi(\mathbf{w}) > \tag{2.4.13}$$

and

$$\psi(\mathbf{e}) = \frac{1}{2}\overline{\sigma}\mathbf{e}\cdot\mathbf{e} = \inf_{\nabla\times\mathbf{z}=0,\ <\mathbf{z}>=\mathbf{e}} < \Psi(\mathbf{z}) > . \tag{2.4.14}$$

We want to show that

$$\psi(\mathbf{e}) = \phi^\star(\mathbf{e}) = \sup_{\mathbf{f}}(\mathbf{e}\cdot\mathbf{f} - \psi(\mathbf{f})), \tag{2.4.15}$$

which means that $\overline{\sigma} = 1/\overline{R}$. Note that

$$< \Psi(\mathbf{z}) > \geq < \mathbf{z}\cdot\mathbf{w} - \Phi(\mathbf{w}) > = \mathbf{e}\cdot\mathbf{f} - < \Phi(\mathbf{w}) > \tag{2.4.16}$$

for any periodic vector fields $\mathbf{z}$ and $\mathbf{w}$ such that $<\mathbf{z}>=\mathbf{f}$, $<\mathbf{w}>=\mathbf{e}$ and $\nabla\cdot\mathbf{w}=0$, $\nabla\times\mathbf{z}=0$. Thus

$$< \Psi(\mathbf{z}) > \geq \mathbf{e}\cdot\mathbf{f} - \inf_{\nabla\cdot\mathbf{w}=0,\ <\mathbf{w}>=\mathbf{e}} < \Phi(\mathbf{w}) > = \mathbf{e}\cdot\mathbf{f} - \phi(\mathbf{e}) \tag{2.4.17}$$

and hence

$$\psi(\mathbf{f}) \geq \mathbf{e}\cdot\mathbf{f} - \phi(\mathbf{e}) \tag{2.4.18}$$

which gives $\psi(\mathbf{f}) \geq \phi^\star(\mathbf{f})$.

To get the opposite inequality note that

$$\begin{aligned}\psi(\mathbf{f}) \quad &= \inf_{\nabla\times\mathbf{z}=0,\ <\mathbf{z}>=\mathbf{f}} < \Psi(\mathbf{z}) > \leq < \Psi(\mathbf{z}) > - < \mathbf{z}\cdot\mathbf{w} > + < \mathbf{z}\cdot\mathbf{w} > = \\ &\mathbf{e}\cdot\mathbf{f} - < \mathbf{z}\cdot\mathbf{w} - \Psi(\mathbf{z}) >\end{aligned} \tag{2.4.19}$$

for all periodic vector fields $\mathbf{z}$ and $\mathbf{w}$ such that $<\mathbf{z}>=\mathbf{f}$, $<\mathbf{w}>=\mathbf{e}$ and $\nabla\cdot\mathbf{w}=0$, $\nabla\times\mathbf{z}=0$. Let $\mathbf{z}$ be the minimizer that gives $\psi(\mathbf{f})$ which means that

$$\begin{aligned}\nabla\cdot(\frac{1}{\rho}\mathbf{z}) &= 0 \\ \nabla\times\mathbf{z} &= 0 \\ < \mathbf{z} > &= \mathbf{f}.\end{aligned} \tag{2.4.20}$$

Then if we let $\mathbf{w} = \frac{1}{\rho}\mathbf{z}$ we see that pointwise

$$\mathbf{z}\cdot\mathbf{w} - \Psi(\mathbf{z}) = \Phi(\mathbf{w}). \tag{2.4.21}$$

Let $<\mathbf{w}>=\tilde{\mathbf{e}}$. Then from (2.4.19)

$$\psi(\mathbf{f}) \leq \tilde{\mathbf{e}}\cdot\mathbf{f} - <\Phi(\mathbf{w})> \tag{2.4.22}$$

for this particular $\mathbf{w}$. Hence, since the left side of (2.4.22) does not depend on $\mathbf{w}$ we have

$$\psi(\mathbf{f}) \leq \tilde{\mathbf{e}}\cdot\mathbf{f} - \inf_{\nabla\cdot\mathbf{w}=0,\ <\mathbf{w}>=\tilde{\mathbf{e}}} <\Phi(\mathbf{w})> \tag{2.4.23}$$

which means that

$$\psi(\mathbf{f}) \leq \tilde{\mathbf{e}}\cdot\mathbf{f} - \phi(\tilde{\mathbf{e}}) \tag{2.4.24}$$

or $\psi(\mathbf{f}) \leq \phi^{\star}(\mathbf{f})$ which proves the lemma.

In order to prove Theorem 1, we will obtain an upper bound for $\overline{R}$ from (2.4.9) which we will match with a lower bound for $\overline{R}$ obtained from the dual variational principle (2.4.10).

If we select from the eligible fields $\nabla^{\perp}u$ in (2.4.9), those which are nonzero only in a neighborhood of $\mathbf{x}_s$, we obtain the inequality

$$\overline{R} \lesssim \min_{<\nabla^{\perp}u>_{\delta}=\mathbf{e}_1} \int_{|\mathbf{x}-\mathbf{x}_s|\leq\delta} \rho \mid \nabla^{\perp}u \mid^2 d\mathbf{x}, \tag{2.4.25}$$

where $<\nabla^{\perp}u>_{\delta}$ is the average of $\nabla^{\perp}u$ in the δ - neighborhood of the saddle point. From all the possible fields $\nabla^{\perp}u$ in (2.4.25) we choose those which have the component in the direction $\mathbf{e}_2$ equal to zero, so that $u = u(y)$ only, and therefore we obtain

$$\overline{R} \lesssim \int_{x_s-\delta}^{x_s+\delta} \rho(\mathbf{x}_s)\exp(-\frac{k^-(x-x_s)^2}{2\epsilon^2})dx \int_{y_s-\delta}^{y_s+\delta} \exp(\frac{k^+(y-y_s)^2}{2\epsilon^2})(\frac{du}{dy})^2 dy, \tag{2.4.26}$$

where $\int_{y_s-\delta}^{y_s+\delta}(-\frac{du}{dy})dy = 1$. We point out that the inequalities above are only asymptotic and depend on the parameter δ which is fixed as $\epsilon \to 0$. More precisely, $\overline{R} \lesssim F^{\epsilon,\delta}$ means $\overline{R} \leq F^{\epsilon,\delta}(1+o(1))$ with the small order one term tending to zero as $\epsilon \to 0$ with $\delta > 0$ fixed. After doing the x integration, (2.4.26) becomes

$$\overline{R} \lesssim \rho(\mathbf{x}_s)\sqrt{\frac{2\pi}{k^-}}\epsilon \min_{\chi} \int_{y_s-\delta}^{y_s+\delta} \exp(\frac{k^+(y-y_s)^2}{2\epsilon^2})(\frac{du}{dy})^2 dy. \tag{2.4.27}$$

We choose u in (2.4.27) to minimize the right side. Then u satisfies the Euler equation

$$\begin{aligned} \frac{d}{dy}[\exp(\frac{k^+(y-y_s)^2}{2\epsilon^2})\frac{du}{dy}] &= 0 \\ \int_{y_s-\delta}^{y_s+\delta}(-\frac{du}{dy})dy &= 1. \end{aligned} \tag{2.4.28}$$

Equations (2.4.28) are exactly the same as (2.2.20) and u is given by (2.2.22), which substituted in (2.4.27) gives the upper bound

$$\begin{aligned} \overline{R} \lesssim \rho(\mathbf{x}_s)\sqrt{\frac{2\pi}{k^-}}\epsilon\frac{1}{2\pi\epsilon^2}k^+\int_{y_s-\delta}^{y_s+\delta}\exp(\frac{k^+(y-y_s)^2}{2\epsilon^2}-\frac{k^+(y-y_s)^2}{\epsilon^2})dy = \\ \rho(\mathbf{x}_s)\sqrt{\frac{2\pi}{k^-}}\epsilon\frac{1}{2\pi\epsilon^2}k^+\sqrt{\frac{2\pi}{k^+}}\epsilon = \rho(\mathbf{x}_s)\sqrt{\frac{k^+}{k^-}}, \end{aligned} \tag{2.4.29}$$

This bound is gotten under the hypothesis that the current $\nabla^\perp u$ is concentrated around $\mathbf{x}_s$, and flows in the driving direction. To obtain a lower bound for $\overline{R}$ we use the dual formulation with the variational principle (2.4.10) and Lemma 1. In (2.4.10) we select fields $\nabla\phi$ which are concentrated around $\mathbf{x}_s$ and have nonzero components only in the $\mathbf{e}_1$ direction. The minimum over such fields can only give a larger value of the functional in (2.4.10) and we obtain

$$\overline{\sigma} \lesssim \min_\phi \int_{x_s-\delta}^{x_s+\delta}\rho^{-1}(\mathbf{x}_s)\exp(\frac{k^-(x-x_s)^2}{2\epsilon^2})(\frac{d\phi}{dx})^2 dx\int_{y_s-\delta}^{y_s+\delta}\exp(-\frac{k^+(y-y_s)^2}{2\epsilon^2})dy, \tag{2.4.30}$$

where $\int_{x_s-\delta}^{x_s+\delta}(\frac{d\phi}{dx})dx = 1$. The computation for the minimum in (2.4.30) is exactly the same as the one for the direct problem. By solving the Euler equation associated with (2.4.30) we obtain

$$\frac{d\phi}{dx} = \frac{1}{\sqrt{\frac{2\pi}{k^-}}\epsilon}\exp(-\frac{k^-(x-x_s)^2}{2\epsilon^2}) \tag{2.4.31}$$

and hence

$$\begin{aligned} \overline{\sigma} \lesssim \rho^{-1}(\mathbf{x}_s)\sqrt{\frac{2\pi}{k^+}}\epsilon\frac{1}{\frac{2\pi}{k^-}\epsilon^2}\int_{x_s-\delta}^{x_s+\delta}\exp(\frac{k^-(x-x_s)^2}{2\epsilon^2}-\frac{k^-(x-x_s)^2}{\epsilon^2})dx = \\ \rho^{-1}(\mathbf{x}_s)\sqrt{\frac{2\pi}{k^+}}\epsilon\frac{1}{\frac{2\pi}{k^-}\epsilon^2}\sqrt{\frac{2\pi}{k^-}}\epsilon. \end{aligned} \tag{2.4.32}$$

Using Lemma 1 and (2.4.32) we see that $\overline{R}$ satisfies

$$\overline{\sigma} = \overline{R}^{-1} \lesssim \rho^{-1}(\mathbf{x}_s)\sqrt{\frac{k^-}{k^+}}. \tag{2.4.33}$$

Combining (2.4.29), and (2.4.33) we get the asymptotic behavior of the effective resistance

$$\overline{R} \approx \rho(\mathbf{x}_s)\sqrt{\frac{k^+}{k^-}}. \tag{2.4.34}$$

Since we used a current $\nabla^{\perp} u$ in the $\mathbf{e}_1$ direction and concentrated around $\mathbf{x}_s$ to get (2.4.34), theorem 1 is proved.

4.2 High contrast approximation in the static case with many saddle points

We shall now describe how to analyze (2.2.1)-(2.2.2) and (2.2.3)-(2.2.4) when $\rho(\mathbf{x})$ has several, say $M \geq 2$, saddle points in Ω.

With each saddle point we associate an effective resistance $\overline{R}_j$, $j = 1, 2, \ldots, M$ given by the right side of (2.4.4). This comes from the local analysis around a saddle point that was just carried out in Theorem 1. To find the currents flowing through the saddle points we must specify how the effective saddle resistances are connected to each other. We do this by identifying the network associated with the resistance function $\rho(\mathbf{x})$ as follows.

With each minimum of the resistance $\rho(\mathbf{x})$ we associate a node of a network on the torus T^2 (which is the region Ω). The nodes are connected to adjacent nodes if there is a path between two nodes that goes over a single saddle. This path is a branch or a bond that connects two nodes. To avoid complicated terminology and notation we will assume that the network that is associated with the resistance is a rectangular lattice network as in the figure 2.4.37. Recall that the network is periodic.

Let the index $j \in N$ denote the set of nodes and I_{jk} be the current from node j to node k that is a neighbor of j, $k \in N_j$. Then $I_{jk} = -I_{kj}$ and

$$\sum_{k \in N_j} I_{jk} = 0, \ j \in N \tag{2.4.35}$$

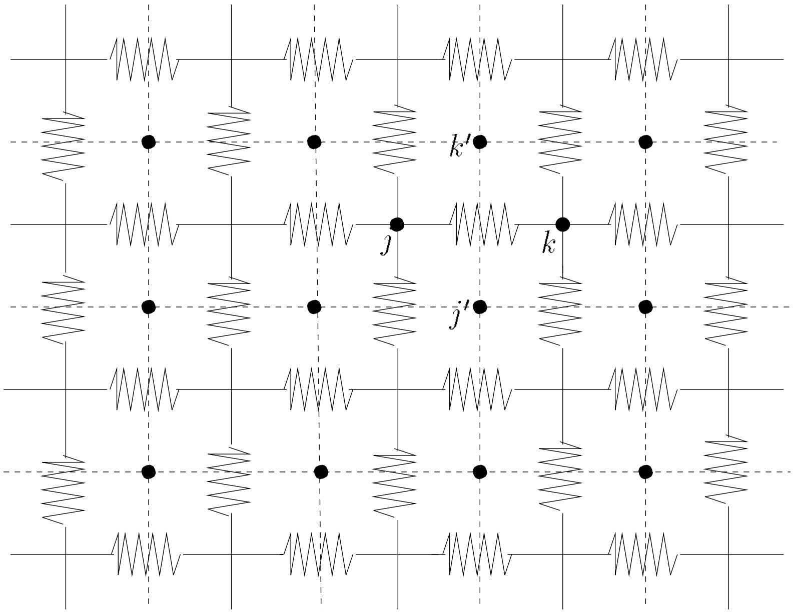

Figure 2.4.37: Periodic resistor network

which is the discrete analog of $\nabla \cdot \mathbf{j} = 0$, Kirchoff's current law for circuits when there are no sources or sinks of current in the network. We denote the resistance of the (j,k) bond by $\overline{R}_{jk}$ (and note that $\overline{R}_{kj} = \overline{R}_{jk}$).

With the above notation and Theorem 1 we now conclude that in the multi-saddle case the effective resistance (2.4.9) is bounded from above by

$$\overline{R} \lesssim \frac{1}{2} \sum_{j \in N} \sum_{k \in N_j} \overline{R}_{jk} I_{jk}^2 \tag{2.4.36}$$

where the factor 1/2 is needed because each bond is counted twice. We now minimize (2.4.36) subject to the condition (2.4.35) and the discrete analog of the driving condition $< \mathbf{j} >= \mathbf{e}$. If for example $\mathbf{e} = \mathbf{e}_1$, the unit vector in the x direction, we add to the currents I_{jk} satisfying (2.4.35) a constant current I in the horizontal direction so that the net current crossing any vertical line in Ω equals one while the net current crossing any horizontal line is zero. The equation that the minimizing currents must satisfy is from (2.4.36)

$$\sum_{j\in N}\sum_{k\in N_j}\overline{R}_{jk}I_{jk}\delta I_{jk}=0 \tag{2.4.37}$$

for every current perturbation δI_{jk} that satisfies (2.4.35) and has no net flow in the horizontal or vertical direction.

The implications of (2.4.37) are best analyzed by using the dual network which in the case of a rectangular network has the form shown in fig. 2.4.37 with broken lines. We denote by $j'\in N'$ the collection of dual nodes and by $N'_{k'}$ the collection of dual nodes adjacent to the dual node k'. The dual network is, of course, the one that is associated with the minima of $\rho^{-1}(\mathbf{x})$, the conductivity of the continuous medium.

A distribution of currents δI_{jk} that satisfies (2.4.35) and has no net flow in the x or y direction can be written in the form

$$\delta I_{jk}=H_{k'}-H_{j'} \tag{2.4.38}$$

in terms of a function $H_{j'}$ defined on the dual network. Here (j,k) and (j',k') are related to each other, as is shown in the figure, and the relation

$$\sum_{k\in N_j}\delta I_{jk}=0$$

is equivalent to

$$\sum_{j\ loop}\Delta H=0$$

which is the sum of H differences taken over the dual loop surrounding the node j.

We now use (2.4.38) in (2.4.37) and note that

$$0=\sum_{j\in N}\sum_{k\in N_j}\overline{R}_{jk}I_{jk}\delta I_{jk}=\sum_{j'\in N'}\Big(\sum_{k'\in N'_{j'}}(\overline{R}I)_{j'k'}\Big)H_{j'}. \tag{2.4.39}$$

This basic identity is the analog of integration by parts in the continuum case and says that the sum over nodes of the network can be replaced by a sum over loops of the voltage differences $(\overline{R}I)$ or, what is the same, a sum over the dual nodes. But in (2.4.39) the $H_{j'}$ are arbitrary since (2.4.38) must hold for all δI_{jk} subject to (2.4.35). Thus,

$$\sum_{k'\in N'_{j'}}(\overline{R}I)_{j'k'}=0,\ j'\in N' \tag{2.4.40}$$

which is Kirchoff's loop voltage-difference law for circuits. Equation (2.4.40), the current law (2.4.35) and the driving condition determine uniquely the minimizing currents I_{jk} in the upper bound (2.4.36).

To get the asymptotic equality of the effective resistance $\overline{R}$ of the original problem to the upper bound we just described we must show that the lower bound is the same as the upper bound. From Theorem 1 and Lemma 1, we know that we have the bound

$$\overline{R}^{-1} \lesssim \frac{1}{2} \sum_{j' \in N'} \sum_{k' \in N'_{j'}} \overline{R}^{-1}_{j'k'} V^2_{j'k'} \tag{2.4.41}$$

where $\overline{R}_{j'k'}$ is the resistance associated with the dual bond $(j'k')$ and equals $\overline{R}_{jk}$ from formula (2.4.4) for the saddle is associated with the bond (jk) in the network or $(j'k')$ in the dual network (see fig. 2.4.37). The potential differences $V_{j'k'}$ are defined on the dual network and satisfy the relation $V_{j'k'} = -V_{k'j'}$ as well as

$$\sum_{k' \in N'_{j'}} V_{j'k'} = 0, \ j' \in N' \tag{2.4.42}$$

which says that the potential differences around a loop (a dual node) vanish. The driving condition in (2.4.41) is that the net potential difference across any vertical line must equal one (driving in the x direction) while the one across any horizontal line is zero.

With these conditions on $V_{j'k'}$ we can now minimize (2.4.41) and we find, using the basic identity (2.4.39) again, Kirchoff's current law for the minimizing potential differences

$$\sum_{k \in N_j} \overline{R}^{-1}_{jk} V_{jk} = 0, \ j \in N. \tag{2.4.43}$$

But (2.4.42) and (2.4.43) are exactly the same equations as (2.4.35) and (2.4.40) so, up to scaling by the overall effective resistance, it is clear that the upper bound (2.4.41) is the same as the reciprocal of the upper bound (2.4.36) and this proves the asymptotic form of the effective resistance $\overline{R}$ as the one associated with the resistances (2.4.4) in the network formed from the minima (nodes) of the resistance function $\rho(\mathbf{x})$.

4.3 The effective impedance of a composite with high contrast coefficients, in the quasistatic limit. Case A: Series connection

In this section we consider the problem defined in section 2.2.3 case A. We study the direct problem (2.1.13) with coefficients $\rho(\mathbf{x}) = \rho_0 e^{-\frac{S(\mathbf{x})}{\epsilon^2}}$ and $C(\mathbf{x}) = C_0 e^{-\frac{P(\mathbf{x})}{\epsilon^2}}$ defined over a region Ω with the geometry shown in fig. 2.2.11. The functions $S(\mathbf{x})$ and $P(\mathbf{x})$ are smooth, ρ_0 and C_0 are constants and ϵ is a small parameter. The domain Ω is divided in two regions by a curve L. In region I the resistance dominates ($\rho \gg C$), in region II $C \gg \rho$ and along curve L $\rho = C$. We assume that the resistance $\rho(\mathbf{x})$ has a single saddle $\mathbf{x}_1$ in region I and that the capacitance $C(\mathbf{x})$ has a single saddle $\mathbf{x}_2$ in region II. Both saddles are oriented in the x direction. The current density is divergence free and can be written as $\mathbf{j} = \nabla^{\perp}(u + iv)$, where u and v are the real and imaginary parts of the magnetic field which is perpendicular on the plane Ω. In section 2.2.3 case A we stated that when we have a driving in the x direction (i.e. $<\mathbf{j}>= \mathbf{e}_1$), in the asymptotic limit $\epsilon \to 0$ we have an equivalent series circuit consisting of a resistance $\overline{R}$ placed at the saddle $\mathbf{x}_1$ connected with a capacitance $i\overline{C}$ placed at the saddle $\mathbf{x}_2$. In this section we use the variational principles (2.1.24) and (2.1.25) to prove this result.

In the vicinity of the saddle points $\mathbf{x}_1$ and $\mathbf{x}_2$ we have
for $\mathbf{x} \in \delta N(\mathbf{x}_1)$:

$$\begin{aligned} \rho(\mathbf{x}) &\approx \rho(\mathbf{x}_1)\exp(-\frac{k_1^-(x-x_1)^2}{2\epsilon^2} + \frac{k_1^+(y-y_1)^2}{2\epsilon^2}) \\ C(\mathbf{x}) &\approx 0, \end{aligned} \tag{2.4.44}$$

for $\mathbf{x} \in \delta N(\mathbf{x}_2)$:

$$\rho(\mathbf{x}) \approx 0$$

$$C(\mathbf{x}) \approx C(\mathbf{x}_2)\exp(\frac{-k_2^-(x-x_2)^2}{2\epsilon^2}+\frac{k_2^+(y-y_2)^2}{2\epsilon^2}). \tag{2.4.45}$$

In order to prove the series connection result we have to show that real$(\overline{Z}) = \overline{R}$ and imag$(\overline{Z}) = \overline{C}$. This is done by obtaining matching lower and upper bounds on the effective impedance $\overline{Z}$. For example, in order to obtain an upper bound on real$(\overline{Z})$ we will choose some particular real current field $\nabla^{\perp}u$ and then perform the maximization over all the eligible imaginary current fields. From the previous results, we have some good clues about what choice of a real current to make. The current averaged over the whole domain should be $\mathbf{e}_1$, therefore the function $v(x,y)$ is periodic in the domain, whereas the real current can be rewritten with the help of a periodic function $\phi(x,y)$ as $\nabla^{\perp}u = \mathbf{e}_1 + \nabla^{\perp}\phi$. We notice that our domain has in the vertical direction the same boundaries as its component regions I and II and we use the periodicity in y of ϕ and v to show that the currents in the x direction averaged over regions I or II satisfy

$$\begin{aligned}
\frac{1}{A_I}\int_I(-u_y)dxdy &= \frac{1}{A_I}\int_I(1-\phi_y)dxdy = 1, \quad \frac{1}{A_I}\int_I(-v_y)dxdy = 0, \\
\frac{1}{A_{II}}\int_{II}(-u_y)dxdy &= \frac{1}{A_{II}}\int_{II}(1-\phi_y)dxdy = 1, \quad \frac{1}{A_{II}}\int_{II}(-v_y)dxdy = 0,
\end{aligned} \tag{2.4.46}$$

where A_I and A_{II} are the areas of regions I and II. The currents in the y direction can have different averages as long as they algebraically add to zero. However in this problem both ρ and C have a single saddle point in regions I and II. From the results presented in sections 2.2.2 and 2.4.1 we know that all the current is concentrated around these saddle points. Consider for example $\mathbf{x}_1$, where the function ρ has a minimum in the y direction and a maximum in the x direction. The current will have x component $-u_y$ concentrated around $\mathbf{x}_1$, but the y component u_x should be small. The only place where we could have flow in the y direction would be away from the saddle point, where according to Theorem 1 it should be negligible. The same conclusion applies to region II.

In order to obtain an upper bound on real($\overline{Z}$), we choose the following real current

$$\nabla^{\perp} u = \begin{cases} \left(\frac{1}{\sqrt{\frac{2\pi}{k_1^+}}\epsilon} \exp\left(-\frac{k_1^+ (y-y_1)^2}{2\epsilon^2}\right), 0\right) & \forall \mathbf{x} \in \delta N(\mathbf{x}_1) \\ \left(\frac{1}{\sqrt{\frac{2\pi}{k_2^+}}\epsilon} \exp\left(-\frac{k_2^+ (y-y_2)^2}{2\epsilon^2}\right), 0\right) & \forall \mathbf{x} \in \delta N(\mathbf{x}_2) \\ \mathbf{0} & \text{otherwise} \end{cases} \tag{2.4.47}$$

which is clearly divergence free, and satisfies

$$< \nabla^{\perp} u > = < \nabla^{\perp} u >_I = < \nabla^{\perp} u >_{II} = \mathbf{e}_1, \tag{2.4.48}$$

where $< \cdot >$ stands for the normalized average over the indicated region. We use (2.4.47) in the variational principle (2.1.24) to obtain

$$\begin{aligned} \text{real}(\overline{Z}) \lesssim \max_{<\nabla^{\perp} v> = \mathbf{0}} & \left[\int_{\delta N^I} \rho(\mathbf{x}_1) e^{-\frac{k_1^-(x-x_1)^2}{2\epsilon^2} + \frac{k_1^+(y-y_1)^2}{2\epsilon^2}} \frac{1}{\frac{2\pi}{k_1^+}\epsilon^2} e^{-\frac{2k_1^+(y-y_1)^2}{2\epsilon^2}} d\mathbf{x} - \right. \\ & \left. 2\int_{\delta N^{II}} C \frac{du}{dy} v_y d\mathbf{x} - < \rho(v_x^2 + v_y^2) > \right]. \end{aligned} \tag{2.4.49}$$

We take $\delta N(\mathbf{x}_i)$ to be the squares $\mid x - x_i \mid < \delta$ and $\mid y - y_i \mid < \delta$, $i = 1, 2$ where the small parameter δ is fixed, so as $\epsilon \to 0$ we have $\frac{\delta}{\epsilon} \to \infty$. The first integral in (2.4.49) is

$$\begin{aligned} \int_{\delta N^I} \rho\left(\frac{du}{dy}\right)^2 d\mathbf{x} & \approx \frac{\rho(\mathbf{x}_1)}{\frac{2\pi}{k_1^+}\epsilon^2} \int_{|x-x_1|<\delta} e^{-\frac{k_1^-(x-x_1)^2}{2\epsilon^2}} dx \int_{|y-y_1|<\delta} e^{-\frac{k_1^+(y-y_1)^2}{2\epsilon^2}} dy \approx \\ & \rho(\mathbf{x}_1)\sqrt{\frac{k_1^+}{k_1^-}} = \overline{R}. \end{aligned} \tag{2.4.50}$$

Since the maximum over a sum of functionals is less than the sum of the maxima we have

$$\text{real}(\overline{Z}) \lesssim \overline{R} + \max_{<\nabla^{\perp} v> = \mathbf{0}} \left(- < \rho(v_x^2 + v_y^2) >\right) + \max_{<\nabla^{\perp} v> = \mathbf{0}} \left(-2\int_{\delta N(\mathbf{x}_2)} C(\mathbf{x}) \frac{du}{dy} v_y d\mathbf{x}\right). \tag{2.4.51}$$

The trial field $\nabla^{\perp}u$ is zero in the region $II \setminus \delta N(\mathbf{x}_2)$ so

$$\int_{\delta N^{II}} C\frac{du}{dy}v_y d\mathbf{x} = \int_{II} C\frac{du}{dy}v_y d\mathbf{x} = \int_{II}\frac{\partial}{\partial y}[C\frac{du}{dy}v]d\mathbf{x} - \int_{II} v\frac{\partial}{\partial y}[C\frac{du}{dy}]d\mathbf{x}. \quad (2.4.52)$$

From the periodicity in y of $C\nabla^{\perp}uv$ and equation $\frac{\partial}{\partial y}(C\frac{du}{dy}) = 0$ satisfied by the trial field (2.4.47) we obtain that

$$\int_{\delta N^{II}} C\frac{du}{dy}v_y d\mathbf{x} \approx 0. \quad (2.4.53)$$

We should point out that the argument above is not quite right because the real current $\nabla^{\perp}u$ defined by (2.4.47) is discontinuous at the boundaries of $\delta N(\mathbf{x}_2)$ so in order to perform the integration by parts in (2.4.52) we must smooth it out. We introduce the cutoff function

$$\chi_2(y) = \begin{cases} 1 \ for \mid y - y_2 \mid < \delta \\ \\ 0 \ for \mid y - y_2 \mid > \delta + \eta \end{cases}$$

where $\chi_2(y)$ decays smoothly to zero over the region $\delta \leq \mid y - y_2 \mid \leq \delta + \eta$. We modify the trial field $\nabla^{\perp}u$ in region II to be

$$\nabla^{\perp}u = \frac{1}{\sqrt{\frac{2\pi}{k_2^+}}\epsilon} e^{-\frac{k_2^+(y-y_2)^2}{2\epsilon^2}} \chi_2(y)\mathbf{e}_1.$$

This is still consistent with $< \nabla^{\perp}u >_{II} = \mathbf{e}_1$, $\nabla \cdot (\nabla^{\perp}u) = 0$ and the periodicity in y of the real current. Since v is also periodic in y we obtain from (2.4.52)

$$\int_{\delta N^{II}} C\frac{du}{dy}v_y d\mathbf{x} = -\int_{II} v\frac{\partial}{\partial y}[C\frac{du}{dy}]d\mathbf{x} \approx$$
$$\frac{C(\mathbf{x}_2)}{\sqrt{\frac{2\pi}{k_2^+}}\epsilon}\int_{\delta \leq |y-y_2| \leq \delta+\eta}\int_{|x-x_2|\leq\delta} e^{-\frac{k_2^-(x-x_2)^2}{2\epsilon^2}}\frac{d\chi_2}{dy}v(x,y)dxdy. \quad (2.4.54)$$

The function $v(\cdot)$ is bounded and after evaluating the Gaussian integral over x we have

$$\int_{\delta N^{II}} C\frac{du}{dy}v_y d\mathbf{x} \approx C(\mathbf{x}_2)\sqrt{\frac{k_2^+}{k_2^-}}\int_{\delta \leq |y-y_2| \leq \delta+\eta} v(x_2,y)\frac{d\chi_2}{dy}dy. \quad (2.4.55)$$

By assumption $\frac{d\chi_2}{dy}$ is also bounded so from (2.4.55) we have

$$| \int_{\delta N^{II}} C\frac{du}{dy}v_y d\mathbf{x} \mid \lesssim K\eta, \tag{2.4.56}$$

where K is a bounded constant. In conclusion, we can make the integral in (2.4.56) arbitrary small by choosing η small enough, so inequality (2.4.51) reduces to

$$\text{real}(\overline{Z}) \lesssim \overline{R} + \max_{<\nabla^\perp v>_I = \mathbf{0}} [- \int_I \rho \mid \nabla^\perp v \mid^2 d\mathbf{x}]. \tag{2.4.57}$$

The Euler equation for the maximum in (2.4.57) is

$$\begin{aligned} \nabla^\perp \cdot (\rho \nabla^\perp v) &= 0 \quad \forall \mathbf{x} \in \text{region} I \\ < \nabla^\perp v >_I &= \mathbf{0} \end{aligned} \tag{2.4.58}$$

and has the solution $\nabla^\perp v = \mathbf{0}$. Thus,

$$\text{real}(\overline{Z}) \lesssim \overline{R}. \tag{2.4.59}$$

To get a lower bound on real($\overline{Z}$) we choose in (2.1.24) the imaginary current $\nabla^\perp v = \mathbf{0}$, and therefore

$$\text{real}(\overline{Z}) \geq \min_{<\nabla^\perp u> = \mathbf{e}_1} < \rho \mid \nabla^\perp u \mid^2 > . \tag{2.4.60}$$

This is exactly the problem studied in section 2.4.1, so we write directly the result given by Theorem 1

$$\text{real}(\overline{Z}) \gtrsim \overline{R}. \tag{2.4.61}$$

The lower bound on real($\overline{Z}$) given by (2.4.61) matches the upper bound (2.4.59) so real($\overline{Z}$) $\approx \overline{R} = \rho(\mathbf{x}_1)\sqrt{\frac{k_1^+}{k_1^-}}$. This result was obtained with a real current, concentrated around the critical points $\mathbf{x}_1, \mathbf{x}_2$ and flowing in the driving direction $\mathbf{e}_1$. The current averaged over our domain, or over regions I, or II is equal to $\mathbf{e}_1$. The analysis for the imag($\overline{Z}$) is exactly the same, and we obtain

$$\text{imag}(\overline{Z}) \approx \overline{C} = C(\mathbf{x}_2)\sqrt{\frac{k_2^+}{k_2^-}}. \tag{2.4.62}$$

This completes the analysis of the network approximation for the quasistatic case with one saddle point in the capacitive and resistive region, respectively, in a series configuration.

4.4 The effective impedance of a composite with high contrast coefficients, in the quasistatic limit. Case B: Parallel connection

In this section we consider the problem defined in section 2.2.3 case B. We study the direct problem (2.1.13) with coefficients $\rho(\mathbf{x}) = \rho_0 e^{-\frac{S(\mathbf{x})}{\epsilon^2}}$ and $C(\mathbf{x}) = C_0 e^{-\frac{P(\mathbf{x})}{\epsilon^2}}$ defined over a region Ω with the geometry shown in fig. 2.2.14. The functions $S(\mathbf{x})$ and $P(\mathbf{x})$ are smooth, ρ_0 and C_0 are constants and ϵ is a small parameter. The domain Ω is divided in two regions by a curve L. In region I the resistance dominates ($\rho \gg C$), in region II $C \gg \rho$ and along curve L $\rho = C$. We assume that the resistance $\rho(\mathbf{x})$ has a single saddle $\mathbf{x}_1$ in region I and that the capacitance $C(\mathbf{x})$ has a single saddle $\mathbf{x}_2$ in region II. Both saddles are oriented in the x direction. The current density can be written as $\mathbf{j} = \nabla^\perp(u + iv)$, where u and v are the real and imaginary parts of the magnetic field which is perpendicular on the plane Ω. In section 2.2.3 case B we stated that when we have a driving in the x direction (i.e. $< \mathbf{j} >= \mathbf{e}_1$), in the asymptotic limit $\epsilon \to 0$ we have an equivalent parallel circuit consisting of a resistance $\overline{R}$ placed at the saddle $\mathbf{x}_1$ connected with a capacitance $i\overline{C}$ placed at the saddle $\mathbf{x}_2$. In this section we use the variational principles (2.1.24) and (2.1.25) to prove this result.

In the vicinity of the saddle points $\mathbf{x}_1$ and $\mathbf{x}_2$ the coefficients $\rho(\mathbf{x})$ and $C(\mathbf{x})$ are given by

for $\mathbf{x} \in \delta N(\mathbf{x}_1)$:

$$\begin{aligned} \rho(\mathbf{x}) &\approx \rho(\mathbf{x}_1)\exp(-\frac{k_1^-(x-x_1)^2}{2\epsilon^2} + \frac{k_1^+(y-y_1)^2}{2\epsilon^2}) \\ C(\mathbf{x}) &\approx 0, \end{aligned} \tag{2.4.63}$$

for $\mathbf{x} \in \delta N(\mathbf{x}_2)$:

$$\rho(\mathbf{x}) \approx 0$$

$$C(\mathbf{x}) \approx C(\mathbf{x}_2)\exp(-\frac{k_2^-(x-x_2)^2}{2\epsilon^2} + \frac{k_2^+(y-y_2)^2}{2\epsilon^2}). \tag{2.4.64}$$

In order to show the parallel connection we must show that $\overline{Z} \approx (\frac{1}{R} + \frac{1}{iC})^{-1}$. This is done by getting matching lower and upper bounds on the effective impedance $\overline{Z}$. In order to obtain an upper bound on real($\overline{Z}$) we choose in the varia tional principle (2.1.24) a particular real current $\nabla^\perp u$ and then perform the maximization over the imaginary current. The experience gained from studying the static case suggests that the current should be concentrated around the critical points $\mathbf{x}_1$ and $\mathbf{x}_2$. The current averaged over the whole domain should be $\mathbf{e}_1$, and therefore the function v which appears in the expression of the imaginary current must be periodic in Ω. The real current can be written as $\nabla^\perp u = \mathbf{e}_1 + \nabla^\perp \chi$, where χ is also a periodic function in Ω. We notice that the domain shown in fig. 2.2.14 has in the horizontal direction the same boundaries as its component regions I and II. Consequently, the periodicity over x of both χ, and v tells us that the average of the currents in the y direction over each one of the regions will be

$$\begin{aligned} \frac{1}{A_I}\int_I u_x dxdy = \frac{1}{A_I}\int_I \chi_x dxdy = 0, \quad \frac{1}{A_I}\int_I v_x dxdy = 0, \\ \frac{1}{A_{II}}\int_{II} v_x dxdy = \frac{1}{A_{II}}\int_{II} \chi_x dxdy = 0, \quad \frac{1}{A_{II}}\int_{II} v_x dxdy = 0 \end{aligned} \tag{2.4.65}$$

where A_I and A_{II} are the areas of regions I and II. The currents in the x direction can have different averages which must satisfy

$$\begin{aligned} &< -u_y >_I + < -u_y >_{II} = 1 \\ &< -v_y >_I + < -v_y >_{II} = 0. \end{aligned} \tag{2.4.66}$$

We choose as a real current trial field

$$\nabla^\perp u = \begin{cases} I_1(\frac{1}{\sqrt{\frac{2\pi}{k_1^+}}\epsilon}\exp(-\frac{k_1^+(y-y_1)^2}{2\epsilon^2}), 0) & \forall \mathbf{x} \in \delta N(\mathbf{x}_1) \\ I_2(\frac{1}{\sqrt{\frac{2\pi}{k_2^+}}\epsilon}\exp(-\frac{k_2^+(y-y_2)^2}{2\epsilon^2}), 0) & \forall \mathbf{x} \in \delta N(\mathbf{x}_2) \\ \mathbf{0} \quad \text{otherwise} \end{cases} \tag{2.4.67}$$

which is clearly divergence free. The constants $I_i,\ i = 1, 2$ are the flux of real current through each saddle and according to (2.4.66) they must satisfy

$$I_1 + I_2 = 1. \tag{2.4.68}$$

Equation (2.4.68) is Kirchoff's current law coming from the divergence free condition imposed on the real current. We use (2.4.67) in the variational principle (2.1.24) and obtain

$$\mathrm{real}(\overline{Z}) \lesssim \min_{I_i} \max_{<\nabla^\perp v>=\mathbf{0}} \quad [\quad \int_{\delta N^I} \rho(\mathbf{x}_1) e^{-\frac{k_1^-(x-x_1)^2}{2\epsilon^2} + \frac{k_1^+(y-y_1)^2}{2\epsilon^2}} \frac{I_1^2}{\frac{2\pi}{k_1^+}\epsilon^2} e^{-\frac{2k_1^+(y-y_1)^2}{2\epsilon^2}} d\mathbf{x} - \tag{2.4.69}$$

$$2 < C\nabla^\perp u \cdot \nabla^\perp v >_{II} - < \rho \mid \nabla^\perp v \mid^2 >].$$

The neighborhoods of $\mathbf{x}_1$ and $\mathbf{x}_2$ are the squares $\mid x - x_i \mid < \delta,\ \mid y - y_i \mid < \delta,\ i = 1, 2$ where the small parameter δ is fixed, so as $\epsilon \to 0$ we have $\frac{\delta}{\epsilon} \to \infty$. The first term in (2.4.69) is a Gaussian integral which gives

$$\int_{\delta N(\mathbf{x}_1)} \rho \mid \nabla^\perp u \mid^2 d\mathbf{x} \quad \approx \quad \frac{I_1^2}{\frac{2\pi}{k_1^+}\epsilon^2} \rho(\mathbf{x}_1) \int_{\delta N^I} \exp\left(-\frac{-k_1^-(x-x_1)^2}{2\epsilon^2} - \frac{k_1^+(y-y_1)^2}{2\epsilon^2}\right) \approx \tag{2.4.70}$$

$$I_1^2 \rho(\mathbf{x}_1) \sqrt{\frac{k_1^+}{k_1^-}} = \overline{R} I_1^2.$$

From (2.4.65) and (2.4.66) we know that the imaginary current in the x direction $(\nabla^\perp v \cdot \mathbf{e}_1 = -v_y)$ satisfies

$$< -v_y >_I + < -v_y >_{II} = 0$$

whereas the current in the y direction $(\nabla^\perp v \cdot \mathbf{e}_2 = v_x)$ averages to zero in both regions I and II. We introduce the constants J_1 and J_2 which are the fluxes of imaginary current in each region, $< -v_y >_I = J_1$ and $< -v_y >_{II} = J_2$. The average currents must satisfy

$$J_1 + J_2 = 0, \tag{2.4.71}$$

which is Kirchoff's current law coming from the divergence free condition imposed on $\nabla^\perp v$.

In order to evaluate the integral over $\delta N(\mathbf{x}_2)$ in (2.4.69) we focus on the current in region II and observe that we can rewrite it as

$$\nabla^{\perp} v = J_2 \mathbf{e_1} + \nabla^{\perp}\psi \tag{2.4.72}$$

where ψ is periodic in region II. We also know that $< \nabla^{\perp} u >= I_2 \mathbf{e_1}$ or

$$\nabla^{\perp} u = I_2 \mathbf{e_1} + \nabla^{\perp}\chi \tag{2.4.73}$$

where χ is periodic in region II. From (2.4.72) and (2.4.73) we have

$$\begin{aligned}\int_{\delta N(\mathbf{x}_2)} C\nabla^{\perp}u\cdot\nabla^{\perp}v d\mathbf{x} = J_2\int_{\delta N(\mathbf{x}_2)} C\nabla^{\perp}u\cdot\mathbf{e}_1 d\mathbf{x} + \int_{\delta N(\mathbf{x}_2)} C\nabla^{\perp}u\cdot\nabla^{\perp}\psi d\mathbf{x} = \\ \frac{J_2}{I_2}\int_{\delta N(\mathbf{x}_2)} C\nabla^{\perp}u\cdot(I_2\mathbf{e}_1+\nabla^{\perp}\chi)d\mathbf{x} + \int_{\delta N(\mathbf{x}_2)} C\nabla^{\perp}u\cdot\nabla^{\perp}(\psi-\frac{J_2}{I_2}\chi)d\mathbf{x} = \\ \frac{J_2}{I_2}\int_{\delta N(\mathbf{x}_2)} C\mid\nabla^{\perp}u\mid^2 d\mathbf{x} + \int_{\delta N(\mathbf{x}_2)} C\nabla^{\perp}u\cdot\nabla^{\perp}(\psi-\frac{J_2}{I_2}\chi)d\mathbf{x}.\end{aligned} \tag{2.4.74}$$

We use the definition (2.4.67) of the real current and obtain after simple computations

$$\int_{\delta N(\mathbf{x}_2)} C\nabla^{\perp}u\cdot\nabla^{\perp}v d\mathbf{x} \approx \frac{J_2}{I_2}C(\mathbf{x}_2)\sqrt{\frac{k_2^+}{k_2^-}}I_2^2 + \int_{\delta N(\mathbf{x}_2)} C\frac{du}{dy}\frac{\partial}{\partial y}(\psi-\frac{J_2}{I_2}\chi)d\mathbf{x}. \tag{2.4.75}$$

Since $\psi - \frac{J_2}{I_2}\chi$ is periodic in region II, the last integral in (2.4.75) is similar to (2.4.53) which was studied in section 2.4.3 and shown to be negligible. We use the notation $\overline{C} = C(\mathbf{x}_2)\sqrt{\frac{k_2^+}{k_2^-}}$ and from (2.4.69), (2.4.70) and (2.4.75) we have

$$\text{real}(\overline{Z}) \lesssim \min_{I_i}\max_{J_i}[\overline{R}I_1^2 - 2\overline{C}I_2J_2 - \min_{<\nabla^{\perp}v>=J_1\mathbf{e}_1} <\rho\mid\nabla^{\perp}v\mid^2>_I]. \tag{2.4.76}$$

The minimization over region I is similar to the static problem considered in section 2.4.1, therefore

$$\min_{<\nabla^{\perp}v>=J_1\mathbf{e}_1} <\rho\mid\nabla^{\perp}v\mid^2>_I \approx \overline{R}J_1^2. \tag{2.4.77}$$

Thus, the upper bound on the real part of the effective impedance is

$$\text{real}(\overline{Z}) \lesssim \min_{I_i}\max_{J_i}[\overline{R}I_1^2 - 2\overline{C}I_2J_2 - \overline{R}J_1^2], \tag{2.4.78}$$

where the currents I_i and J_i, $i = 1, 2$ satisfy Kirchoff's current laws (2.4.68) and (2.4.71), respectively.

In order to obtain a lower bound on real($\overline{Z}$) we choose an imaginary current field

$$\nabla^{\perp} v = \begin{cases} J_1\left(\frac{1}{\sqrt{\frac{2\pi}{k_1^+}}\epsilon}\exp\left(-\frac{k_1^+(y-y_1)^2}{2\epsilon^2}\right),0\right) & \forall \mathbf{x} \in \delta N(\mathbf{x}_1) \\ \\ J_2\left(\frac{1}{\sqrt{\frac{2\pi}{k_2^+}}\epsilon}\exp\left(-\frac{k_2^+(y-y_2)^2}{2\epsilon^2}\right),0\right) & \forall \mathbf{x} \in \delta N(\mathbf{x}_2) \\ \\ \mathbf{0} \quad \text{otherwise} \end{cases} \tag{2.4.79}$$

which satisfies the divergence free condition and averages to zero ($< \nabla^{\perp} v >= \mathbf{0}$). We substitute (2.4.79) in the variational principle (2.1.24) and after performing similar computations we get a lower bound on real($\overline{Z}$) which matches the upper bound (2.4.78). Consequently,

$$\text{real}(\overline{Z}) \approx \min_{I_i} \max_{J_i} [\overline{R} I_1^2 - 2\overline{C} I_2 J_2 - \overline{R} J_1^2]. \tag{2.4.80}$$

A similar analysis applied to the imaginary part of $\overline{Z}$ (i.e. variational principle (2.1.25)) leads to the same currents I_i and J_i, $i = 1, 2$ and the discrete variational formulation

$$\text{imag}(\overline{Z}) \approx \min_{I_i} \max_{J_i} [\overline{C} I_1^2 + 2\overline{R} I_1 J_1 - \overline{C} J_1^2]. \tag{2.4.81}$$

The equations that the currents must therefore satisfy are

$$\begin{cases} \overline{R} I_1 \delta I_1 - \overline{C} J_2 \delta I_2 = 0 \\ \\ \overline{C} I_2 \delta J_2 + \overline{R} J_1 \delta J_1 = 0 \end{cases} \tag{2.4.82}$$

where the perturbation currents δI_i and δJ_i, $i = 1, 2$ are arbitrary but must satisfy Kirchoff's current laws

$$\begin{cases} \delta I_1 + \delta I_2 = 0 \\ \\ \delta J_1 + \delta J_2 = 0. \end{cases} \tag{2.4.83}$$

From (2.4.82) and 2.4.83) we obtain

$$\begin{cases} \overline{R} I_1 = -\overline{C} J_2 \\ \\ \overline{C} I_2 = \overline{R} J_1, \end{cases} \tag{2.4.84}$$

which are Kirchoff's loop voltage-difference law (discrete version of condition $\nabla \cdot [(\rho + iC)\mathbf{j}] = 0$). From (2.4.84) and the driving conditions (2.4.68) and (2.4.71) we obtain the currents

$$\begin{aligned} I_1 &= \frac{\overline{C}^2}{\overline{R}^2 + \overline{C}^2}, \\ J_1 &= \frac{\overline{RC}}{\overline{R}^2 + \overline{C}^2}, \\ I_2 &= \frac{\overline{R}^2}{\overline{R}^2 + \overline{C}^2}, \\ J_2 &= -\frac{\overline{RC}}{\overline{R}^2 + \overline{C}^2}. \end{aligned} \tag{2.4.85}$$

Substituting these in the variational principles (2.4.80) and (2.4.81) we obtain

$$\overline{Z} \approx \left(\frac{1}{\overline{R}} + \frac{1}{i\overline{C}}\right)^{-1} \tag{2.4.86}$$

which is the effective impedance of the parallel network.

This completes the analysis of the network approximation for the quasistatic case with one saddle point in the capacitive and resistive region, respectively, in a parallel configuration.

5 Summary

In this chapter we have shown both analytically and numerically that the effective resistance and capacitance of a high contrast material can be approximated well by a resistor-capacitor (R-C) network. In the static case where the network consists of resistors only, this can be done in general for any number of saddle points of the resistance function $\rho(\mathbf{x})$, around which the current concentrates. Variational principles play an essential role in the analysis. We have restricted attention to two dimensional problems but the results are general and can be extended easily to any number of dimensions [54].

The asymptotic theory presented in this chapter tells us how to construct R and C networks in each region but it is not clear in general how they should be connected to each other. We can, however, use our methods to get upper and lower bounds for the effective resistance and capacitance that remain sharp in the high contrast limit but do not necessarily converge to each other.

Chapter 3

The inverse problem

Let Ω be a bounded two-dimensional region with conductivity $\sigma(x, y)$ and resistance (or impedance) $\rho(x, y) = \frac{1}{\sigma(x,y)}$. The recovery of σ from measurements of the potential ϕ at the boundary $\partial\Omega$ is the impedance tomography problem. The potential ϕ is the solution of the boundary value problem

$$\begin{aligned} \nabla \cdot (\sigma \nabla \phi) &= 0 \quad \text{in} \quad \Omega \\ \sigma \frac{\partial \phi}{\partial n} &= I \quad \text{on} \quad \partial\Omega, \end{aligned} \tag{3.0.1}$$

where the imposed surface current density I satisfies $\int_{\partial\Omega} IdS = 0$ and the potential ϕ is unique up to a constant. When the conductivity σ is sufficiently smooth and the full Neumann to Dirichlet map is known, that is, measurements of ϕ are given on $\partial\Omega$ for all possible current source distributions I, then it is known that the conductivity can be recovered in principle [52, 70, 71]. An extensive review of the uniqueness and stability of the impedance tomography problem is given in [42]. There is also an extensive literature on recovery algorithms, based mostly on linear output least-squares methods, that work well for low contrast or linearized conductivity problems [1, 9, 25, 43, 61, 65, 67, 73]. Electromagnetic impedance tomography, in which σ in (3.0.1) is complex valued, is also of interest in geophysical applications [5] but there is relatively little theoretical development for it at present. In this chapter we consider the impedance tomography problem with static (d.c.) boundary excitation and real valued conductivity. A possible configuration of current sources and points where the potential is measured, on part of the boundary of a square region, is shown in Fig. 3.0.1.

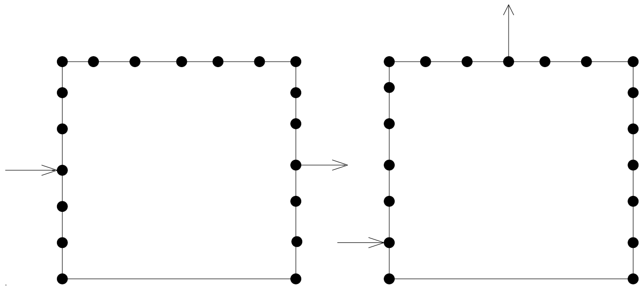

Figure 3.0.1: An impedance tomography problem for a square region Ω. The arrows represent current sources and the dots represent points where the potential is measured.

We consider the recovery of the conductivity from boundary measurements when there are regions of high contrast so that linearization methods (the Born approximation) do not work. The analysis of current flow in regions with high conductivity, the direct problem, has been carried out in [54, 17]. This analysis motivates our approach to the high contrast inverse problem: we model the unknown conductivity in a special way, suggested by the analysis of the direct problem, and then estimate the parameters of the model conductivity by an output least-squares process.

1 The High Contrast Model

1.1 Description of the Model

There are many ways in which high contrast conductivity may arise in practice. We can have, for example, a uniform background conductivity with highly conducting or insulating inclusions of different shape. Since in many applications we do not know the shape of the inclusions, it is convenient to assume that the high contrast of the conductivity (σ) arises in a general way from a continuum model of the form

$$\sigma(\mathbf{x}) = \sigma_0 e^{-S(\mathbf{x})/\epsilon}. \tag{3.1.2}$$

Here σ_0 is a reference constant conductivity, $S(\mathbf{x})$ is a smooth function and ϵ is a small parameter. Variations of the function $S(\mathbf{x})$, the scaled logarithm of the conductivity, are amplified by the parameter ϵ, producing the high contrast of the conductivity. Media with discontinuous conductivities, like ones with inclusions of finite size, can then be viewed as particular cases of the generic model (3.1.2).

1.2 Review of the asymptotic theory

Although we presented the asymptotic results in chapter 2 in great detail, we include at this point, to make this chapter self-contained, a short review of the asymptotic resistor network theory. We consider transport in media with high contrast conductivity (3.1.2) and present the results in the context of homogenization [11, 45]. However, the conclusions reviewed in this section are equally valid for more general circumstances.

We consider the flow problem

$$\nabla \cdot (\sigma \nabla \phi) = 0 \tag{3.1.3}$$

in a periodic unit cell Ω, where ϕ is the electric potential and $\sigma(\mathbf{x})$ is the conductivity. The flow is driven by the condition

$$< \nabla \phi >= \mathbf{e} \tag{3.1.4}$$

where $< \cdot >$ stands for the normalized average over Ω and $\mathbf{e}$ is a unit vector. The mean potential gradient can be specified, for example, by prescribing uniform and different values of the potential at two opposite sides of the domain.

By using Ohm's law $\mathbf{j} = \sigma \nabla \phi$ where $\mathbf{j}$ is the electric current, we can also consider the dual problem

$$\begin{aligned} \nabla \times (\rho \mathbf{j}) &= 0 \\ \nabla \cdot \mathbf{j} &= 0 \\ < \mathbf{j} > &= \mathbf{e}, \end{aligned} \tag{3.1.5}$$

where $\rho(\mathbf{x}) = \sigma(\mathbf{x})^{-1}$ is the resistance.

It is shown in [54, 17] that when the conductivity has logarithmic high contrast in the form (3.1.2) there is strong channeling of the flow at the saddle points of σ. Moreover, by using the variational formulation of the effective conductivity and resistance [17]

$$\overline{\sigma} = \min_{<\nabla\phi>=\mathbf{e}} < \sigma\nabla\phi \cdot \nabla\phi > \tag{3.1.6}$$
$$\overline{\rho} = \frac{1}{\overline{\sigma}} = \min_{<\mathbf{j}>=\mathbf{e},\, \nabla\cdot\mathbf{j}=0} < \rho\mathbf{j} \cdot \mathbf{j} >,$$

it is shown that in the asymptotic limit of high contrast the leading order term in the effective parameters $\overline{\sigma}$ and $\overline{\rho}$ is obtained by considering the flow only in the neighborhoods of the saddle points of σ.

To explain this flow behavior in the vicinity of the saddles, let us assume that the conductivity has a single saddle point $\mathbf{x}_S \in \Omega$, which is oriented in the driving direction, say $\mathbf{e} = \mathbf{e}_1 = (1, 0)$. In a small neighborhood of $\mathbf{x}_S$, the conductivity has the form

$$\sigma(\mathbf{x}) \approx \sigma(\mathbf{x}_S) \exp[\frac{k(x - x_S)^2}{2\epsilon} - \frac{p(y - y_S)^2}{2\epsilon}], \tag{3.1.7}$$

where k and p are the curvatures of $S(\cdot)$ at the saddle point. In general, the saddle point can be oriented in any direction but equation (3.1.7) still holds if at $\mathbf{x}_S$ we introduce a local system of coordinates (x, y) such that direction x coincides with the direction of the saddle. We take as the small region around $\mathbf{x}_S$ the square $\mid x - x_S \mid \leq \delta, \mid y - y_S \mid \leq \delta$ where the parameter $\delta \to 0$ in such a way that $\frac{\delta}{\epsilon} \to \infty$ as $\epsilon \to 0$.

From (3.1.3), the local problem near the saddle point is

$$\begin{gathered} \nabla \cdot \{\sigma(\mathbf{x}_S) \exp[\frac{k(x - x_S)^2}{2\epsilon} - \frac{p(y - y_S)^2}{2\epsilon}]\nabla\phi\} = 0 \\ < \nabla\phi >= \mathbf{e}_1 \end{gathered} \tag{3.1.8}$$

which we solve by separation of variables. The potential $\phi(\mathbf{x})$ is

$$\phi(x, y) \approx \frac{1}{2}\mathrm{erf}(\sqrt{\frac{k}{2\epsilon}}(x - x_S)), \tag{3.1.9}$$

correct up to an additive constant which is set to zero here. The analytical basis for (3.1.9) is matched asymptotic expansions. The local analysis gives the leading term

(3.1.9) in the inner expansion valid near the saddle point. The outer expansion deals with the diffuse flow in the rest of the domain. The potential $\phi(\mathbf{x})$ therefore has the character of an inner layer in the direction of the saddle (the x direction in this case).

From (3.1.9) we compute the potential gradient

$$\nabla\phi(x,y) \approx \frac{1}{\sqrt{\frac{2\pi\epsilon}{k}}} e^{-\frac{k(x-x_S)^2}{2\epsilon}} \mathbf{e}_1 \tag{3.1.10}$$

and the current

$$\mathbf{j} = -\sigma\nabla\phi \approx -\frac{\sigma(\mathbf{x}_S)}{\sqrt{\frac{2\pi\epsilon}{k}}} e^{-\frac{p(y-y_S)^2}{2\epsilon}} \mathbf{e}_1. \tag{3.1.11}$$

We note from (3.1.10) and (3.1.11) that when the contrast of σ is high (ϵ is small) both the current and potential gradient are narrow Gaussians centered at $\mathbf{x}_S$ which means that there is strong flow channeling around the saddle point of the conductivity. The results (3.1.10) and (3.1.11) imply that the overall, or effective, conductivity and resistance (3.1.6) are (see [54, 17])

$$\overline{\sigma} \approx \sigma(\mathbf{x}_S)\sqrt{\frac{k}{p}} \quad \text{and} \quad \overline{\rho} \approx \frac{1}{\sigma(\mathbf{x}_S)}\sqrt{\frac{p}{k}}. \tag{3.1.12}$$

Thus, the flow through a medium with high contrast conductivity can be approximated by the flow through a resistor having resistance $\overline{\rho}$, given by (3.1.12).

In more general situations, where there are more saddle points of σ in the region that are oriented in different directions, the flow still concentrates at the saddles but it follows a more complicated pattern, which is a network of channels. Locally, around each saddle point of the conductivity, the flow is approximated by the current through resistors given by (3.1.12). These resistors are connected in a network that is identified as follows: the nodes of the network are the maxima of $\sigma(\mathbf{x})$ and the branches are paths connecting two adjacent maxima over a saddle point.

2 Inversion Algorithm

The asymptotic network theory described in §2 suggests that if we have flow channeling in the medium that we are trying to image, there is significant information in the data about the resistor network that describes the flow in the high contrast regions of the conductivity. Thus in the first step of the inversion algorithm we should attempt to identify the resistor network (channels of flow). The flow through this network is also the leading order term of the flow in the high contrast regions of σ. We can then use the conductivity estimate from the first stage of the inversion algorithm as a starting point for the second stage, in which we try to recover other features that were not captured by the network. In this step of the inversion we can linearize about the conductivity of the resistor network. Linearization works well because the main part of the flow through the high contrast regions of σ is already estimated, and small changes of the conductivity about it produce small changes in the potential gradients.

2.1 Identification of the Asymptotic Resistor Network

In order to identify the resistor network that describes the flow through the high contrast regions, we *model* the unknown conductivity σ by

$$\sigma(\mathbf{x}) \longrightarrow \sigma_b + \sum_{j=1}^{m} \chi_j(\mathbf{x}, \mathbf{s}_j) f_j(\mathbf{x}, \mathbf{s}_j). \tag{3.2.1}$$

Here σ_b is a uniform background in which we imbed the high contrast modules $f_j(\cdot)$. Each high contrast module is of the form $f_j(\cdot) \sim e^{\frac{S_j(\mathbf{x})}{\epsilon}}$ with support in the interior of Ω, and consists of a saddle point surrounded by two maxima and two minima. The vectors of parameters $\mathbf{s}_j$ describe the structure of the modules $f_j(\cdot)$ by specifying the position of the saddle points, their orientation, the curvatures at the saddle, the contrast, etc. The modules $f_j(\cdot)$ are localized with the smooth cutoff functions $\chi_j(\cdot)$.

Since conductivities defined by (3.2.1) are completely determined by the parameters $\mathbf{s}_j$, $j = 1, \ldots m$, we estimate them by minimizing the error between the solution with these parameters and the observed data. Thus, we estimate the $\mathbf{s}_j$, $j = 1, \ldots m$ by minimizing the mean-square error

$$E(\mathbf{s}_1, \ldots \mathbf{s}_m) = \sum_{i=1}^{M} \sum_{k=1}^{N} [\psi_k^{(i)} - \phi_k^{(i)}(\mathbf{s}_1, \ldots \mathbf{s}_m)]^2, \tag{3.2.2}$$

where the index of summation k runs through the data points on the boundary and i labels the pair of electrodes at which the current is injected into the domain.

The potential measured on the boundary is $\psi_k^{(i)}$, while $\phi_k^{(i)}(\cdot)$ is the potential on the boundary calculated by solving the partial differential equation (3.0.1) with the current best estimate of a conductivity of the form (3.2.1). This is an output least-squares estimation method, parametrized with high contrast conductivities of the form (3.2.1).

Introducing a model of the form (3.2.1) for the conductivity is a form of *regularization* [72, 59, 60, 56] for the output least squares problem (3.2.2). It is particularly well suited to high contrast problems, as we know from the analysis of the direct problem summarized in section 2.2.

To describe the minimization algorithm that we use, we assume for simplicity that we have only one high contrast module ($m = 1$) in (3.2.1). When the vector of parameters $\mathbf{s} \in \mathbb{R}^p$ changes by $\Delta\mathbf{s}$, the mean-square error (3.2.2) changes by

$$E(\mathbf{s}) + \Delta E \approx \sum_{i=1}^{M}\sum_{k=1}^{N}[\psi_k^{(i)} - \phi_k^{(i)}(\mathbf{s}) - \sum_{j=1}^{p}\frac{\partial\phi_k^{(i)}}{\partial s_j}\Delta s_j]^2, \tag{3.2.3}$$

where we use the fact that, when the change in $\mathbf{s}$ is small, we have

$$\phi_k^{(i)}(\mathbf{s} + \Delta\mathbf{s}) \approx \phi_k^{(i)}(\mathbf{s}) + \sum_{j=1}^{p}\frac{\partial\phi_k^{(i)}}{\partial s_j}\Delta s_j. \tag{3.2.4}$$

From (3.2.3) the change in the error is

$$\Delta E \approx \sum_{j=1}^{p}\sum_{l=1}^{p}A_{jl}\Delta s_j\Delta s_l - 2\sum_{j=1}^{p}b_j\Delta s_j. \tag{3.2.5}$$

Here we introduced the symmetric positive definite matrix

$$A_{jl} = \sum_{i=1}^{M}\sum_{k=1}^{N}\frac{\partial\phi_k^{(i)}}{\partial s_j}\frac{\partial\phi_k^{(i)}}{\partial s_l} \tag{3.2.6}$$

and the vector

$$b_j = \sum_{i=1}^{M}\sum_{k=1}^{N}[\psi_k^{(i)} - \phi_k^{(i)}(\mathbf{s})]\frac{\partial\phi_k^{(i)}}{\partial s_j}, \tag{3.2.7}$$

whose components measure the current data misfit weighted by the sensitivity of the potential to changes in s_j. The decrease in the error ΔE is maximized when the parameters $\Delta\mathbf{s}$ satisfy the linear equations

$$A\Delta\mathbf{s} = \mathbf{b} \tag{3.2.8}$$

and then the change in the mean-square error is

$$\Delta E \approx -\Delta \mathbf{s}^T A \Delta \mathbf{s} \leq 0. \tag{3.2.9}$$

This Gauss-Newton algorithm [34, 26, 32], given by (3.2.6) - (3.2.8), does not work well here because the matrix A, defined by (3.2.6) is ill-conditioned. Some of the components of the parameter vector $\mathbf{s}$ change faster than others. For example, when the contrast is high and the flow concentration at the saddle point is strong, the position of the saddle point is recovered after a few iterations while the contrast converges slowly. We avoid this difficulty by updating the vector of parameters $\mathbf{s}$ one component at a time, instead of all at once. This approach has, in addition, the advantage of allowing us to terminate the updating of parameters that have converged before the end of the overall iteration process. The change in the j^{th} component of $\mathbf{s}$ that maximizes the decrease in the error is easily found to be

$$\Delta s_j = \frac{\sum_{i=1}^{M}\sum_{k=1}^{N}[\psi_k^{(i)} - \phi_k^{(i)}(\mathbf{s})]\frac{\partial \phi_k^{(i)}}{\partial s_j}}{\sum_{i=1}^{M}\sum_{k=1}^{N}(\frac{\partial \phi_k^{(i)}}{\partial s_j})^2} = \frac{b_j}{A_{jj}} \tag{3.2.10}$$

and then

$$\Delta E \approx -(\Delta s_j)^2 \sum_{i=1}^{M}\sum_{k=1}^{N}(\frac{\partial \phi_k^{(i)}}{\partial s_j})^2 = -A_{jj}(\Delta s_j)^2 \leq 0. \tag{3.2.11}$$

The change in the parameters $\mathbf{s}$ depends both on the error at the boundary and on the sensitivity coefficients $\frac{\partial \phi_k^{(i)}}{\partial s_j}$. Thus, at each step of the iteration we must solve the elliptic problems

$$\begin{aligned} \nabla \cdot (\sigma \nabla \phi) &= 0 \\ \sigma \frac{\partial \phi}{\partial n} &= f \text{ on } \delta\Omega \\ \phi(\mathbf{0}, \mathbf{s}) &= 0 \end{aligned} \tag{3.2.12}$$

and

$$\nabla \cdot (\sigma \nabla \frac{\partial \phi}{\partial s_i}) = -\nabla \cdot (\frac{\partial \sigma}{\partial s_i} \nabla \phi)$$

$$\begin{aligned} \sigma \frac{\partial}{\partial n}(\frac{\partial \phi}{\partial s_i}) &= 0 \text{ on } \delta\Omega \\ \frac{\partial \phi}{\partial s_i}(\mathbf{0}, \mathbf{s}) &= 0 \text{ for } i = 1, \ldots p. \end{aligned} \tag{3.2.13}$$

However, since small changes in the components of $\mathbf{s}$ lead to an updated potential of the form (3.2.4), we need not solve (3.2.12) for each iteration but only once every p iterations.

In the Gauss-Newton method used here we approximate the Hessian of the mean square error (3.2.1) by the first derivatives of the estimated potential (3.2.4). We omit the second derivatives which are difficult to calculate. The success of the Gauss-Newton method depends on the negligibility of second derivatives [26, 32, 34]. In order to insure that second derivatives in the Hessian are negligible, we scale the update in the parameters (3.2.10) by a factor $\lambda_c > 0$, as is usually done in damped Gauss-Newton methods [26, 34]. These methods are globally convergent for many nonlinear least-squares problems, including large residual problems [26, 34]. In our computations we choose the scaling parameter λ_c so that the change in s_j is smaller than 15%.

2.2 Identification of Features of the Conductivity that are Neglected by the Asymptotic Theory

The resistor network identified by the algorithm described in section 3.2.1 is in general only a rough estimate of the conductivity $\sigma(\mathbf{x})$. In order to improve its resolution we must also identify low contrast features of $\sigma(\mathbf{x})$ that are not captured by the asymptotic resistor network theory. This is done by linearizing about the network conductivity estimated by the algorithm described in the previous section. In this section we define the linearized problem and explain why it works at this stage of the inversion algorithm.

For the reference medium with conductivity $\sigma_r(\mathbf{x})$ of form (3.2.1) we have

$$\nabla \cdot [\sigma_r(\mathbf{x}) \nabla \phi_r(\mathbf{x})] = 0 \quad \text{in} \quad \Omega \tag{3.2.14}$$

$$\sigma_r \frac{\partial \phi_r}{\partial n} = I \quad \text{on} \quad \partial\Omega,$$

where $\phi_r(\mathbf{x})$ is the reference potential. In the linearized problem

$$\sigma(\mathbf{x}) = \sigma_r(\mathbf{x}) + \delta\sigma(\mathbf{x}), \quad \text{where} \ \mid \delta\sigma(\mathbf{x}) \mid \ll \mid \sigma_r(\mathbf{x}) \mid . \tag{3.2.15}$$

Problem (3.0.1) can then be written as

$$\begin{aligned} \nabla \cdot [\sigma_r(\mathbf{x})\nabla\psi(\mathbf{x})] = -\nabla \cdot [\delta\sigma(\mathbf{x})\nabla\phi(\mathbf{x})] \quad \text{in} \ \ \Omega \\ (\sigma + \delta\sigma)\frac{\partial \phi}{\partial n} = I \quad \text{on} \ \partial\Omega, \end{aligned} \tag{3.2.16}$$

where $\psi(\mathbf{x}) = \phi(\mathbf{x}) - \phi_r(\mathbf{x})$. The 'scattered' potential gradient $\nabla\psi(\mathbf{x})$ that is due to the change $\delta\sigma(\mathbf{x})$ of the reference conductivity is assumed to be much smaller than the reference potential gradient $\nabla\phi_r(\mathbf{x})$, so we linearize (3.2.16)

$$\nabla \cdot [\sigma_r(\mathbf{x})\nabla\psi(\mathbf{x})] \approx -\nabla \cdot [\delta\sigma(\mathbf{x})\nabla\phi_r(\mathbf{x})] \quad \text{in} \ \ \Omega. \tag{3.2.17}$$

Equation (3.2.17) is linear in $\delta\sigma(\mathbf{x})$. Linearization is justified in the second stage of our inversion algorithm because, as we explained in section 3.1.2 , the resistor network given by $\sigma_r(\mathbf{x})$ determines the main part of the flow in the high contrast regions of the medium. Small changes of the reference conductivity can only produce small changes in the potential gradient, so linearization (3.2.17) can be done.

Inversion of the linearized problem has been the topic of numerous studies and an extensive literature on recovery algorithms is available [1, 9, 25, 43, 61, 65, 67, 73]. In our computations we used an inversion algorithm based on adjoint fields [64] that requires less computation than the usual algorithms that are based on Green's functions.

3 Numerical Results

3.1 The PLTMG solver

We review a few facts about the software package PLTMG [7] that we use for solving the elliptic problems (3.2.12) and (3.2.13) during the iterative process described in

§3. PLTMG is an elliptic partial differential equation solver in two dimensions. It uses an adaptive multigrid approach and a finite element discretization based on C^0 piecewise linear triangular elements.

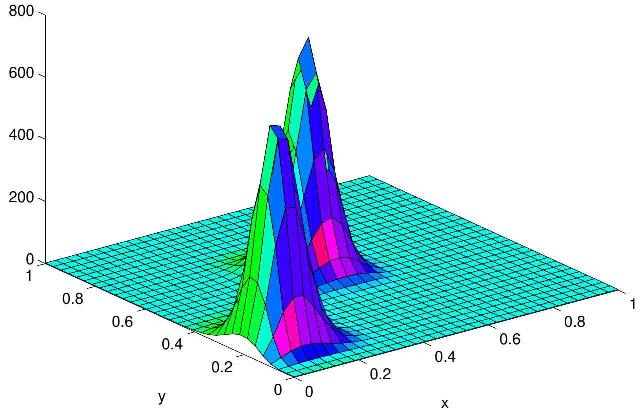

Figure 3.3.2: Model conductivity (Contrast = 369)

We tested extensively the performance of PLTMG for problems of form (3.2.12) with high contrast conductivity in [18]. We found that for contrasts no higher than $O(10^2)$, the numerical solution given by PLTMG is accurate, within a few percent. When the contrast is higher, the solution produced by PLTMG can be quite inaccurate in the vicinity of the saddle points of σ where strong flow channeling occurs, but overall remains satisfactory away from the channels. Since in our computations we use only the boundary values of the potential and we assume that all the channels are in the interior of Ω, we may use PLTMG for computing the potential $\phi(\mathbf{x}, \mathbf{s})$ and the sensitivity coefficients $\frac{\partial \phi}{\partial s_i}(\mathbf{x}, \mathbf{s})$ for $i = 1, \ldots p$, on the boundary.

3.2 One Channel Model

In this section we present numerical results obtained with the inversion algorithm described in §3 for conductivities that have only one saddle point in the domain. An

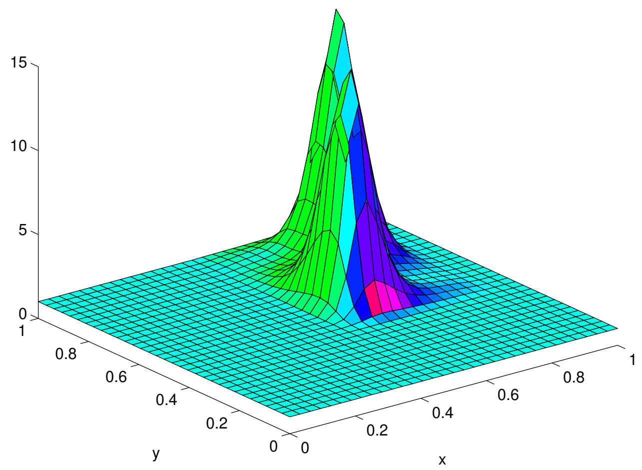

Figure 3.3.3: Initial conductivity guess (Contrast = 14.7)

example of such a conductivity is

$$\sigma(\mathbf{x}) = \sigma_b + \chi(\mathbf{x}, \mathbf{s}) f(\mathbf{x}, \mathbf{s}), \tag{3.3.1}$$

where σ_b is a uniform background, $f(\cdot)$ is a high contrast module that has a saddle point surrounded by two maxima and two minima and $\chi(\cdot)$ is a cutoff function that localizes $f(\cdot)$. We model the high contrast module by

$$f(\mathbf{x}, \mathbf{s}) = \sigma_0 exp\{\frac{1}{\epsilon} \sin[\alpha((x-x_s)\cos\theta + (y-y_s)\sin\theta)] \sin[\beta((y-y_s)\cos\theta - (x-x_s)\sin\theta)]\}, \tag{3.3.2}$$

where (x_s, y_s) is the location of the saddle point of the conductivity, θ is the orientation of the saddle and ϵ determines the contrast. The function $f(\cdot)$ in (3.3.2) is periodic with period determined by α and β, which also determine the curvatures at the saddle. The constant σ_0 controls the height of the saddle. Thus, the high contrast conductivity module is completely described by the eight-component vector

$$\mathbf{s} = (\sigma_b, \sigma_0, \alpha, \beta, x_s, y_s, \theta, \epsilon). \tag{3.3.3}$$

The high contrast module $f(\cdot)$ is tapered with the C^1 cutoff function

$$\chi(\mathbf{x}, \mathbf{s}) = g((x - x_s)\cos\theta + (y - y_s), \alpha) g(-(x - x_s)\sin\theta + (y - y_s)\cos\theta), \beta), \tag{3.3.4}$$

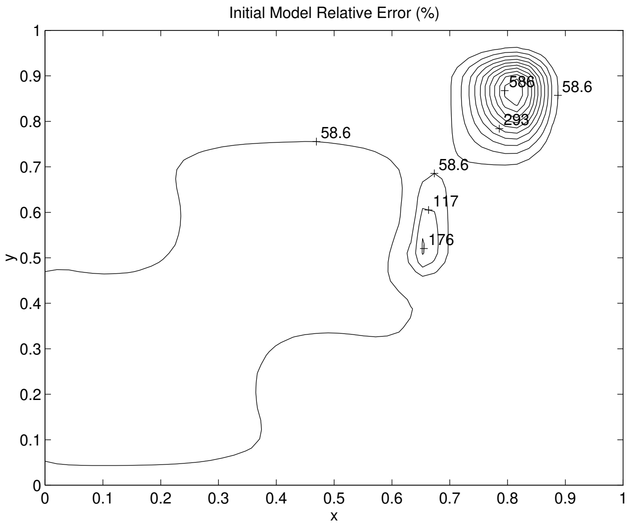

Figure 3.3.4: L_∞ initial relative error in the conductivity

where

$$g(\xi,\gamma) = \begin{cases} \sin^3[\frac{\pi}{2}(\xi + \frac{\pi}{\gamma})/d] & \text{for} \quad -\frac{\pi}{\gamma} \leq \xi \leq -\frac{\pi}{\gamma} + d \\ -\sin^3[\frac{\pi}{2}(\xi - \frac{\pi}{\gamma})/d] & \quad \frac{\pi}{\gamma} - d \leq \xi \leq \frac{\pi}{\gamma} \\ 1 & \quad -\frac{\pi}{\gamma} + d \leq \frac{\pi}{\gamma} - d \\ 0 & \quad \mid \xi \mid \geq \frac{\pi}{\gamma}. \end{cases} \tag{3.3.5}$$

The parameter d in (3.3.5) controls the sharpness of the cutoff and it is kept constant throughout the numerical experiments.

The data that we use in the numerical experiments are generated numerically with a synthetic model of the form (3.3.1) and PLTMG. An example of a conductivity used to generate data is shown in Fig. 3.3.2. In a uniform background, $\sigma_b = 2$, we have embedded a high contrast module $(\max(\sigma)/\min(\sigma) = 369)$ that has a saddle at $(x_s, y_s) = (0.3, 0.4)$ which is oriented at an angle $\pi/4$ from the axes.

As a starting point in the iterative process of reconstructing the model σ shown in Fig. 3.3.2, we consider the conductivity shown in Fig. 3.3.3. Even though the initial guess is of the same form (3.3.1) as the model, the set of parameters $\{\mathbf{s}\}$ describing it is very different. The background conductivity is $\sigma_b^{init} = 1$, the saddle is situated at $(x_s, y_s)^{init} = (0.7, 0.7)$ and the contrast is 14.7. The initial relative error in the

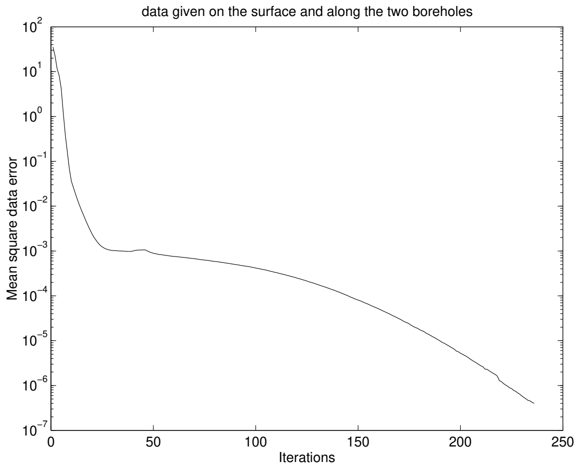

Figure 3.3.5: Evolution of the mean square data error

conductivity (see Fig. 3.3.4) is very high around the initial guess of the position of the saddle ($\sim$ 600%) and about 60% elsewhere in the domain.

In the reconstruction process, the data consists of the value of the potential at points placed a distance $h = 1/32$ apart along the sides ($x = 0$ and $x = 1$) and the surface boundary ($y = 1$). Current is injected with two different pairs of electrodes located at (0,0.5), (1,0.5) and (0,0.3), (0.5,1), respectively.

The evolution of the mean-square data error during the iteration process is shown in Fig. 3.3.5. The algorithm reduces this error monotonically. However, it does not guarantee reduction of the error in the conductivity and as shown in Fig. 3.3.6. At some stage of the iteration process the error in the model actually increases. This behavior is due to the strong nonlinearity of the problem and is more subdued in experiments with contrast of order $O(10)$. After 250 iterations, the relative error in the conductivity in the L_2 norm is reduced by two orders of magnitude. The final relative error in the model in the L_∞ norm (see Fig. 3.3.7) is only a few percent so the model conductivity is recovered quite well.

During the reconstruction process, some of the components of the vector of parameters $\mathbf{s}$ describing the model conductivity are recovered more quickly than others. For example, the position of the saddle point is expected to be easily recovered in

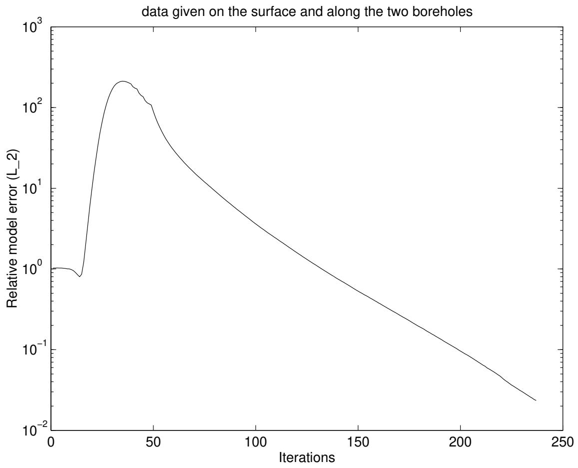

Figure 3.3.6: Evolution of the L_2 relative error in the conductivity

experiments with high contrast. For low contrasts flow channeling is weak so the position of the saddle is harder to recover. In Fig. 3.3.8 and 3.3.9, we show the evolution of the relative error in three parameters (ϵ, σ_b and x_s) obtained from two numerical experiments that assume contrasts 10^4 and 14, respectively. As expected, when the contrast is high the position of the saddle and the uniform background are recovered more quickly than the parameter ϵ that controls the contrast. However, when the contrast is lowered to 14 the position of the saddle is the last parameter to be recovered. The numerical experiment for reconstructing the model conductivity shown in Fig. 3.3.2 was repeated with data to which 5% noise has been added. The noise is simulated with independent, identically distributed Gaussian random variables. The starting point in the iteration is as before (see Fig. 3.3.3). From Fig. 3.3.10 we see that the mean-square error decreases to about 10^{-2} in 50 iterations and remains unchanged after that. The relative error in the model in the L_∞ norm, shown in Fig. 3.3.11, tells us that, even with a very noisy data, the algorithm recovers very well the background conductivity, the position and orientation of the channel and the support of the high contrast region. The error is high ($\sim 30\%$) only around the maxima of the conductivity where the potential gradient is nearly zero and so the inverse problem is ill-posed in this region. The quality of the results improves when the noise level is

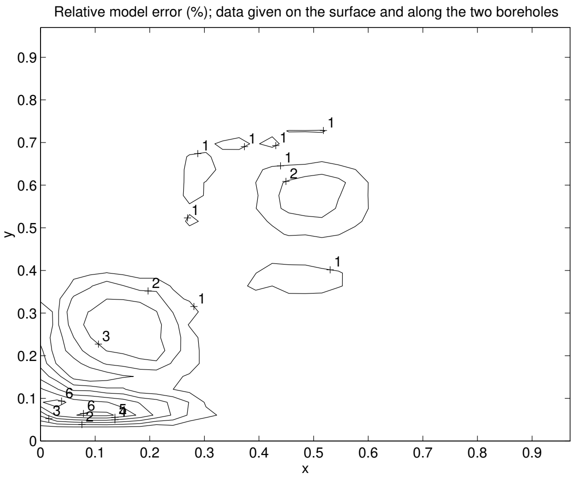

Figure 3.3.7: Relative model error (%)

reduced. For example, with 1% noise the relative model error is smaller than 10%.

Since data are given only at a discrete number of points on the boundary, the resolution of the estimates is limited. To illustrate this point we present the results of a numerical experiment with model conductivity in a tight, high contrast configuration. If the domain is discretized with a uniform mesh corresponding to the number of data points on the boundary, the distance between the two maxima of the high contrast conductivity is just six grid spacings. The contrast is 300 and the iteration starts as before with an initial guess that is far from the model parameters. The relative error in the conductivity at the end of the iteration process is shown in Fig. 3.3.12. Thus, the algorithm is successful in recovering the uniform background, the position and orientation of the channel and the support of the high contrast region, but it does not give a very accurate conductivity around the position of the maxima.

3.3 Nonuniform background

The numerical experiments presented so far show that the inversion algorithm described in §3.1 is successful in imaging the conductivity when the model σ belongs to the same class of functions (4.0.3) within which we are searching. We now consider

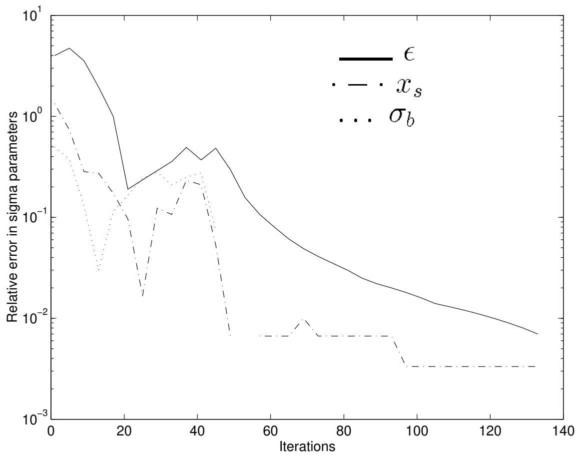

Figure 3.3.8: Convergence of high contrast module parameters. Contrast of $\sigma = 10^4$

a more realistic experiment in which we try to recover the model conductivity shown in Fig. 3.3.13, which consists of a high contrast module embedded in a variable background (see Fig. 3.3.14). The local variation in magnitude of the conductivity around the high contrast region is about 100, but only about 7 elsewhere in the domain. The data (ϕ at the boundary) are given at 32 uniformly distributed points along each side of the boundary and is generated numerically with the model conductivity shown in Fig. 3.3.13.

In the first step of the inversion process we looked for a conductivity of the form (4.0.3) that is most consistent with the data. In the computations we consider data generated with only two pairs of electrodes at $(0., 0.5)$, $(1., 0.5)$ and $(0.5, 0.)$, $(0.5, 1.)$ respectively. The result is shown in Fig. 3.3.15 and the error in the conductivity is presented in Fig. 3.3.16 and 3.3.17. Thus, the inversion algorithm recovered the position and orientation of the channel as well as the support of the high contrast region. The error is large around the two peaks of the conductivity and for the background in which we embedded the high contrast module. We can view the results of this first step as a low resolution image of the conductivity, that gives only features that control the leading order term of the flow. Other details, like the variable background conductivity, are completely ignored.

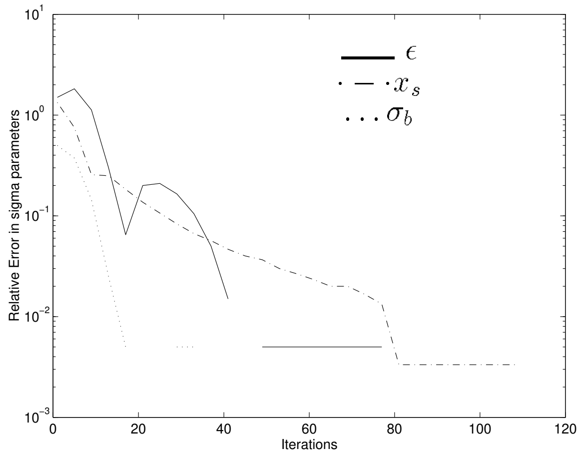

Figure 3.3.9: Convergence of high contrast module parameters. Contrast of $\sigma = 14$

In the second step of the inversion process, we improve the quality of the image by linearizing about the conductivity given by the first step. In the numerical computations we use the same data points as before and many more pairs of electrodes for current injection. It is natural that in the first step of the inversion it is sufficient to consider data from only a few (two) current source-sink pairs while in the next step (the linearization process) we need data from many more current source-sink pairs. This is because the first inversion step only looks for the channel of strong flow and ignores all other details of the conductivity. Thus, in order to get the single resistor in the asymptotic network, along with its position and orientation, we only need two current source-sink pairs into the domain, chosen so that flow will cross it.

The relative error of the final conductivity (Fig. 3.3.18) shows clearly that the quality of the image has improved, by almost 150% in the background. It remained constant around the peaks in the high contrast region of σ. The parameters identified in the first step of the inversion did not deteriorate in the linearization step.

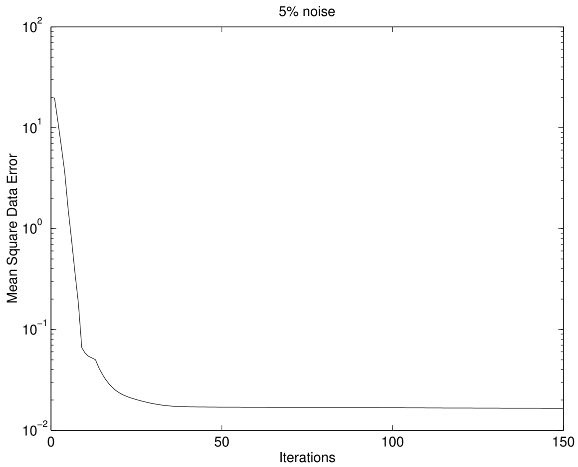

Figure 3.3.10: Evolution of mean square data error (5% noise)

3.4 Multiple channels

All the numerical examples presented so far have a single channel of flow concentration in the medium. In general, there can be an arbitrary number of channels that is not known. Identification of the resistor network in these cases can be done with the algorithm described in advance (§3.1), where the model conductivity will have many high contrast modules. Another approach is to identify a single channel at a time. We use this approach in imaging the conductivity of media with two and three channels of flow. If the channels are well separated, the algorithm works well. The channels are found sequentially, one by one, starting with the one closest to the boundary and ending with the ones in the interior of the flow domain.

The amount of data needed for inversion is larger than for media with a single channel of flow concentration, where data from two source-sink pairs are sufficient. For instance, in a numerical experiment with two channels we can recover the resistor network with six source-sink pairs. The error in the boundary data is shown with the dotted line in Fig. 3.3.19. The full line represents the error in an experiment with the same conductivity minus the interior channel and the same amount of data. We see that the error for the experiment with a single channel drops to 10^{-5}, while the

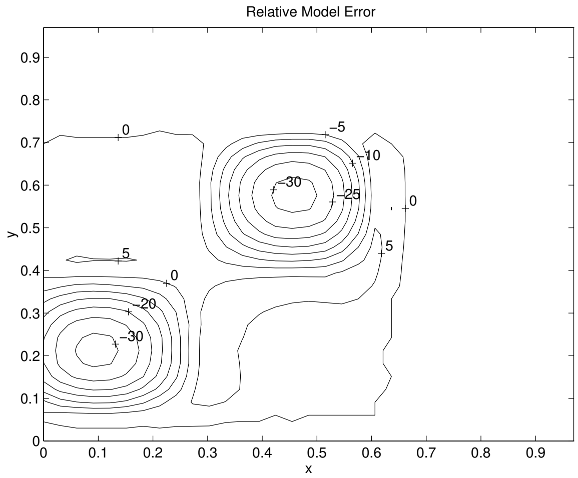

Figure 3.3.11: L_∞ conductivity error (5% noise)

error in the experiment with two channels has a more complex behavior. Initially, it decreases but then it stabilizes to a plateau at about 10^{-1}. This indicates that the algorithm has found the first channel and it cannot make any further reduction to the error unless a second high contrast module is introduced. The insertion of the second module is identified by the slight peak observed in the error around iteration 25. After this introduction the error drops rapidly and then stabilizes at about 10^{-3}, which indicates that the second channel has been identified. The error is worse than for the one channel experiment but it can be reduced by using more data.

The numerical experiments of this section show that when the medium consists of well separated channels of flow concentration, they can be identified one by one in a manner very similar to the method of matching pursuit [58]. However, when the channels are close together the algorithm breaks down because it tries to fit a high contrast module in between the channels. Such cases require special attention and will be considered in future research.

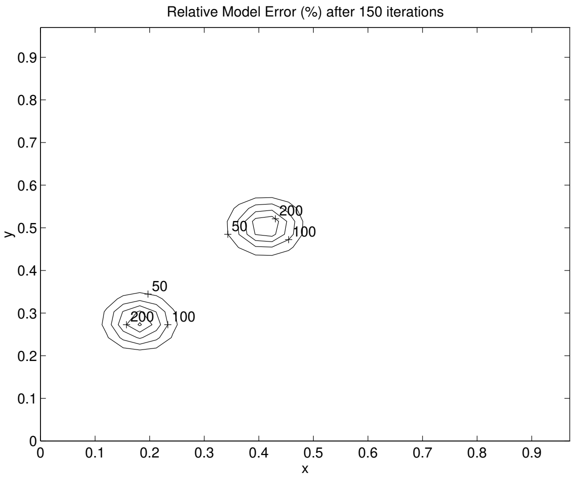

Figure 3.3.12: Tight high contrast configuration

4 Analysis of the boundary data

In this section we explain why the inversion method of §3 is successful in finding the channels of flow inside the medium. We do this by identifying features in the boundary data that have channel information. We assume that the medium has a single channel and a conductivity that belongs to the class described by (4.0.3). The channel is oriented in the vertical direction and is located at $(0.7, 0.6)$ (see Fig. 3.3.20). The asymptotic theory (see §2.2) shows that the flow is concentrated around the channel and is diffuse elsewhere in the flow regime. Thus, when the boundary excitation is such that flow must pass through the channel, the potential gradient near it is a Gaussian centered at the saddle point and oriented in the vertical direction. The flow concentration in the interior of the medium is visible at those parts of the boundary that are relatively close to the channel.

For a current source located at $(0.5, 0.)$ and a sink at $(0.5, 1.)$, we plot in Fig. 3.3.21 the vertical potential gradient at the left and right boundaries of Ω. At the right boundary, which is closer to the saddle point, there is a maximum of the vertical potential gradient $(\nabla\phi \cdot \mathbf{e}_2)$ at $y = 0.6$. However, at the left boundary, which is further away from the channel, flow concentration is not visible. When we drive the flow

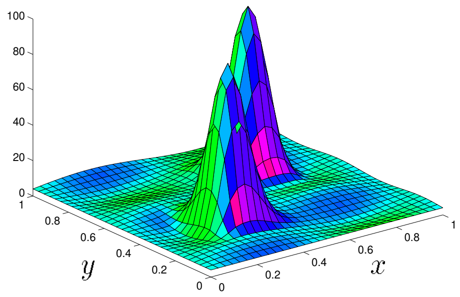

Figure 3.3.13: Model conductivity

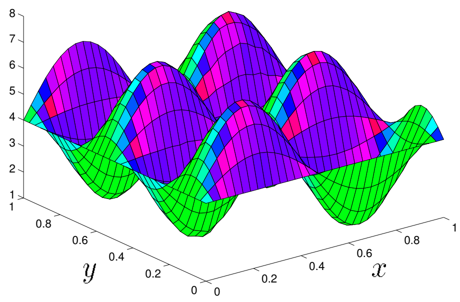

Figure 3.3.14: Background for the high contrast module

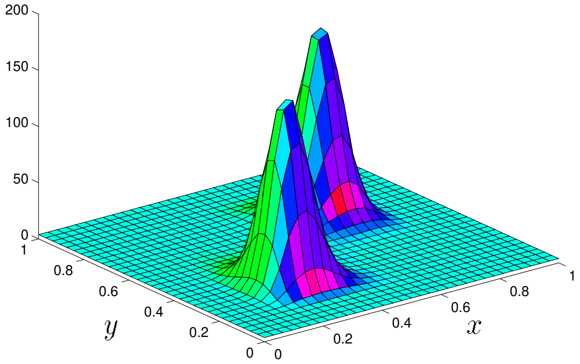

Figure 3.3.15: Conductivity after the first step of inversion

along the horizontal direction (source and sink are located at $(0., 0.5)$ and $(1., 0.5)$, respectively), the channel rejects the flow. Thus, the horizontal potential gradient has a minimum near the saddle point, which can be seen at the top boundary around $x = 0.7$ (see Fig 3.3.22). However, the minimum of $\nabla\phi \cdot \mathbf{e}_1$ cannot be observed at the bottom boundary, which is too far away from the channel. Thus, we can locate the vertical channel at $\mathbf{x}_S = (0.7, 0.6)$ very easily by just inspecting the boundary data.

The picture is more complicated when the high contrast module is embedded in a variable background because there are also regions of weak flow concentration in Ω that are felt at the boundary. For example, consider a medium with conductivity

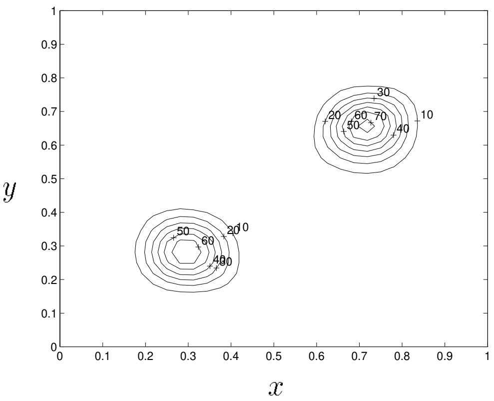

Figure 3.3.16: Absolute error in σ after the first step of the inversion

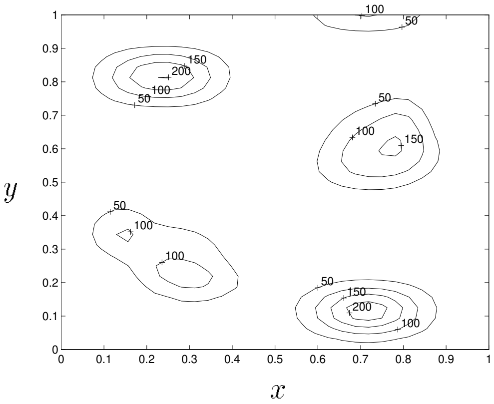

Figure 3.3.17: Relative error (%) in σ after the first step of the inversion

shown in Fig. 3.3.23. For a flow driven vertically with a current source and sink located at $(0.5, 0.)$ and $(0.5, 1.)$, respectively, the vertical potential gradient $(\nabla\phi \cdot \mathbf{e}_2)$ at the right and left boundaries is shown in Fig. 3.3.24. At the right boundary, we observe three maxima of the vertical potential gradient: one is centered at the saddle point $(y = 0.6)$ and the others (due to the minima of σ at $(0.75, 0.12)$ and $(0.83, 0.85)$) are centered at $y = 0.12$ and $y = 0.85$, respectively. At the left boundary, which is far from the saddle point, the channel is invisible but we observe two maxima of $\nabla\phi \cdot \mathbf{e}_2$. These maxima are due to the minima of the conductivity located at $(0.15, 0.31)$ and $(0.15, 0.75)$, respectively. When the sources are moved to $(0., 0.5)$ and $(1., 0.5)$, so that the flow has a horizontal direction, the channel at $\mathbf{x}_S = (0.7, 0.6)$ rejects the flow. In Fig. 3.3.25 we show the horizontal potential gradient $(\nabla\phi \cdot \mathbf{e}_1)$ at the top and bottom boundaries. The top boundary is closer to the channel and the minimum of $\nabla\phi \cdot \mathbf{e}_1$ at $x = 0.7$ is evident. However, although the channel is not seen at the bottom boundary, we nevertheless observe the maxima of the horizontal potential gradient that are due to the minima of σ located at $(0.15, 0.31)$ and $(0.75, 0.15)$.

In general, the conductivity of the unknown medium has a complicated structure and finding its main features in the interior of Ω by inspection of the boundary data is nearly impossible. Regions of weak flow concentration could give misleading information and channels can be hidden from the boundary. Consequently, the heuristic

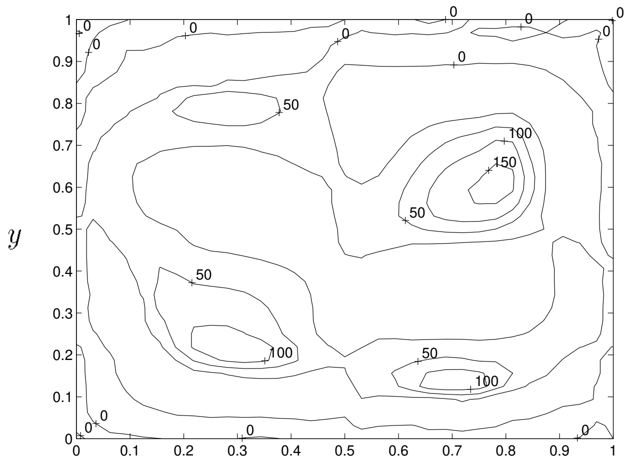

Figure 3.3.18: Relative error (%) in final σ

method for identifying channels in the medium described here is, in general, inefficient and inaccurate for complex situations. The simple examples presented here give, however, a physical explanation for the success of the inversion algorithm of §4 in localizing the channels in the medium.

5 Summary

We have introduced an inversion algorithm for tomographic imaging of media with large variations in the conductivity. The algorithm is based on the results of an asymptotic analysis of the forward problem in media with high contrast. This analysis shows that when the contrast of the conductivity is high, the flow can be roughly approximated by that of a resistor network. The network accounts for the main part of the flow and neglects the low contrast features of the conductivity. We introduce a new parametrization of the conductivity based on the resistor network theory and use an output least-squares approach for identifying the network. This parametrization acts as a regularization for the inverse problem. The conductivity estimated in this first stage of the algorithm is used as a reference conductivity in a second stage, where we identify low contrast features that are not captured by the network.

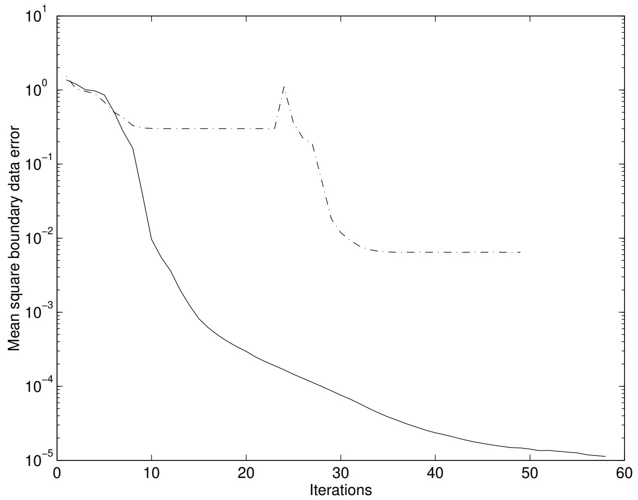

Figure 3.3.19: Output least-squares error as a function of the number of iterations. The solid lines is for conductivity function with one high contrast region. The dashed line is for a conductivity with two high contrast regions.

We have assessed the performance of the algorithm with several numerical experiments and have shown that it is stable and successful in imaging high contrast conductivities in many situations. At present, the inversion algorithm uses high contrast modules that are somewhat rigid (see (3.3.1)- (3.3.5)), in the sense that they require the peaks of the conductivity surrounding the channel to have the same height. We are currently exploring less rigid models in order to eliminate this deficiency. Media with multiple channels of flow need to be explored further.

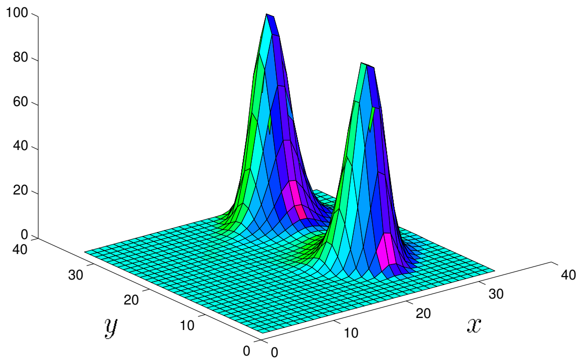

Figure 3.3.20: Conductivity with a vertical channel and uniform background

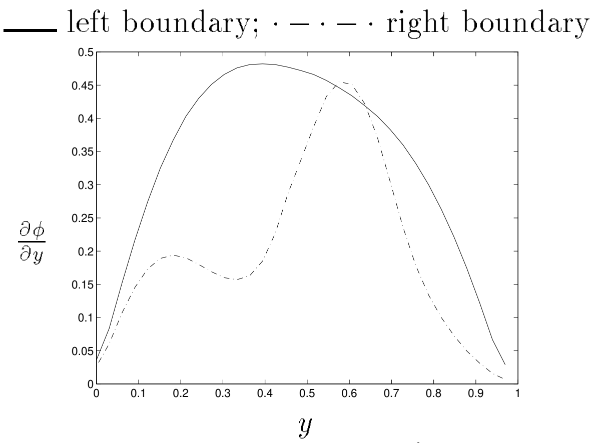

Figure 3.3.21: Vertical potential gradient at the left and right boundaries of Ω

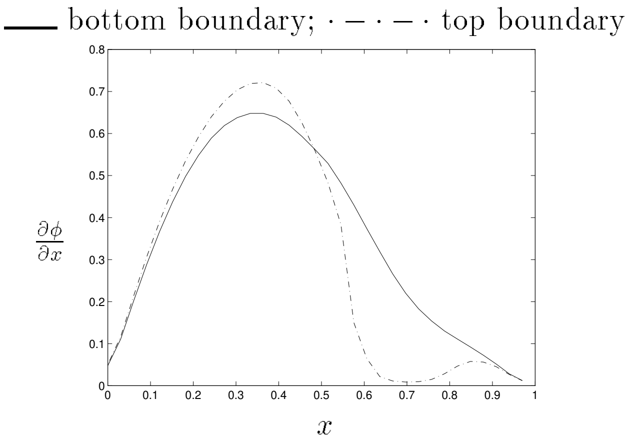

Figure 3.3.22: Horizontal potential gradient at the top and bottom boundaries of Ω

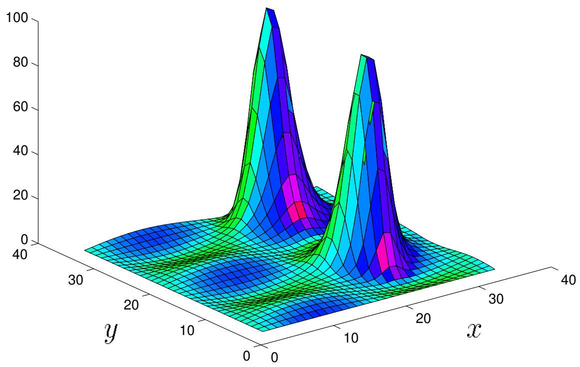

Figure 3.3.23: Conductivity with a vertical channel and variable background

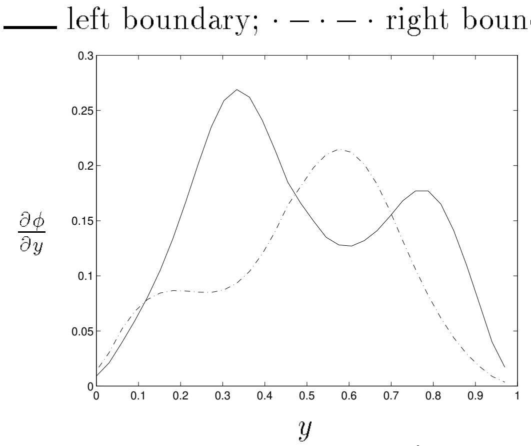

Figure 3.3.24: Vertical potential gradient at the left and right boundaries of Ω

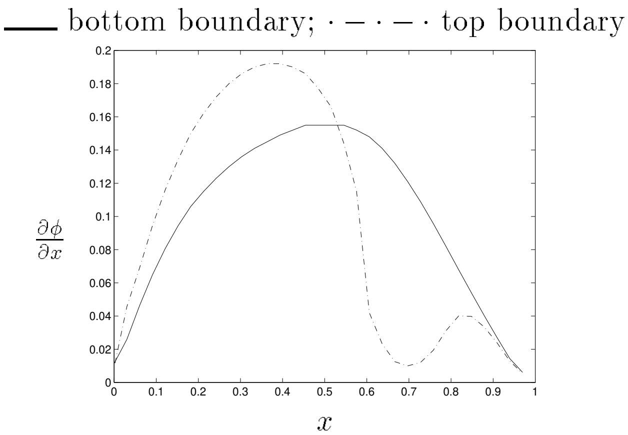

Figure 3.3.25: Horizontal potential gradient at the top and bottom boundaries of Ω

Chapter 4

Hybrid numerical method

In this chapter we present a hybrid numerical method for solving isotropic steady state problems in media with high contrast properties. The method combines the asymptotic resistor network theory, introduced in chapter 2, with the use of standard numerical methods, so we call it hybrid. For flow problems in media with strong variability in their properties, it is known that standard numerical methods encounter difficulties and are neither accurate nor efficient. The main difficulty encountered by standard methods arises because of very fine numerical meshes needed for capturing the correct flow behavior in the high contrast media. Thus, one has very large matrices that must be inverted. Because of the high contrast, the matrices are ill conditioned and thus iterative methods used in the inversion have very poor convergence rates. In this chapter we show that the hybrid method overcomes the difficulties listed above and that it is both efficient and accurate. We consider throughout the isotropic steady flow problem

$$-\nabla \cdot [\sigma(x,y)\nabla\phi(x,y)] = f(x,y) \tag{4.0.1}$$

defined in a unit square domain Ω (see Fig. 4.0.1), where σ is the conductivity, $\phi(x,y)$ is the electric potential and $f(x,y)$ is the source term. We choose a simple domain in order to simplify the exposition of the hybrid method but the methodology presented in this chapter applies to regions Ω of any shape.

The current is obtained from Ohm's law $\mathbf{j} = -\sigma\nabla\phi$ and the flow can be driven by either the forcing term $f(x,y)$ or by some inhomogeneous boundary conditions.

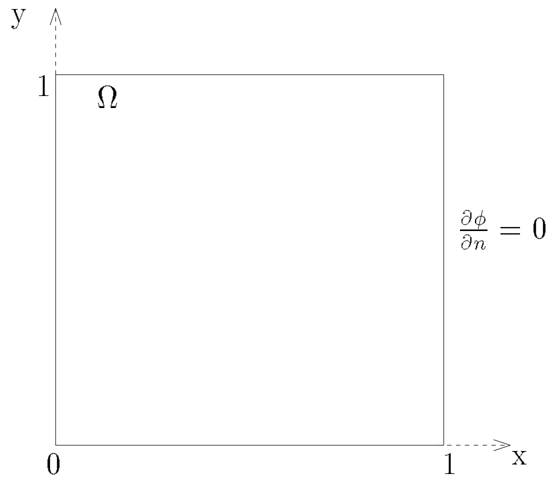

Figure 4.0.1: Computational domain

In order to fix ideas we assume that the flow is confined in Ω and impose the no-flux boundary conditions

$$\frac{\partial \phi}{\partial n}|_{\partial\Omega} = 0, \tag{4.0.2}$$

where $\mathbf{n}$ is the unit normal at the boundary, pointing outwards. The source term $f(x, y)$ is prescribed so that the flux injected equals the one taken out. For example, for a point source at $\mathbf{x}_1$ and sink at $\mathbf{x}_2$ we take

$$f(x, y) = \delta(\mathbf{x} - \mathbf{x}_1) - \delta(\mathbf{x} - \mathbf{x}_2). \tag{4.0.3}$$

In the numerical computations we use an approximation of the driving force (4.0.3) where the delta functions are approximated by narrow Gaussians centered at $\mathbf{x}_1$ and $\mathbf{x}_2$. Problem (4.0.1)-(4.0.3) with $\sigma(\mathbf{x}) > 0$ has a unique solution $\phi(x, y)$ up to an additive constant.

We showed in chapter 2 that for a high contrast conductivity of the form $\sigma(\mathbf{x}) = \sigma_0 e^{-\frac{S(\mathbf{x})}{\epsilon^2}}$ there is strong flow channeling at saddle points of $\sigma(x, y)$. Moreover, in a small neighborhood of a saddle point $\mathbf{x}_S$ where $\sigma(\mathbf{x}) \approx \sigma(\mathbf{x}_S) e^{\frac{k(x-x_S)^2}{2\epsilon^2} - \frac{p(y-y_S)^2}{2\epsilon^2}}$, the electric potential is given by

$$\phi(\mathbf{x}) \approx -C \mathrm{erf}[\sqrt{\frac{k}{2\epsilon^2}}(x - x_s)], \tag{4.0.4}$$

where k and p are the curvatures at the saddle and C is the flux through the saddle. The potential gradient is

$$\nabla\phi \approx -\frac{2C}{\sqrt{\frac{2\pi}{k}}\epsilon} e^{-\frac{k(x-x_S)^2}{2\epsilon^2}} \mathbf{e}_1, \tag{4.0.5}$$

and the current is given by

$$\mathbf{j} \approx \sigma(\mathbf{x}_S)\frac{C}{\sqrt{\frac{2\pi}{k}}} e^{-\frac{p(y-y_S)^2}{2\epsilon^2}} \mathbf{e}_1. \tag{4.0.6}$$

The flow through the saddle was shown to be well approximated by the flow through a resistor given by

$$\overline{R} \approx \frac{1}{\sigma(\mathbf{x}_S)}\sqrt{\frac{p}{k}}. \tag{4.0.7}$$

The analytical basis for (4.0.4)-(4.0.7) is the method of matched asymptotic expansions and the local analysis in a vicinity of the saddle point $\mathbf{x}_S$ gives the leading term in the inner expansion of the potential. The outer expansion represents the diffuse flow in the rest of the domain.

The asymptotic results summarized above are derived for two-dimensional flows. However, the theory can be easily extended to three dimensions (see [54]) so the ideas presented in this chapter apply to three dimensional problems as well. From (4.0.4) it is clear that when the contrast is high (ϵ is small), the potential $\phi(x, y)$ changes abruptly near the saddle point. In order to avoid numerical difficulties due to this behavior, the hybrid numerical method uses the asymptotic result (4.0.4) in the regions of flow channeling and matches it with the numerically computed solution elsewhere in the flow regime.

1 The numerical method

1.1 Standard finite difference schemes

We can solve (4.0.1)-(4.0.3)with a variety of numerical methods but for simplicity we concentrate on a second order finite difference scheme with a uniform discretization of the domain Ω (see [63]). We introduce a mesh which has N grid points and equal spacing $h = \frac{1}{N}$ in both the horizontal and vertical direction. The position of the grid points is given by

$$(i,j) \rightarrow x_i = (i-1)h, \quad y_j = (j-1)h, \quad i,j = 1,\ldots N+1 \tag{4.1.8}$$

and we use the notation

$$\begin{aligned} \phi_{i,j} &= \phi(x_i, y_j), \\ \sigma_{i,j} &= \sigma(x_i, y_j), \\ f_{i,j} &= f(x_i, y_j). \end{aligned} \tag{4.1.9}$$

Equation (4.0.1) is equivalent to

$$\sigma \Delta \phi + \nabla \sigma \cdot \nabla \phi = -f(x,y), \tag{4.1.10}$$

which is discretized with a central difference scheme as

$$\begin{aligned} &\sigma_{i,j} \frac{(\phi_{i-1,j} + \phi_{i,j-1} - 4\phi_{i,j} + \phi_{i,j+1} + \phi_{i+1,j})}{h^2} \\ &\quad + \frac{(\sigma_{i+1,j} - \sigma_{i-1,j})}{2h} \frac{(\phi_{i+1,j} - \phi_{i-1,j})}{2h} + \\ &\frac{(\sigma_{i,j+1} - \sigma_{i,j-1})}{2h} \frac{(\phi_{i,j+1} - \phi_{i,j-1})}{2h} = -f_{i,j}. \end{aligned} \tag{4.1.11}$$

At the boundaries $i = 1$ or $N+1$ and $j = 1$ or $N+1$ we have from (4.0.2)

$$\begin{aligned} &\frac{\phi_{2,j} - \phi_{0,j}}{2h} = 0, \qquad \frac{\phi_{N+2,j} - \phi_{N,j}}{2h} = 0, \\ &\frac{\phi_{i,2} - \phi_{i,0}}{2h} = 0, \qquad \frac{\phi_{i,N+2} - \phi_{i,N}}{2h} = 0. \end{aligned} \tag{4.1.12}$$

Equations (4.1.11) and (4.1.12) can be written in matrix form (see [63]) as

$$A\mathbf{\Phi} = \mathbf{F}, \tag{4.1.13}$$

where $\mathbf{\Phi} \in \mathbb{R}^{(N+1)^2 \times 1}$ is the vector of unknowns $\phi(x_i, y_j)$, $i,j = 1, N+1$ and $\mathbf{F} \in \mathbb{R}^{(N+1)^2 \times 1}$ is the vector of the driving force f_{ij}. Since the potential is unique up to an additive constant only, we fix it by specifying $\phi(x,y)$ at some grid point. The linear system of equations (4.1.13) can be solved for $\mathbf{\Phi}$, which gives then the potential gradient $\nabla\phi$ and current $\mathbf{j} = -\sigma\nabla\phi$.

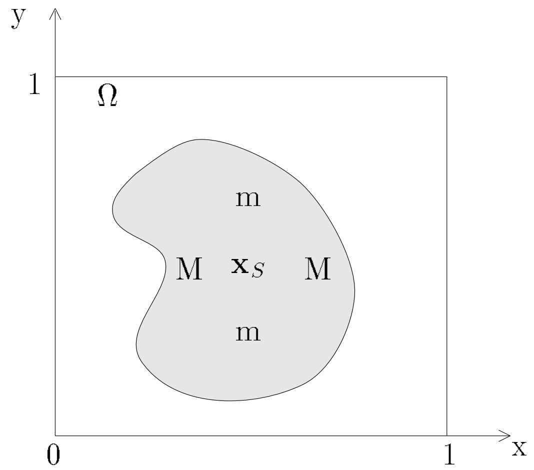

Figure 4.1.2: Region of high contrast of σ in Ω

1.2 The hybrid method

We first explain our method in the simple case shown in Fig. 4.1.2. We assume that the conductivity function $\sigma(x, y)$ is continuous and differentiable and that it has a high contrast region inside Ω (see shaded region in Fig. 4.1.2). Let us assume that σ has only one saddle point $\mathbf{x}_s$, two minima and two maxima denoted in Fig. 4.1.2 by m and M, respectively. If the contrast in the shaded region is very high, as we explained in chapter 2, we can assume that $\sigma(\mathbf{x}) = \sigma_0 \exp(-\frac{S(\mathbf{x})}{\epsilon^2})$, where $S(\cdot)$ is a smooth function, σ_0 is a constant and ϵ is a small parameter.

We define the modified domain $\Omega \setminus D$ as shown in Fig. 4.1.3. Inside the small box D centered at the saddle point the potential $\phi(x, y)$ has the expression (4.0.4). The constant C quantifies the flux through the saddle point and it is treated as an unknown. To compute C beforehand, we would need the effective conductivity for the smooth regions of σ, which is clearly unknown. Thus, we introduce the hybrid method where the flux C is computed numerically.

The hybrid method solves (4.0.1) in $\Omega \setminus D$ with Neumann boundary conditions (4.0.2) at the outer boundary, and Dirichlet boundary conditions (4.0.4) at the inner boundary. In order to have as many equations as unknowns we need an additional equation for the unknown flux C. We observe that if we integrate (4.0.1) over the

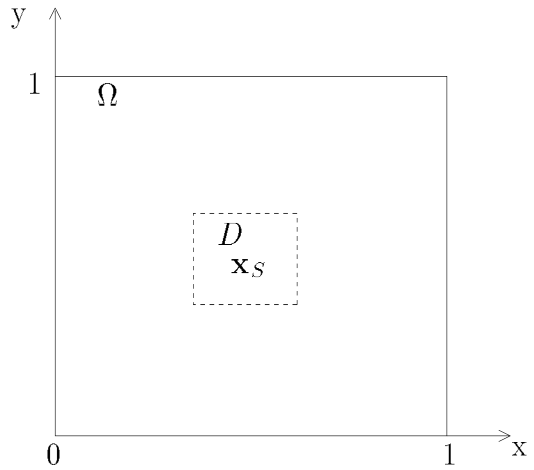

Figure 4.1.3: Modified numerical domain

rectangular domain Λ shown in figure 4.1.4, we obtain

$$-\int_{\Lambda} \nabla \cdot (\sigma \nabla \phi) d\mathbf{x} = -\int_{\partial \Lambda_E} (\sigma \nabla \phi) \cdot \mathbf{e}_1 dy = \int_{\Lambda} f(x,y) d\mathbf{x}, \tag{4.1.14}$$

which is the additional equation we needed. We discretize equation (4.0.1) and the no-flux boundary conditions (4.0.2) as explained in section 4.1.1. The discretization of the additional equation (4.1.14) can be done with any quadrature rule; we used the trapezoidal rule for integration. In the end we obtain a linear system of equations with unknowns $\phi(x_i, y_j)$, $(x_i, y_j) \in \Omega \setminus D$ and flux C which we solve with a direct solver for banded matrices (see [55]).

In order to prescribe the size of the inner box D, we keep in mind that the potential gradient inside is a Gaussian centered at the saddle point and decaying in the x direction. It is known that at a distance equal to three standard deviations, the Gaussian is close to zero. Since we must match the flux entering the box with that inside, the box should be smaller than this. However, we want to choose it as large as possible in order to eliminate numerical computations for the high contrast region. Consequently, we choose the size of the box in the x direction so that $\sqrt{\frac{k}{2\epsilon^2}} \mid x - x_s \mid \sim 2$ and similarly in the y direction $\sqrt{\frac{p}{2\epsilon^2}} \mid y - y_s \mid \sim 2$.

The method described in this section can be generalized to any number of saddle points. We illustrate the generalization by considering a conductivity function with

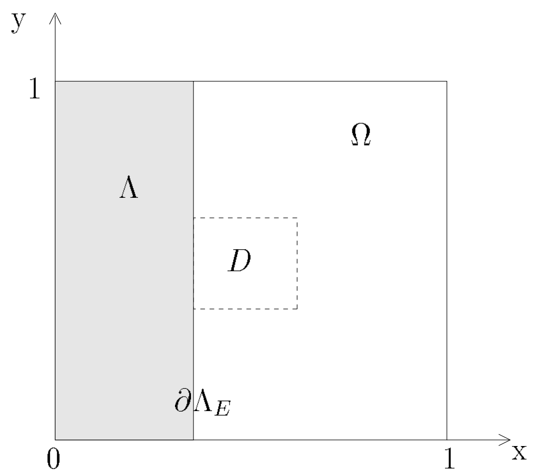

Figure 4.1.4: Domain of integration for computing the flux through the saddle

the geometry shown in Fig. 4.1.5. The local maxima, minima, and saddle points of the conductivity are denoted by M, m and $\mathbf{x}_i$ respectively. The saddle points $\mathbf{x}_1$ and $\mathbf{x}_2$ are oriented in the x direction, while the other two saddle points $\mathbf{x}_3$ and $\mathbf{x}_4$ are in the y direction. In a small neighborhood of each saddle point the potential gradient has an expression similar to (4.0.5) i.e., it is oriented in the direction of the saddle and its magnitude is a Gaussian centered at it. Exactly as we did before, we surround the saddle points by small boxes and we solve the problem (4.0.1) numerically in the rest of the domain. At the outer boundary we have the no-flux boundary conditions (4.0.2) and at the inner boundaries we prescribe the potential gradient (4.0.5).

As before, the potential gradient inside the boxes is known up to a multiplicative constant that quantifies the flux through the saddle. These constants are considered to be unknowns and in order to determine them we introduce four additional equations. They are similar to (4.1.14) and have the form

$$-\int_{\Lambda_i} \nabla \cdot (\sigma \nabla \phi) d\mathbf{x} = -\int_{\partial \Lambda_i} \sigma \nabla \phi \cdot \mathbf{n} ds = \int_{\Lambda_i} f(x,y) d\mathbf{x}, \; i = 1, \ldots 4 \tag{4.1.15}$$

with an example of the integration domains Λ_i shown in figure 4.1.6. Equations (4.1.15) are discretized as before and introduced in the linear system of equations which is solved for the unknown potential and fluxes through each saddle.

Since the key idea in our hybrid method is the use of the asymptotic expression

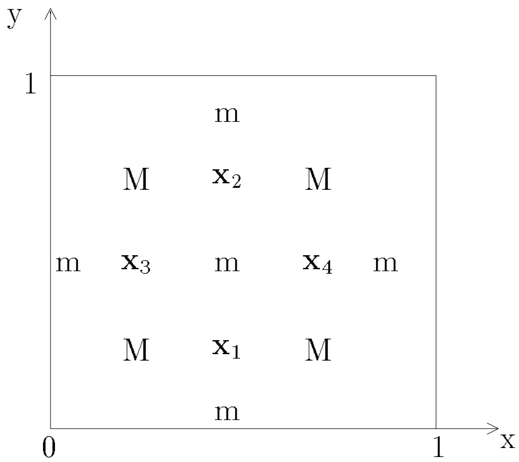

Figure 4.1.5: Geometry of σ

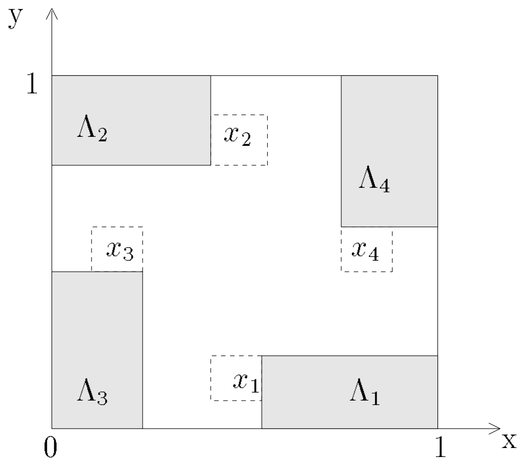

Figure 4.1.6: Modified domain

of the potential in regions of strong flow (channels or saddles of σ), one can use any numerical method in the rest of the domain where the flow is diffuse. The finite difference scheme described in section 4.1.1 is an example. Even though we only consider two-dimensional flow problems, as we mentioned in the introduction of this chapter, the methods can be extended to three dimensions.

2 Performance of the hybrid method

In this section we present the results of numerical computations that test the performance of the hybrid method. In our tests we consider conductivities σ with geometries described in section 4.1.2 and we vary the contrast and driving conditions. For comparison we used two additional numerical methods.

One is the standard finite difference scheme described in section 4.1.1. This scheme is second order accurate and uses a uniform discretization of the domain. We expect that the performance of this method should be rather poor because the regions of flow channeling in Ω need a very fine discretization in order to capture the correct behavior of the solution. To give an acceptable answer, the finite difference scheme must use a very fine mesh which leads to an extremely large and ill-conditioned matrix that must be inverted. We include in this section the experiments performed with this naive numerical scheme in order to point out its shortcomings.

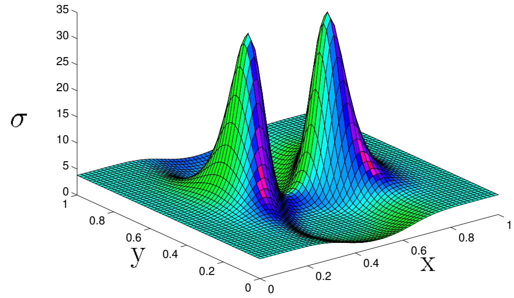

Figure 4.2.7: Conductivity function

The other numerical method we used is PLTMG (see [7]), a carefully designed general purpose solver for elliptic partial differential equations. It is a multigrid solver with a finite element discretization based on continuous piecewise linear triangular elements and it provides for adaptive mesh refinement. This solver performs much better than the second order finite difference scheme, but we will see that in some cases it does not correctly solve the problem in the high contrast regions of the conductivity.

2.1 One subregion of high contrast

In this section we assume that the conductivity has a single high contrast region where $\sigma = \sigma_0 e^{-\frac{S(\mathbf{x})}{\epsilon^2}}$, with $S(\cdot)$ a smooth function, σ_0 constant and ϵ small. In this region σ has a single saddle point (channel) at (0.5,0.5), two maxima at $(0.35, 0.5)$ and$(0.65, 0.5)$ and two minima at $(0.5, 0.35)$ and $(0.5, 0.65)$. The orientation of the saddle is such that flow is in the x direction. In the rest of the domain σ is fairly flat. In Fig. 4.2.7 we show an example of the conductivity we use. We vary the contrast $(\max(\sigma)/\min(\sigma))$ by changing the parameter ϵ.

To test the performance of the hybrid method for different contrasts, in the first set of computations we fix the positions of the source and sink at $(0.2, 0.2)$ and $(0.8, 0.8)$, and the curvatures at the saddle $k = 86.76$ and $p = 59.95$ and then vary the parameter ϵ that controls the contrast of the conductivity. We give the results

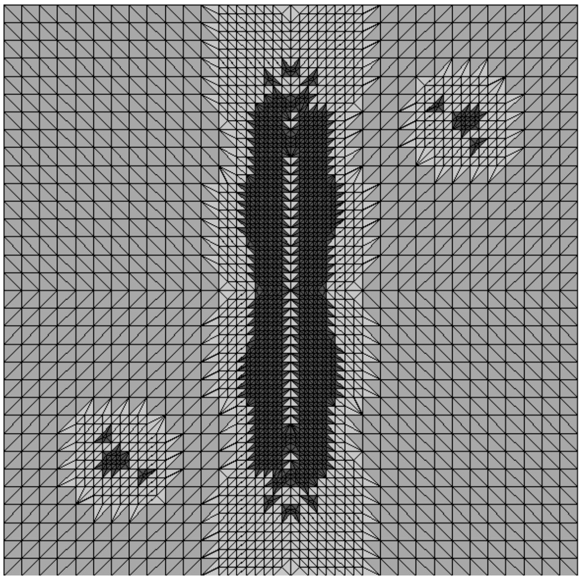

Figure 4.2.8: Grid used by PLTMG for contrast $6 \cdot 10^4$

$\sigma(x_s)$	ϵ^2	Contrast
3.49	0.08	10^6
2.72	0.1	$6 \cdot 10^4$
1.95	0.15	10^3

Table 4.2.1: One saddle parameters

of three computations with the parameters shown in table 4.2.1. The grids used in each computation are shown in table 4.2.2, where the hybrid and finite difference method have uniform meshes and PLTMG has four grid levels, with the coarsest level described by the grid spacing h_{max} and the finest level described by h_{min}. In figure 4.2.8 we show the grid used by PLTMG for the contrast $6 \cdot 10^4$ and note the local refinement around the high contrast region and sources. The hybrid method has for all three experiments an inner box of size $| x - x_s | \leq 0.084$ and $| y - y_s | \leq 0.1$. This box size is determined according to the remarks in section 4.1.2 for the highest contrast case and it could be slightly larger for the lower contrast computations. In

Hybrid M.	Finite Diff.	PLTMG
$h = \frac{1}{32}$	$h = \frac{1}{64}$	$h_{max} = \frac{1}{32}$; $h_{min} = \frac{1}{256}$

Table 4.2.2: Numerical grids

Fig. 4.2.9 we show the flow computed with the hybrid method when the contrast is 10^6. The flows that result with the other two methods look similar so we must use a quantitative criterion for comparing their performance. We note that if we integrate the flux in the x direction along vertical lines in the domain Ω we have

$$\chi(x) = \int_0^1 \mathbf{j} \cdot \mathbf{e}_1 dy - \int_0^1 dy \int_0^x dx f(x,y) = 0. \tag{4.2.16}$$

This result follows from the divergence theorem and equations (4.0.1) and (4.0.2). A similar condition is satisfied by the flux in the y direction.

$$\Delta(y) = \int_0^1 \mathbf{j} \cdot \mathbf{e}_2 dx - \int_0^1 dx \int_0^y dy f(x,y) = 0. \tag{4.2.17}$$

If the forcing terms were exactly (4.0.3), we would have

$$\int_0^1 \mathbf{j} \cdot \mathbf{e}_1 dy = \begin{cases} 0 & if \quad x < 0.2 \quad or \quad x > 0.8 \\ 1 & \text{otherwise} \end{cases} \tag{4.2.18}$$

and

$$\int_0^1 \mathbf{j} \cdot \mathbf{e}_2 dx = \begin{cases} 0 & if \quad y < 0.2 \quad or \quad y > 0.8 \\ 1 & \text{otherwise.} \end{cases} \tag{4.2.19}$$

Since we do not have delta functions for the source and sink, but rather very narrow Gaussians, the integrals over the horizontal and vertical fluxes will be smoothed versions of (4.2.18) and (4.2.19). We test the accuracy of the solution computed with each one of the three numerical methods by looking at the absolute and relative errors of the net horizontal and vertical fluxes given by (4.2.16)-(4.2.19).

In Fig. 4.2.10 we plot the absolute error $\mid \chi(x) \mid$ obtained with the three different numerical methods for the contrast 10^6. The solid line corresponds to the hybrid

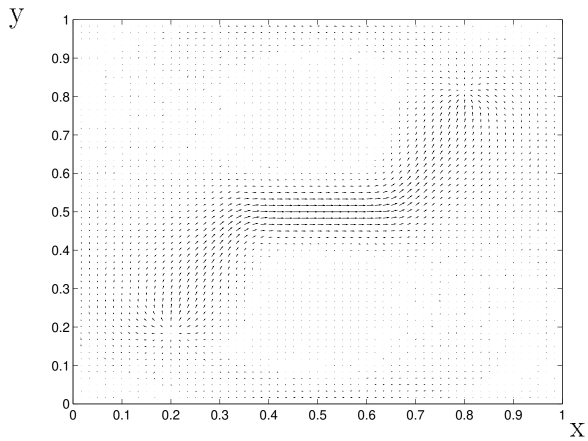

Figure 4.2.9: Source / sink at $(0.2, 0.2)$ and $(0.8, 0.8)$, contrast 10^6

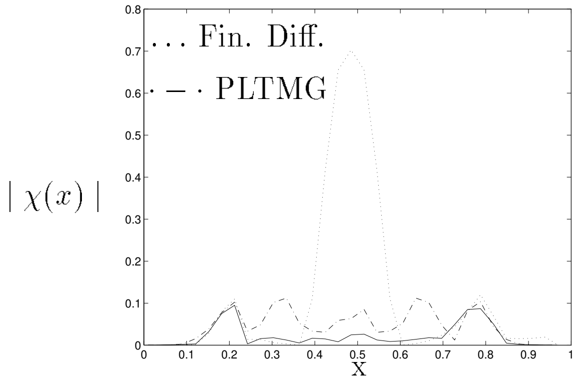

Figure 4.2.10: Error in the net horizontal flux for contrast 10^6

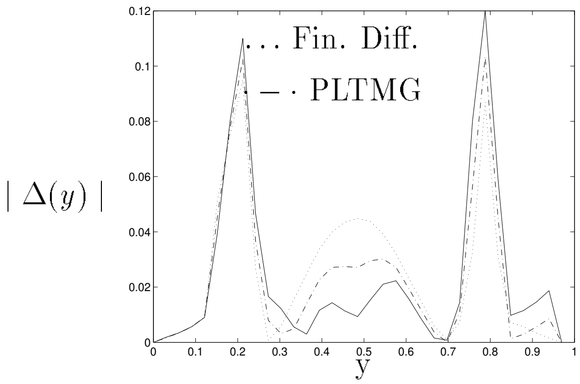

Figure 4.2.11: Error in the net vertical flux for contrast 10^6

method, the dotted line to the finite difference method, and the dash-dot line to the PLTMG solver. We see from this picture that the error given by all three methods is large (absolute error~ 0.1, relative error $\sim 20\%$) around the "point" source and sink. Fig. 4.2.10 also shows that if we are slightly away from the source and sink the hybrid method gives a very good result (the absolute and relative error is less than 0.03). The net horizontal flux given by PLTMG has large oscillations in the high contrast region; the relative error around the channel ($x \sim 0.5$) is about 10%. PLTMG built an adaptively refined grid consisting of 5100 vertices. For less refined meshes, the error around the channel was considerably larger ($\sim 30\%$). Thus, even though the solution given by PLTMG seems not much worse than the one computed with the hybrid method, the computational cost due to the mesh refinement is much higher. The finite difference scheme gives a very inaccurate result in the high contrast region and it seems to overestimate substantially the flux through the saddle. The errors in the net vertical flux (4.2.17) are shown in Fig. 4.2.11 and once again they are relatively large near the source and sink. In the rest of the domain all three methods give a small error $\mid \Delta(y) \mid$ although the hybrid method is slightly better. This is expected because flow channeling occurs only in the x direction and the flow in the y direction is diffuse and well resolved by all three methods.

For the other two computations in table 4.2.1, we lowered the contrast and used the same criteria (4.2.16)-(4.2.19) for the solution. The error $\mid \Delta(y) \mid$ in vertical flux, not being affected by the channel, remained similar to the one shown in Fig. 4.2.11. The error $\mid \chi(x) \mid$ in the net horizontal flux given by the hybrid method remained as small as the one shown in Fig. 4.2.10. PLTMG gave an improved result in the high contrast region; the error did not have the large amplitude oscillatory behavior we saw in Fig. 4.2.10 but remained about (10%) in the neighborhood of the saddle point. The finite difference method gave, as expected, the worst solution even though the results improved when the contrast was lowered. In all three experiments, the error around the source and sink remained constant because the sources are situated away from the high contrast region.

To see where the solution computed with the hybrid method differs from the solution given by the other numerical schemes, we look at the contour plots of the difference in the fluxes obtained with the finite difference and hybrid methods, and with PLTMG and the hybrid method, respectively for contrast 10^6. In figures 4.2.12, 4.2.13 we show the relative errors which are obtained by normalizing the flux difference with the flux given by the hybrid method. From these figures we can see that the error in the horizontal flux $j_x = \mathbf{j} \cdot \mathbf{e}_1$ is quite large only in the high contrast region, as expected. The error in the vertical flux is much smaller ($\sim 3\%$) and has no particular localization in Ω.

In the second set of numerical computations we examine the dependence of the performance of the hybrid method on the position of the source and sink. We fix the

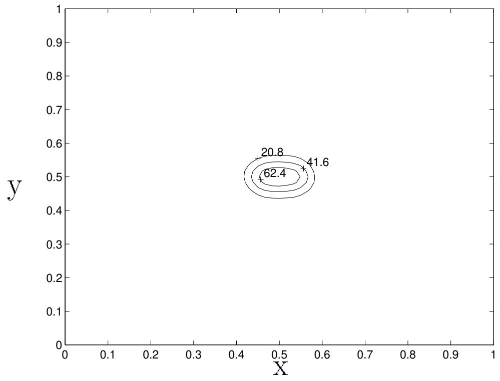

Figure 4.2.12: Second order Finite Difference: Rel. error in J_x (%)

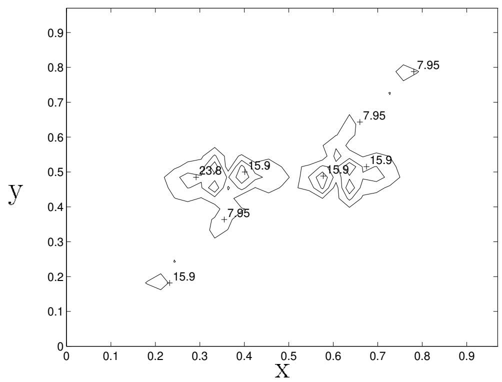

Figure 4.2.13: PLTMG: Relative error in J_x (%)

Source	Sink	$\mid \chi(x) \mid$
(0.2,0.2)	(0.8,0.8)	0.015
(0.2,0.2)	(0.8,0.2)	0.013
(0.4,0.4)	(0.8,0.8)	0.014

Table 4.2.3: Hybrid solution error sensitivity to source location

curvatures at the saddle point, $k = 86.76$ and $p = 59.95$, the height of the saddle to $\sigma(x_s) = 3.49$ and the contrast to 10^6 (i.e., $\epsilon^2 = 0.08$). As explained in section 4.1.2 the size of the inner box is chosen to be

$$\mid x - x_s \mid \leq 0.084, \quad \mid y - y_s \mid \leq 0.1.$$

In table 4.2.3 we summarize the results of three computations, where the first two columns give the position of the source and sink and the last column gives the error $\mid \chi(x) \mid$ in the high contrast region ($x \sim 0.5$) when the hybrid method is used. The error $\mid \Delta(y) \mid$ in the vertical flux is not affected by the channeling and remains similar to the one shown in Fig. 4.2.11. The results shown in table 4.2.3 indicate that the performance of the hybrid method is independent of the position of the source and sink provided that they are not in a very small neighborhood of the saddle point of σ.

We saw in the first part of this section that for the first experiment in this set the solution computed by the finite difference method was quite inaccurate. The results are basically the same for all three positions of the source and sink presented here. For the first two experiments in the table, the accuracy of the solution computed by PLTMG remained similar to what we saw in Fig. 4.2.10. However, in the third experiment, where the source is close to the channel, the error in the high contrast region is as high as 70%. We may thus conclude that in the high contrast region the two other numerical methods have difficulties, while in the flat regions of the conductivity they perform well. In order for the finite difference method to have small horizontal flux error (4.2.16), we needed a uniform discretization of the domain with a grid spacing of $h \sim 1/120$ for contrast 10^3 and $h \sim 1/200$ for contrast $6 \cdot 10^4$. For the highest contrast case we could not obtain an accurate result because of limited computer memory. The finest grid we considered had $h = 1/240$ grid points and the result was not satisfactory. PLTMG gave accurate solutions and used reasonable meshes for problems with contrast $\sim 10^2$. For higher contrasts, the solution was always less accurate than the one given by the hybrid method, although we obtained acceptable results when we used very finely refined meshes. When the sources were placed in the neighborhood of the channel the errors in the high contrast region were quite high and did not improve considerably when the mesh was locally refined.

2.2 Four subregions of high contrast

In this section we consider a conductivity that has four regions of flow concentration (i.e., saddle points) in the domain (see Fig. 4.1.5). Inside Ω, σ has four maxima at $(0.225, 0.225)$, $(0.775, 0.225)$, $(0.225, 0.775)$ and $(0.775, 0.775)$, five minima at $(0.5, 0.5)$, $(0.5, 0.05)$, $(0.5, 0.95)$, $(0.15, 0.5)$ and $(0.85, 0.5)$ and four saddle points at $(0.5, 0.225)$, $(0.5, 0.775)$, $(0.225, 0.5)$ and $(0.775, 0.5)$. Two saddles allow flow in the x direction whereas the other two are oriented in the y direction. The curvatures of the saddles in the x direction are $k = 99.3, p = 75.4$ and the curvatures of the saddles in the y direction are $k = 11.9$, $p = 8.12$. The conductivity used in the computations is similar to the one shown in Fig. 4.2.14, but we vary its contrast $(\max(\sigma)/\min(\sigma))$.

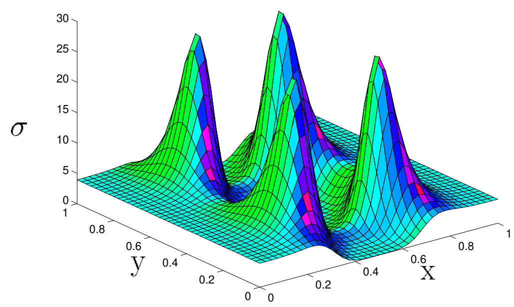

Figure 4.2.14: Conductivity

$\sigma(x_1)$	$\sigma(x_2)$	$\sigma(x_3)$	$\sigma(x_4)$	Contrast
1.5	1.5	4.2	4.2	10^3
3.4	3.4	9.3	9.3	10^6
7.1	7.1	12.4	12.4	10^7

Table 4.2.4: Conductivity in the channels for different contrasts

We assess the performance of the hybrid method for different contrasts with a set of computations whose parameters are shown in table 4.2.4. The source position is $(0.1, 0.1)$ and the sink is at $(0.9, 0.9)$. The curvatures of the saddle points are kept constant but the conductivity and overall contrast are changed. The hybrid method requires four inner boxes which have sizes chosen as explained in section 4.1.2:

$$(x, y) \in [0.44, 0.56] \times [0.18, 0.27],$$

$$(x, y) \in [0.44, 0.56] \times [0.73, 0.83],$$

$$(x, y) \in [0.18, 0.27] \times [0.44, 0.56],$$

$$(x, y) \in [0.73, 0.83] \times [0.44, 0.56].$$

In the rest of the domain we used a uniform grid with spacing $h = 1/32$. The

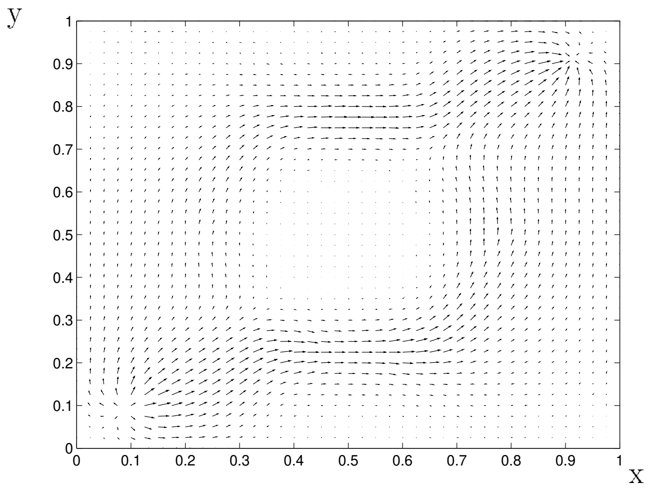

Figure 4.2.15: Source / sink at $(0.1, 0.1)$ and $(0.9, 0.9)$, contrast 10^6

standard finite difference method had a uniform grid with $h = 1/64$ and PLTMG built a sequence of four grid levels with $h = 1/32$ for the coarsest grid and $h = 1/256$ for the finest one.

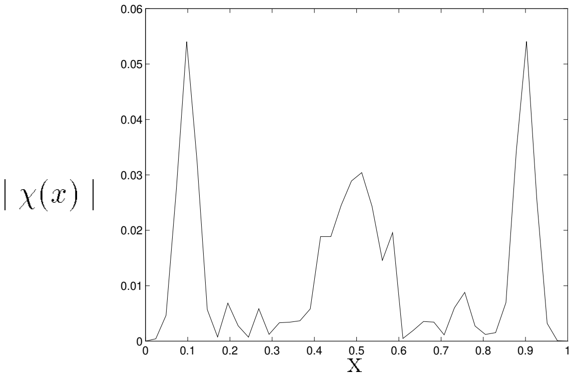

Figure 4.2.16: Source / sink at $(0.1, 0.1)$ and $(0.9, 0.9)$, contrast 10^6

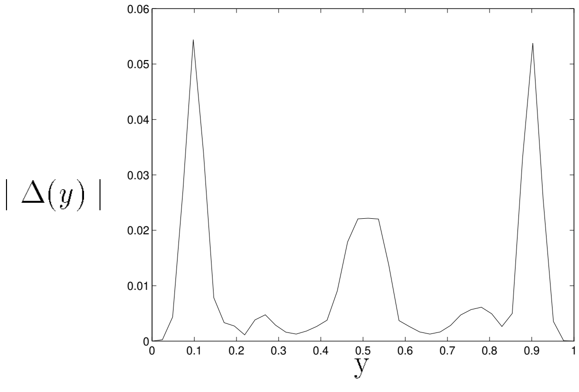

Figure 4.2.17: Source / sink at $(0.1, 0.1)$ and $(0.9, 0.9)$, contrast 10^6

In figure 4.2.15 we show the flow computed with the hybrid method when the contrast is 10^6. For other contrasts the flows are similar although the flow concentration at the saddle points of the conductivity changes. As before we test the accuracy of the solution given by the hybrid method by looking at the errors in the net horizontal and vertical flux (see (4.2.16)-(4.2.19)). In Fig. 4.2.16, 4.2.17 we plot the errors $\mid \chi(x) \mid$, $\mid \Delta(y) \mid$ for the hybrid method when the contrast is 10^6. We note again a large error (relative error $\sim 15\%$) around the source and sink because of the discretization. Around the saddle points ($x \sim 0.5$ or $y \sim 0.5$), the error (relative and absolute) is 0.03. The error $\mid \Delta(y) \mid$ in the vertical flux is very similar to the error in the horizontal flux (see Fig. 4.2.17). For the other cases shown in table 4.2.4, the accuracy of the solution by the hybrid method remained about the same.

In Fig. 4.2.18 we show the horizontal flux ($\int_0^1 \mathbf{j}(x,y) \cdot \mathbf{e}_1 dy$) computed with all three numerical methods. The full line corresponds to the hybrid method, the dotted line to the standard finite difference method and the dash-dot line to PLTMG. We see that in the high contrast region (where the hybrid method was shown to be accurate) the PLTMG solution oscillates about the correct value with large amplitude. The finite difference method gives a poor solution everywhere in the flow regime. When the contrast was lowered to 10^3 the oscillations in the net horizontal flux computed by PLTMG were damped but the hybrid method did better again.

In Fig. 4.2.19 we show the vertical flux ($\int_0^1 \mathbf{j}(x,y) \cdot \mathbf{e}_2 dx$) computed with all three numerical methods and note that PLTMG and the hybrid method give almost the same result. The finite difference method performs worse than the other two but now the error is relatively small. The vertical flux is well resolved by all three methods because the saddles oriented in the y direction are shallow and the vertical flow concentration is weak.

We also tested the hybrid numerical method for problems with four channels when the source and sink are displaced. The results confirmed the conclusion of section 4.2.1 that the performance of the hybrid method is independent of the position of the source and sink as long as they are not very near the saddle points. The other two methods give quite inaccurate solutions when the source or sink are relatively close to the channels. For example, we did an experiment with the source situated at $(0.4, 0.4)$ and the sink at (0.9,0.9) and contrast 10^6. The flow computed with the hybrid method is shown in Fig. 4.2.20. The finite difference method gave relative errors in the net vertical and horizontal fluxes of about 150%. In order to obtain an acceptable result with PLTMG we used a very fine mesh (6000 vertices) but the quality of the solution remained inferior to the one computed with the hybrid method.

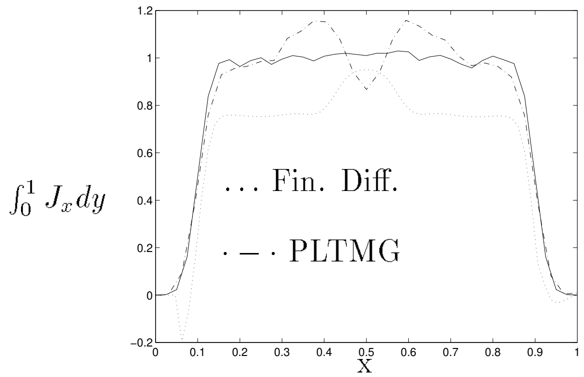

Figure 4.2.18: Source / sink at $(0.1, 0.1)$ and $(0.9, 0.9)$, contrast 10^6

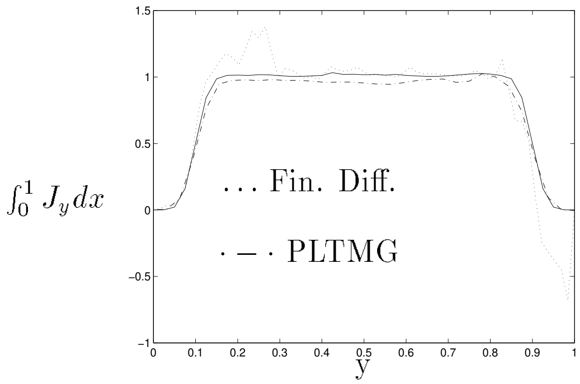

Figure 4.2.19: Source / sink at $(0.1, 0.1)$ and $(0.9, 0.9)$, contrast 10^6

The results presented in this section lead us to the conclusion that potentials in high contrast media can be computed more accurately and efficiently with the hybrid numerical method than with even a well designed, general purpose, adaptive numerical solver like PLTMG. This is not surprising because a general purpose code that can handle discontinuous and nonlinear problems with automated grid refinement cannot be expected to do as well as a specially designed method that works for a limited class of problems, like the hybrid method for high contrast media. The numerical computations presented here make precise the range of applicability of PLTMG for high contrast media and quantify the extent to which special methods can do better.

2.3 Dependence of performance on the size of the inner box

In this section we study how the size of the inner box in the hybrid method influences its performance. We consider only the problem with a single saddle point described in section 4.2.1.

The parameters are chosen as follows: $k = 86.76$, $p = 59.95$, $\epsilon^2 = 0.08$ (i.e., contrast $= 10^6$) and the position of the source and sink are $(0.2, 0.2)$ and $(0.8, 0.8)$,

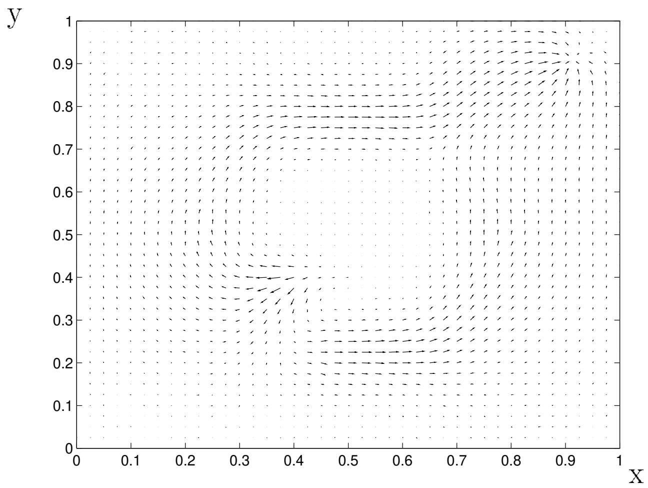

Figure 4.2.20: Source / sink at $(0.4, 0.4)$ and $(0.9, 0.9)$, contrast 10^6

respectively. According to the rule for the size of the inner box given in section 4.1.2 we have

$$\sqrt{\frac{86.76}{2 \cdot 0.08}} \mid x - x_s \mid \sim 2, \qquad \sqrt{\frac{59.95}{2 \cdot 0.08}} \mid y - y_s \mid \sim 2, \tag{4.2.20}$$

which means

$$\mid x - x_s \mid \leq 0.084, \qquad \mid y - y_s \mid \leq 0.1. \tag{4.2.21}$$

We did a computation with the rectangular inner box given by

$$\mid x - x_s \mid \leq 0.1, \qquad \mid y - y_s \mid \leq 0.1,$$

which is equivalent to having $\sqrt{\frac{86.76}{2 \cdot 0.08}} \mid x - x_s \mid = 2.33$. The results are not satisfactory. The solution should satisfy (4.2.16) and (4.2.17) and in Fig. 4.2.21 we plot $\int_0^1 j_x dy$ (dash - dot line) and $\int_0^1 dy \int_0^x dx f(x, y)$ (full line). The error is very large in the high contrast region because the box is too large. We compute the flow through the box by using (4.1.14) in which the flux C multiplies the potential difference at the boundary of the box. If the size of the box is too large, the Gaussian in the expression of the potential gradient (see (4.0.5) is too small and leads to an overestimation of the flux constant C when we use equation (4.1.14). The result is good for the test (4.2.17) because it only involves the flux in the y direction which is not affected by the presence of the high contrast region.

In the next computation we use an inner box defined by

$$| x - x_s | \leq 0.06, \quad | y - y_s | \leq 0.1,$$

which is equivalent to having $\sqrt{\frac{86.76}{2 \cdot 0.08}} \mid x - x_s \mid = 1.3965$. The results are shown in figure 4.2.22 and are unsatisfactory as well. It is clear that we have underestimated the flux in the high contrast region with an inner box that is too small. We left a part of the difficult high contrast region uncovered and, as we saw before, the finite difference method does not handle it well. The effect is exactly the opposite of the one we had before. The finite difference method overestimates the flow which enters the inner box so equation (4.1.14) gives a value for the flux C that is too small. As in the previous computation, the vertical flux is computed accurately.

In all of our numerical computations we found that the choice

$$\sqrt{\frac{k}{2\epsilon^2}} \mid x - x_s \mid \sim 2, \quad \sqrt{\frac{p}{2\epsilon^2}} \mid y - y_s \mid \sim 2 \tag{4.2.22}$$

was optimal, for several different contrasts. The computations with lower contrast gave good results for other sizes of the box as well. For example, for a contrast of 10^4 we obtained good hybrid method performance with box sizes

$$\sqrt{\frac{k}{2\epsilon^2}} \mid x - x_s \mid \in [1., 2.5].$$

We note that the numerical computations that we did with the more complicated problem that has four saddle points, described in section 4.2.2, behave the same way as far as box sizes are concerned.

3 Enhancement of the network approximation with the hybrid numerical method

In this section we discuss the asymptotic network approximation of [54, 18] and assess its limitations using numerical results. We saw in previous sections that even adaptive numerical methods cannot solve the conductivity problem efficiently when σ has very high contrast. A combination of the asymptotic results and numerical

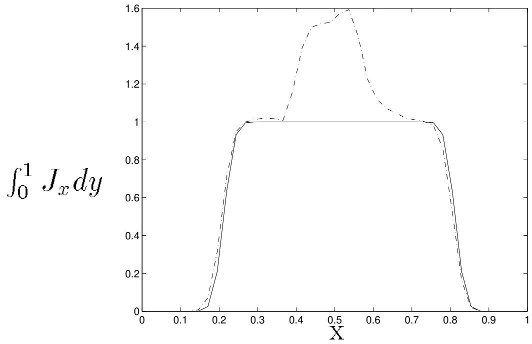

Figure 4.2.21: contrast 10^6, box too large

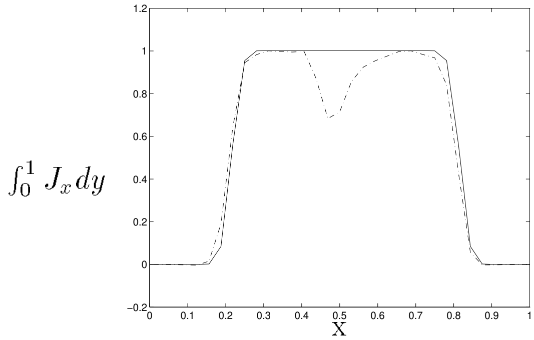

Figure 4.2.22: contrast 10^6, box too small

methods leads to a much better solver, as might be expected. We will now consider how well the asymptotic theory alone describes the flow behavior in different high contrast situations.

As we explained in chapter 2, the asymptotic approximation was obtained under the assumption that the high contrast of the conductivity σ dominates the behavior of the flow. The asymptotic analysis and the variational principles show that the flow in such media can be described by an equivalent network of channels placed at the saddle points of $\sigma(\cdot)$. The equivalent network description is a consequence of the almost discrete flow behavior (i.e., channeling) in materials with high contrast conductivity. Because of the similarity of the problem we are studying with the electric current flow problem in a material with resistance $\rho = \sigma^{-1}$, we can view the network as consisting of resistors $\overline{R}$ given by (4.0.7). Network equivalences were also used in other studies, see for example [53]. In the electric network context the potential gradient is $-\nabla\phi$ and the electric current is the flux $\mathbf{j} = -\sigma\nabla\phi$. In this section we use the hybrid numerical method to test the validity of the asymptotic network approximation and understand its limitations.

3.1 One subregion of high contrast

We assume that the conductivity function has the geometry shown in figure 4.1.2. Inside Ω there is a region of high contrast where $\sigma \sim \sigma_0 e^{-\frac{S(\mathbf{x})}{\epsilon^2}}$, where $S(\cdot)$ is smooth and ϵ is a small parameter. We also assume that σ has only one saddle point oriented

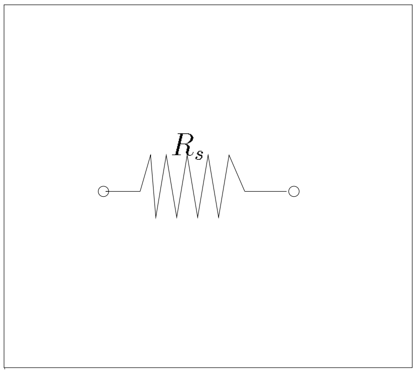

Figure 4.3.23: Asymptotic network

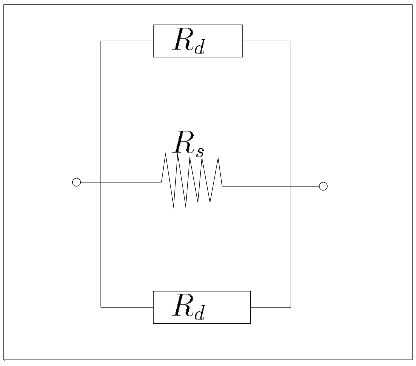

Figure 4.3.24: Corrected network

in the x direction, near which

$$\sigma \sim \sigma(\mathbf{x}_s) \cdot \exp[\frac{k(x-x_s)^2}{2\epsilon^2} - \frac{p(y-y_s)^2}{2\epsilon^2}], \tag{4.3.1}$$

where k and p are the curvatures at the saddle. If the saddle has an arbitrary orientation (4.3.1) is still valid in a local system of coordinates with x denoting the direction of the saddle. The asymptotic network theory predicts that nearly all the flow passes through the saddle and that the equivalent network describing this problem consists of a resistor $R_s = \frac{1}{\sigma(\mathbf{x}_s)}\sqrt{\frac{p}{k}}$ placed at the saddle point $\mathbf{x}_s$ (see Fig. 4.3.23).

To test the validity of the asymptotic network approximation, we consider the conductivity $\sigma(x, y)$ used in section 4.2.1 and we keep the position of the critical points fixed while varying the contrast, curvatures, and height of the saddle. To have flow through the resistor R_s, we must have the source and sink on opposite sides of the saddle. Thus, we take the positions of the source and sink at $(0.2, 0.2)$ and $(0.8, 0.8)$, respectively. The extreme cases one might encounter are when all the flow or none of it passes through the saddle. The first case corresponds to the problem analyzed in [54, 18]. In this situation the flux C appearing in the expression of the potential (4.0.4) can be calculated analytically. From Ohm's law and (4.0.5), we obtain the flux around the saddle

$$\mathbf{j} \approx 2C\sigma(\mathbf{x}_s)\sqrt{\frac{k}{2\pi\epsilon^2}}e^{-\frac{p}{2\epsilon^2}(y-y_s)^2}\mathbf{e}_1. \tag{4.3.2}$$

If all the flow passes through the saddle, we obtain from (4.0.1), (4.0.2), (4.0.3) and the divergence theorem that

$$\int_{|y-y_s|<\eta} \mathbf{j} \cdot \mathbf{e}_1 dy = 1, \tag{4.3.3}$$

where η is a small number such that $\frac{\eta}{\epsilon} \to \infty$ when $\epsilon \to 0$. By using (4.3.2), (4.3.3) and (4.0.7), we easily obtain

$$C = \frac{1}{2\sigma(\mathbf{x}_s)}\sqrt{\frac{p}{k}} = \frac{R_s}{2}. \tag{4.3.4}$$

If the asymptotic network theory is a good approximation of our problem, the flux C computed numerically should be close to the one predicted by (4.3.4).

We expect the amount of flow through $\mathbf{x}_s$ to depend on the effective resistance R_s of the high contrast region and on the effective resistance of the flat region between the source and sink. If the resistance R_s is much smaller than the one of the background, most of the flow should pass through the saddle point. If R_s is comparable to the background resistance, only some of the flow will pass through the saddle point, the rest will be diffuse. Finally when R_s is much higher than the background resistance, only a small amount of flow is expected to cross the high contrast region.

To illustrate this behavior, we consider three computations. The value of the parameter ϵ is fixed, $\epsilon^2 = 0.08$, which gives us a contrast of 10^6. The height of the saddle as well as the curvatures k and p are different for each computation. The parameters chosen in each case as well as the results are given in table 4.3.5, where the first column gives the ratio between the height of the saddle $\sigma(\mathbf{x}_s)$ and the background conductivity, and the last column shows the percentage of the flow through the saddle point. All computations were done with a resolution of 32 grid points in each direction and the inner box size was chosen as explained in section 4.1.2.

In the first computation the resistance at the saddle point is three times smaller than the one of the background. The flow must pass to the other side of the high contrast region in order to reach the sink and the path of least resistance is clearly through the saddle. The diffuse flow encounters a cumulative resistance R_d that is larger than R_s. The network model has the resistor R_s connected in parallel with two other resistors corresponding to the regions of diffuse flow above and below the

$\sigma(x_s)$ / σ_b	σ	p	R_s	C	%
3.49	71.06	66.30	0.0227	0.01097	97
0.28	86.76	59.95	0.24	0.1009	85
0.10	94.75	56.85	0.0624	0.0202	63.5

Table 4.3.5: Parameters and results for single saddle numerical experiments

saddle point, as shown in figure 4.3.24. When the resistances R_d of the diffuse regions are much higher than R_s then almost all the flow passes through the saddle point and the asymptotic network shown in figure 4.3.23 is a good approximation. The flow pattern is shown in figure 2.2.9 where the flow concentration at the saddle point is evident.

For the other two computations we increased the resistance R_s relative to the background. The resistances R_d (figure 4.3.24) of the diffuse regions play a more important role in the circuit and only part of the flow is through the saddle. For the last computation shown in table 4.3.5, only 63.5% of flow is through R_s so the asymptotic network approximation (figure 4.3.23) is not so good anymore. The flow pattern for this last case (figure 4.3.25) is very similar to what we had before, except that we notice diffuse flow above and below the high contrast region.

Next we consider the dependence of the flux through the saddle point on the contrast. We fix the curvatures at $k = 71.06$ and $p = 66.30$ and we vary ϵ (i.e., the contrast). We assume that the conductivity at the saddle is higher than the one of the background and that the ratio $\sigma(x_s)/\sigma_b$ increases as $\epsilon \to 0$. The results are shown in table 4.3.6, where the last column is the relative error between the flux at the saddle point computed numerically and the one predicted by (4.3.4). When the contrast decreases, the approximation of the flow in the high contrast region by the resistor network R_s becomes less accurate and the ratio between the height of the saddle and the background becomes smaller. This explains the increase in the relative error with ϵ in table 4.3.6.

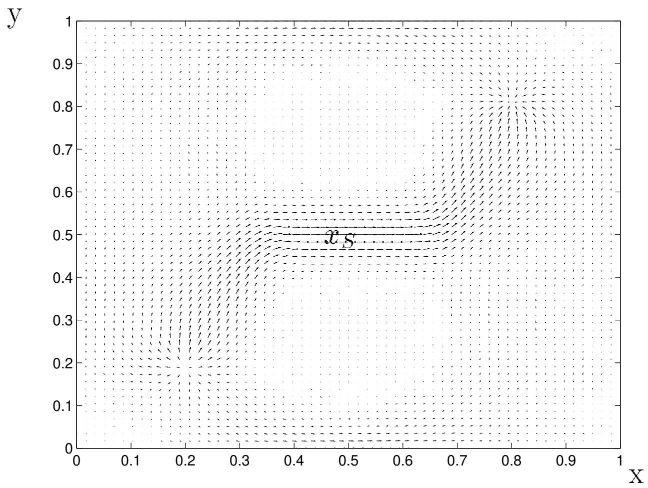

Figure 4.3.25: Higher R_s, 63.5% of flow through $\mathbf{x}_s$

$\sigma(x_s)$ / σ_b	ϵ^2	Contrast	R_s	C	%
3.49	0.08	10^6	0.0227	0.01097	3
2.72	0.1	$5 \cdot 10^4$	0.048	0.0207	13
1.01	0.15	$1.6 \cdot 10^3$	0.13	0.0501	23
0.71	0.19	250	0.214	0.065	39

Table 4.3.6: Accuracy of the network approximation versus contrast

From the computations presented in this section, we conclude that the asymptotic network approximation depends on the parameters of the problem in a more complicated way than the theory suggests. Its validity depends on the ratio between the resistance R_s at the saddle point and the one of the background. Until now we defined contrast as simply the ratio between the maximum and minimum value of the conductivity in the domain. We can also define contrast as the ratio between the conductivity at the saddle point and the one of the background. If this contrast is relatively high, the simple asymptotic network approximation gives a good description of the flow. However, if the contrast is small there is a considerable amount of diffuse flow and by assuming the equivalent network shown in figure 4.3.23 we lose significant information about the problem.

3.2 Four subregions of high contrast

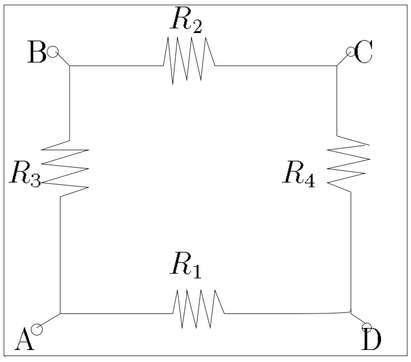

Figure 4.3.26: Asymptotic network

We repeat the calculations of the previous section with the conductivity function of section 4.2.2 that has four saddle points, two of which ($\mathbf{x}_1$ and $\mathbf{x}_2$) are oriented in the x direction while the other two ($\mathbf{x}_3$ and $\mathbf{x}_4$) are in the y direction. Around the saddle points $\mathbf{x}_1$ and $\mathbf{x}_2$ the conductivity function has an expression the form

$$\sigma(x,y) \approx \sigma(\mathbf{x}_i) \cdot \exp[\frac{k_i(x-x_i)^2}{2\epsilon^2} - \frac{p_i(y-y_i)^2}{2\epsilon^2}], \quad i = 1,2 \tag{4.3.5}$$

and around the saddle points $\mathbf{x}_3$ and $\mathbf{x}_4$

$$\sigma(x,y) \approx \sigma(\mathbf{x}_i) \cdot \exp[-\frac{k_i(x-x_i)^2}{2\epsilon^2} + \frac{p_i(y-y_i)^2}{2\epsilon^2}], \quad i = 3,4. \tag{4.3.6}$$

The asymptotic network approximation is shown in figure 4.3.26 where

$$R_i = \begin{cases} \sqrt{\frac{p_i}{k_i}} \frac{1}{K(\mathbf{x}_i)} & i = 1,2 \\ \sqrt{\frac{k_i}{p_i}} \frac{1}{K(\mathbf{x}_i)} & i = 3,4. \end{cases} \tag{4.3.7}$$

To test the validity of the asymptotic network approximation as the source and sink location are displaced we did several computations. We fixed the overall contrast to

Source	Sink
(0.1,0.1)	(0.9,0.9)
(0.4,0.4)	(0.9,0.9)
(0.1,0.1)	(0.9,0.3)

Table 4.3.7: Source-sink locations

10^6 (i.e., $\epsilon^2 = 0.08$), the height of the saddles and conductivity of the background and moved the sources. The curvatures at the saddles are

$$k_i = \begin{cases} 99.3 & i = 1,2 \\ 11.9 & i = 3,4 \end{cases} \tag{4.3.8}$$

and

$$p_i = \begin{cases} 75.4 & i = 1,2 \\ 8.12 & i = 3,4. \end{cases} \tag{4.3.9}$$

The parameters of the computations are shown in table 4.3.7. The saddles in the x direction are much deeper than the ones in the y direction and the ratios between the conductivities at the saddles and the ones of their vicinity are

$$\frac{\sigma(\mathbf{x}_i)}{\sigma_b} = \begin{cases} 30.15 & i = 1,2 \\ 1.38 & i = 3,4. \end{cases} \tag{4.3.10}$$

From (4.3.7) we obtain the resistances in the network

$$R_i = \begin{cases} 0.26 & i = 1,2 \\ 0.13 & i = 3,4 \end{cases} \tag{4.3.11}$$

The flow picture obtained for the first experiment is shown in figure 4.2.15. In this case we apply a potential difference (i.e., potential gradient) between the points A and C in figure 4.3.26. This means that we have the resistance $R_1 + R_4$ connected in parallel with the resistance $R_2 + R_3$. Since in this case these resistances are equal, we expect the flow to be divided in half between the two branches of the network. However, just by looking at the flow picture (figure 4.2.15), it is obvious that the flow concentrates at the saddles in the x direction only, whereas in the y direction it is rather diffuse. The reason for this behavior is the local contrast we discussed in section 4.3.1. The conductivity at the saddle points $\mathbf{x}_1$ and $\mathbf{x}_2$ is much higher than the one of the flat regions surrounding these points, whereas the conductivity at the saddle points $\mathbf{x}_3$ and $\mathbf{x}_4$ is very close to the one of the background. As a result, we do not obtain a significant flow concentration at these saddle points and the asymptotic theory alone leads to significant errors in the problem. For this experiment we find that the flux through the deep saddles is 0.465 instead of the ideal 0.5, whereas the flux through the shallow saddles is only 0.25. Similar conclusions are drawn from the results of the two remaining experiments in the table 4.3.7 that consider different network connections.

We conclude therefore that in order to have a good approximation of the problem by the asymptotic network we need a large overall contrast (i.e., $\max(\sigma)/\min(\sigma)$) and the saddles should be deep enough. If this is not the case, the regions of diffuse flow play an important role in the problem and cannot be neglected.

4 Summary

In this chapter we have introduced and tested extensively a hybrid numerical method for solving conductivity problems in a heterogeneous medium with high contrast properties. The method combines analytical results of the asymptotic theory introduced in [54, 18] with the use of a finite difference numerical scheme, but other numerical schemes such as finite elements could also have been used. We carried out extensive numerical tests for different contrasts, different geometries and driving forces and showed that the hybrid method performs much better than standard ones, even the adaptive method of [7] where very fine meshes are used locally. We also show that the performance of the hybrid method is independent of the position of the source or sink in the flow region, except when they are situated very near a saddle point of the conductivity. The other methods have serious difficulties even when the source or sink are not so close to the region of high contrast. The hybrid method performs equally well for contrast of the conductivity ranging from 10^2 to 10^8. A good choice for the size of the inner box where the asymptotic solution is used is essential for good performance of the hybrid method. In all the computations that we carried out we found that the size prescribed in section 4.1.2 is quite appropriate. The computational cost of the hybrid method is low, hence its efficiency high, because we only discretize the part of the domain where the flow is diffuse and therefore well resolved by standard numerical schemes.

Chapter 5

Summary and future research

1 Summary

In this dissertation we studied direct and inverse problems for transport in media with strong spatial variability (high contrast) of the electric conductivity and dielectric permittivity.

In **chapter 2** we address the forward problem for conducting and dielectric media under static and time harmonic, low frequency excitation, respectively. We formulate the problem as a homogenization problem for Maxwell's equations and look at how high contrast affects overall transport behavior. We consider a quasistatic approximation so the equations are in terms of complex fields and the conductivity (impedance) is complex. The real part of the complex impedance describes the dissipative properties of the medium, so we call it resistance. The imaginary part describes the dielectric properties of the medium, so we call it capacitance. The effective resistance and capacitance of the material are given by saddle-type variational principles [22, 30], which we use extensively in our analysis.

By combining asymptotic and variational techniques, we have shown that the effective resistance and capacitance of a high contrast material can be approximated well by a resistor-capacitor (R-C) network. The network approximation comes from the current flow concentration, or channeling, that occurs in media with high contrast. The channels develop in the vicinity of saddle points of the resistance or capacitance of the material and the network elements are computed locally, around these saddle points. The connection between the network elements is given by the variational principles describing the effective transport properties of the medium. For purely resistive (capacitive) regions of the material, the network nodes correspond to local minima of the microscopic resistance (capacitance) and the branches are paths connecting two adjacent minima over a saddle point of the resistance (capacitance).

Thus, we can easily construct the resistor or capacitor networks that approximate the flow in resistive or capacitive regions of the high contrast medium. However, it is not clear how the resistive and capacitive networks are connected to each other in general. We understand the connection only in simple cases of layered media and a single possible region of weak flow concentration across interfaces separating resistive regions from capacitive ones. The difficulty in obtaining the R-C connection in general situations comes from the weak flow concentration across the boundary interfaces that leads to lower order terms in the variational formulation of the effective impedance of the material. However, we can use our methods to get upper and lower bounds for the effective resistance and capacitance that remain sharp in the high contrast limit but do not necessarily converge to each other. This will be considered in future research.

The network approximation was tested numerically through various experiments and shown to be accurate when the contrast of the material is of order 10^2 or higher. The analysis and numerical experiments are done for two-dimensional flow problems but the results can be extended easily to any number of dimensions [54].

In **chapter 3** we use the resistor network approximation of transport in conducting materials with a static excitation for imaging. The flow channeling that occurs in such media implies that the data measured at the boundary contains significant information about the approximating resistor network. The network accounts for the main part of the flow in the domain and neglects the low contrast features of the conductivity.

We introduce a high contrast *model* of the conductivity based on the resistor network theory that defines $\sigma(\mathbf{x})$ in terms of a few parameters in comparison with the number of unknown conductivities in a usual pixel by pixel discretization. The reduced dimension of the space of model parameters is equivalent to a regularization of the inverse problem that is well suited for high contrast. The resistor network identified in the first step of the algorithm is used as a reference conductivity in a second stage where we identify the low contrast features of $\sigma(\mathbf{x})$. This involves a linearization about the reference conductivity (resistor network) as is usually done in a Born approximation.

We assess the performance of the inversion algorithm through numerous experiments and show that it is remarkably successful in recovering high contrast conductivities in many situations. The high contrast modules used in our computations (3.3.2) are rigid in the sense that they do not allow different heights of the maxima of $\sigma(\mathbf{x})$ around a channel. However, even with this restriction, our numerical experiments show that for conductivities with uneven peaks the algorithm recovers successfully the channels and the location of the inhomogeneities. Very good results were also obtained in numerical experiments with discontinuous conductivities (i.e., inclusions). The algorithm recovered a smoothed version of the model with the correct orientation and location of the channels and inclusions. We are currently considering more flexible models of the high contrast conductivity in order to improve the resolution of the images we obtain.

In **chapter 4** we combine the analytical results of the asymptotic resistor network theory for static flow problems with standard numerical methods in a hybrid numerical method that solves conductivity problems in heterogeneous media with high contrast properties. The method applies to conductivities that have both high contrast and flat or nearly flat regions in the flow regime. We developed the hybrid method for the inverse problem (chapter 3) where an accurate forward solver is needed. We carried out extensive numerical tests for different contrasts, different geometries and driving forces and showed that the hybrid method performs much better than standard ones, even the adaptive method of [7] where very fine meshes are used locally. This is not surprising because a general purpose code cannot be expected to do as well as a specially designed method that works for a limited class of problems, like the hybrid method for high contrast media.

The use of the hybrid method is restricted to problems with high contrast of the conductivity that arise in a continuum manner, but the ideas presented in this dissertation can be generalized to any problem where an asymptotically exact solution is known. Our numerical computations show that the performance of the hybrid method is independent of the position of the source or sink in the flow region, except when they are situated very near a saddle point of the conductivity. The other methods have serious difficulties even when the source or sink are not so close to the region of high contrast. The hybrid method performs equally well for contrast of the conductivity ranging from 10^2 to 10^8. The size of the inner box where the asymptotic solution is used is essential for good performance of the hybrid method and the choice prescribed in §1.2 proved to be optimal in our computations. The computational cost of the hybrid method is low, hence its efficiency high, because we only discretize the part of the domain where the flow is diffuse and therefore well resolved by standard numerical schemes.

At present the hybrid method requires a lot of human input and cannot be used efficiently in numerical computations involved in inversion. However, the hybrid numerical method helped us test the high contrast behavior of the multigrid numerical solver PLTMG [7] that we used in all our inversion computations.

2 Plans for future research

Although this thesis contains a systematic treatment of both forward and inverse problems in high contrast media and has laid a theoretical basis for network approximations of transport in such media, there remain several issues to be explored. We now discuss some of these issues.

- Increase the flexibility and performance of the inversion algorithm presented in this thesis. At present, the inversion algorithm uses high contrast modules that are quite rigid in the sense that they require the peaks of the conductivity surrounding the channel to have the same height. We are exploring at present more general models in order to eliminate this deficiency. For example, we are using Gaussians to fit the maxima of the conductivity. While this model is more general than the one used in this thesis, the dynamics is more complicated and the problem will require more careful regularization.

- Carry out a careful study of imaging media with multiple channels of current flow. We do know how to handle situations where the channels of flow are far apart, but additional work has to be done for more general situations.
- Extend the imaging method to dielectric media with complex valued, high contrast impedance.
- Carry out an asymptotic high contrast analysis for transport in conductive media with magnetic boundary excitation (magnetic problem). Several numerical experiments show the formation of rotational currents and no flow concentration around the saddle points of the conductivity of the materials. Thus, the asymptotic analysis for the magnetic problem is expected to be quite different than the one for dielectric high contrast media that we have done up to now.
- Design, implementation and testing of imaging algorithms for high contrast conductive media and magnetic probes.
- Pursue a careful study of the connection between the resistor and capacitor networks in general situations. The study will involve carrying out the asymptotic analysis to lower order terms and looking carefully into other variational formulations of the effective parameters of the medium. Thus, variational principles of Dirichlet type (see A1) can give more insight into this problem. Also, significant information can come from the study of the dual forward problem that is formulated in terms of the scalar electric potential. The problem of obtaining bounds based on the resistive and capacitive subnetworks also needs to be studied.
- We are currently considering the asymptotic analysis and proofs of the resistor-capacitor approximation for flow in high contrast media with random structure [19].

- Automation of the hybrid numerical method. At present, the hybrid numerical method introduced in chapter 4 is implemented manually, that is, we must know beforehand the position of the saddle points, their orientation and curvatures which are needed for specifying the saddle boxes. We are now considering the design of a code that automates this process and possible modifications of the adaptive code PLTMG [7] that allows for high contrast. Also, we consider combining the asymptotic theory with finite element methods by using the electric potentials predicted by the theory as basis functions around the channels of flow in the domain. Moreover, we want to extend the hybrid method to time-harmonic problems and use the resistor-capacitor network theory for this purpose.

Appendix A

Variational principles

In this section we present some variational formulations for the complex conductivity problem which were derived by Cherkaev and Gibiansky [22] and Fannjiang and Papanicolaou [30], as well as an explanation for why we chose the variational principles (2.1.24) and (2.1.25).

Recall from section 2.1 that

$$\mathbf{E} = (\rho + iC)\mathbf{j} \tag{A.0.1}$$

where the current density $\mathbf{j}$ is expressed in terms of the magnetic field as $\mathbf{j} = \nabla \times \mathbf{H}$ and the electric field is the gradient of a scalar electric potential $\mathbf{E} = -\nabla\phi$. We can write the current density and the electric field as a sum of their real and imaginary parts

$$\begin{aligned} \mathbf{j} &= \mathbf{j}_R + i \cdot \mathbf{j}_I \\ \mathbf{E} &= \mathbf{E}_R + i \cdot \mathbf{E}_I \end{aligned} \tag{A.0.2}$$

The coefficients ρ and C are in general symmetric positive definite matrices which in the particular case of isotropic media can be written as a scalar times the identity matrix. With the decomposition (A.0.2), equation (A.0.1) can be rewritten as

$$\begin{cases} -\mathbf{E}_R = -\rho\mathbf{j}_R + C\mathbf{j}_I \\ \mathbf{E}_I = C\mathbf{j}_R + \rho\mathbf{j}_I \end{cases} \tag{A.0.3}$$

or

$$\begin{pmatrix} -\mathbf{E}_R \\ \mathbf{E}_I \end{pmatrix} = \begin{pmatrix} -\rho & C \\ C & \rho \end{pmatrix} \begin{pmatrix} \mathbf{j}_R \\ \mathbf{j}_I \end{pmatrix} = D_{JJ} \begin{pmatrix} \mathbf{j}_R \\ \mathbf{j}_I \end{pmatrix}. \tag{A.0.4}$$

By using the condition $\nabla \times \mathbf{E} = \mathbf{0}$ we obtain

$$\begin{aligned} \nabla \times (-\rho \mathbf{j}_R + C\mathbf{j}_I) &= 0 \\ \nabla \times (C\mathbf{j}_R + \rho \mathbf{j}_I) &= 0 \\ \mathbf{j}_R = \nabla \times \mathbf{H}_R, \quad \mathbf{j}_I &= \nabla \times \mathbf{H}_I \end{aligned} \tag{A.0.5}$$

which is exactly the system of equations (2.1.17). The matrix D_{JJ} is symmetric but it is not positive definite, therefore problem (A.0.4) has a saddle point variational formulation. If we require the current density $\mathbf{j}$ to have an average over the unit cell $<\mathbf{j}>= \mathbf{e}_R + i\mathbf{e}_I$ we obtain

$$\frac{1}{2}(\mathbf{e}_R, \ \ \mathbf{e}_I) \cdot \begin{pmatrix} -\overline{R} & \overline{C} \\ \overline{C} & \overline{R} \end{pmatrix} \begin{pmatrix} \mathbf{e}_R \\ \mathbf{e}_I \end{pmatrix} =$$

$$\min_{<\mathbf{j}_I>=\mathbf{e}_I} \max_{<\mathbf{j}_R>=\mathbf{e}_R} \int_\Omega \frac{1}{2}(\mathbf{j}_R, \ \ \mathbf{j}_I) \cdot \begin{pmatrix} -\rho & C \\ C & \rho \end{pmatrix} \begin{pmatrix} \mathbf{j}_R \\ \mathbf{j}_I \end{pmatrix} d\mathbf{x} = \tag{A.0.6}$$

$$\min_{<\mathbf{j}_I>=\mathbf{e}_I} \max_{<\mathbf{j}_R>=\mathbf{e}_R} \frac{1}{2}[- <\mathbf{j}_R \cdot \rho \mathbf{j}_R> +2 <\mathbf{j}_R \cdot C\mathbf{j}_I> + <\mathbf{j}_I \cdot \rho \mathbf{j}_I>].$$

Equation (A.0.3) can also be written as

$$\begin{pmatrix} \mathbf{E}_I \\ \mathbf{E}_R \end{pmatrix} = \begin{pmatrix} C & \rho \\ \rho & -C \end{pmatrix} \begin{pmatrix} \mathbf{j}_R \\ \mathbf{j}_I \end{pmatrix} \tag{A.0.7}$$

which has the variational formulation

$$\frac{1}{2}(\mathbf{e}_R, \ \ \mathbf{e}_I) \cdot \begin{pmatrix} \overline{C} & \overline{R} \\ \overline{R} & -\overline{C} \end{pmatrix} \begin{pmatrix} \mathbf{e}_R \\ \mathbf{e}_I \end{pmatrix} =$$

$$\min_{<\mathbf{j}_R>=\mathbf{e}_R} \max_{<\mathbf{j}_I>=\mathbf{e}_I} \int_\Omega \frac{1}{2}(\mathbf{j}_R, \ \ \mathbf{j}_I) \cdot \begin{pmatrix} C & \rho \\ \rho & -C \end{pmatrix} \begin{pmatrix} \mathbf{j}_R \\ \mathbf{j}_I \end{pmatrix} d\mathbf{x} = \tag{A.0.8}$$

$$\min_{<\mathbf{j}_R>=\mathbf{e}_R} \max_{<\mathbf{j}_I>=\mathbf{e}_I} \frac{1}{2}[<\mathbf{j}_R \cdot C\mathbf{j}_R> +2 <\mathbf{j}_R \cdot \rho \mathbf{j}_I> - <\mathbf{j}_I \cdot C\mathbf{j}_I>].$$

The variational principles (A.0.6) and (A.0.8) are equivalent to (2.1.24) and (2.1.25) when the current density is driven by a real force only (i.e., $\mathbf{e}_I = \mathbf{0}$). By choosing a real driving force we compute directly $\overline{R}$ and $\overline{C}$. If the driving force were complex we would only get a linear combination of the effective resistance and capacitive reactance. By applying a Legendre transformation to our problem we can also obtain variational principles of Dirichlet type. From (A.0.3) we solve for $\mathbf{E}_R$ and $\mathbf{j}_I$ in terms of $\mathbf{j}_R$ and $\mathbf{E}_I$ and obtain

$$\begin{pmatrix} -\mathbf{j}_I \\ \mathbf{E}_R \end{pmatrix} = \begin{pmatrix} \rho^{-1} & \rho^{-1}C \\ C\rho^{-1} & \rho + C\rho^{-1}C \end{pmatrix} \begin{pmatrix} \nabla\phi_I \\ \mathbf{j}_R \end{pmatrix} = D_{EJ} \begin{pmatrix} \nabla\phi_I \\ \mathbf{j}_R \end{pmatrix}. \tag{A.0.9}$$

The matrix D_{EJ} is symmetric and positive definite and this problem has a variational principle of Dirichlet type. The Euler equations equivalent to (A.0.9) are

$$\begin{aligned} \nabla\cdot(\rho^{-1}\nabla\phi_I + \rho^{-1}C\mathbf{j}_R) &= 0 \\ \nabla\times[C\rho^{-1}\nabla\phi_I + (\rho + C\rho^{-1}C)\mathbf{j}_R] &= 0 \\ \nabla\cdot\mathbf{j}_R &= 0 \end{aligned} \tag{A.0.10}$$

and they are associated with the variational principle

$$\tfrac{1}{2}(\mathbf{e}_1, \;\; \mathbf{e}_2)\cdot \begin{pmatrix} \overline{R}^{-1} & \overline{R}^{-1}C \\ \overline{CR}^{-1} & \overline{R} + \overline{CR}^{-1}\overline{C} \end{pmatrix} \begin{pmatrix} \mathbf{e}_1 \\ \mathbf{e}_2 \end{pmatrix} =$$

$$\min_{<\nabla\phi_I>=\mathbf{e}_1} \min_{<\mathbf{j}_R>=\mathbf{e}_2} \int_\Omega \tfrac{1}{2}(\nabla\phi_I, \;\; \mathbf{j}_R)\cdot \begin{pmatrix} \rho^{-1} & \rho^{-1}C \\ C\rho^{-1} & \rho + C\rho^{-1}C \end{pmatrix} \begin{pmatrix} \nabla\phi_I \\ \mathbf{j}_R \end{pmatrix} d\mathbf{x} =$$

$$\min_{\nabla\phi} \min_{\mathbf{j}} \tfrac{1}{2}[< \nabla\phi\cdot\rho^{-1}\nabla\phi > +2 < \nabla\phi\cdot\rho^{-1}C\mathbf{j} > + < \mathbf{j}\cdot(\rho + C\rho^{-1}C)\mathbf{j} >]. \tag{A.0.11}$$

In general min min variational principles are preferred to saddle point ones in obtaining bounds on the effective parameters and especially in numerical computations. However, in order to obtain sharp bounds we need a good estimate for the trial fields $\nabla\phi_I$ and $\mathbf{j}_R$. We found that the Euler equations (A.0.10) are difficult to use because they are in terms of both current and potential difference and the coefficients are nonlinear functions of the microscopic resistance and capacitance. The nonlinearity of the coefficients makes it hard to perform an asymptotic analysis of (A.0.10) for the logarithmic high contrast ρ and C we are considering. However, variational principles like (A.0.11) could still provide useful information and we intend to exploit them in future work. Even though in general it is difficult to work with saddle point variational principles, we found that they are very suitable for our particular problem. This is because an asymptotic analysis performed on the simpler system of Euler equations (A.0.5) can provide a good guess of the trial fields $\mathbf{j}_R$ and $\mathbf{j}_I$. For example, in order to get an upper bound on the effective resistance $\overline{R}$ from (A.0.6) we can use such a guess for the real part of the current. Then we are left with a single maximization problem. In general this problem could be difficult to solve but in our case the maximization is equivalent to the minimization occurring in the computation of the effective real conductivity of isotropic media for static fields. The later is a problem we can solve asymptotically (see section 2.2.2) and therefore we can obtain an upper bound on $\overline{R}$. A similar strategy is used in obtaining a lower bound on $\overline{R}$. We start with a guess provided by the asymptotic analysis for the imaginary current and then minimize over the real current. This procedure is used in the proofs we presented and works well for isotropic media and relatively simple geometries. For more complicated geometries it could well be that variational principles of Dirichlet type are more useful.

Appendix B

Spectral numerical method used in chapter2

In order to compute the effective impedance associated with the direct problem, we solve the system of differential equations

$$\begin{aligned} \nabla^{\perp} \cdot [(\rho + iC)(\mathbf{e}_1 + \nabla^{\perp} w)] = 0 \\ < \nabla^{\perp} w >= 0 \end{aligned} \tag{B.0.1}$$

Since the problem is periodic and defined on a square cell Ω, we use a Fourier Galerkin spectral method. In this approach the solution w is approximated by a truncated Fourier series

$$w(x, y) = \sum_{k_1=-\frac{N}{2}}^{\frac{N}{2}-1} \sum_{k_2=-\frac{N}{2}}^{\frac{N}{2}-1} \hat{w}_{k_1 k_2} e^{i(k_1 x + k_2 y)}, \tag{B.0.2}$$

where N is the number of orthogonal test functions in the expansion, and w is restricted to a uniform grid with N points in each direction. For simplicity we consider a square domain Ω with a 2π side, such that the wavenumbers k_i, i = 1,2 are integers. The position dependent coefficients ρ and C appearing in (B.0.1) have their own discrete Fourier expansion

$$\rho(x, y) + iC(x, y) = \sum_{k_1=-\frac{N}{2}}^{\frac{N}{2}-1} \sum_{k_2=-\frac{N}{2}}^{\frac{N}{2}-1} a_{k_1 k_2} e^{i(k_1 x + k_2 y)}. \tag{B.0.3}$$

If we substitute (B.0.2), and (B.0.3) in (B.0.1), and use the orthogonality of the test functions $e^{i(k_1 x + k_2 y)}$ we obtain the system of equations

$$\sum_{n=-\frac{N}{2}}^{\frac{N}{2}-1} \sum_{m=-\frac{N}{2}}^{\frac{N}{2}-1} \sum_{p+n=j} \sum_{k+m=s} [m(k+m) + n(p+n)] a_{pk} \hat{w}_{nm} = -isa_{js},$$

$$\forall j, s = -\frac{N}{2}, \ldots \frac{N}{2} - 1. \qquad \text{(B.0.4)}$$

The linear system of equations (B.0.4) can be rewritten in matrix form as

$$A\hat{\mathbf{w}} = \mathbf{b}, \qquad \text{(B.0.5)}$$

where the matrix A is complex, and has N^2 rows and columns, and the vector $\mathbf{w}$ contains the N^2 unknown Fourier coefficients. We mention that because of the convolution sums appearing in (B.0.4) the matrix A will be dense in general, and solving for the Fourier coefficients $\hat{w}_{ij}$ can become expensive. After obtaining the Fourier coefficients we perform an inverse FFT in order to find $w(\mathbf{x})$ which substituted in (2.1.19) gives the effective impedance $\overline{Z}$.

Bibliography

[1] Allen, A. and Santosa, F., 1991, *Stability and resolution analysis of a linearized problem in electrical impedance tomography*, Inverse Problems, **7**, pp. 515-533.

[2] Alessandrini, G., *Stable determination of conductivity by boundary measurements*, App. Anal., 27, 1988, pp. 153-172.

[3] Alumbaugh, D.L., *Iterative Electromagnetic Born Inversion Applied to Earth Conductivity Imaging*, Ph.D. thesis, Berkeley, 1993.

[4] Alumbaugh, D.L., Morrison, H. F., *Electromagnetic conductivity imaging with an iterative Born inversion*, IEEE Transactions on Geosciences and Remote Sensing, Vol. 31, No. 4, July, 1993, pp. 758-763.

[5] Alumbaugh, D.L. and Morrison, H.F., 1995, *Monitoring subsurface changes over time with cross-well electromagnetic tomography*, Geophysical Prospecting, **43**, pp. 873-902.

[6] Ambegaokar, V., Halperin, B. I., Langer, J. S., *Hopping Conductivity in Disordered Systems*, Phys. Rev. B, 4(8), 1971, pp. 2612-2620.

[7] Bank, E.R. *PLTMG: A Software Package for Solving Elliptic Partial Differential Equations*, SIAM, 1990.

[8] Banks, T.H. and Kunisch, K., 1989, *Estimation techniques for distributed parameter systems* (Boston Birkhaüser).

[9] Barber, D., Brown, B., *Recent developments in applied potential tomography-APT*, Information processing in medical imaging, Bacharach., S. ed., Nijhoff, Amsterdam, 1986, pp. 106-121.

[10] Batchelor, G.K., O'Brien, R.W., *Thermal or electrical conduction through a granular material*, Proc. R. Soc. London A, 1977, 355, pp. 313-333.

[11] Bensoussan, A., Lions, J.L., Papanicolaou, G.C., *Asymptotic analysis for periodic structures*, North-Holland, Amsterdam, 1978.

[12] Berlyand, L., Golden, K., *Exact result for the effective conductivity of a continuum percolation model*, Phys. Rev. B, vol. 50, no. 4, July, 1994, pp. 2114-2117.

[13] Berryman, J.G., *Stable iterative reconstruction algorithm for nonlinear traveltime tomography*, Inverse Problems, 6, 1990, pp. 21-42.

[14] Berryman, J.G., *Weighted least-squares criteria for seismic traveltime tomography*, IEEE Trans. Geosci. Remote Sensing, 27(3), 1989, pp. 302-309.

[15] Berryman, J.G., *Fermat's principle and nonlinear traveltime tomography*, Phys. Rev. Let., 62(25), 1989, pp. 2953-2956.

[16] Berryman, J.G., *Convexity properties of inverse problems with variational constraints*, J. of Franklin Institute, vol. 328, no. 1, 1991, pp. 1-13.

[17] Borcea, L., Papanicolaou, G.C., *Network approximation for transport properties of high contrast materials*, submitted SIAM Applied Mathematics, 1996.

[18] Borcea, L., Papanicolaou, G.C., *A hybrid numerical method for high contrast conductivity problems*, submitted J. Computational and Applied Math., 1996.

[19] Borcea, L., Papanicolaou, G.C., Wehr, J., *Network approximation for high contrast random conductivities*, in preparation.

[20] Borcea, L., Berryman, J.G., Papanicolaou, G.C., *High Contrast Impedance Tomography*, submitted Inverse Problems, 1996.

[21] Chandler R., Koplik J., Lerman K., Willemsen J.F., *Capillary displacement and percolation in porous media*, J. Fluid Mech., 1982, vol. 119, pp. 249-267.

[22] Cherkaev, A.V., Gibiansky, L.V., *Variational principles for complex conductivity, viscoelasticity, and similar problems in media with complex moduli*, J. Math. Phys., 35 (1), January, 1994, pp. 127-145.

[23] Curtis, E.B., Morrow, J.A., *Determining the resistors in a network*, SIAM J. Appl. Math., Vol. 50, No. 3, June 1990, pp. 931-941.

[24] Dagan, G., *Flow and Transport in Porous Formations*, Springer- Verlag, New York, 1989.

[25] Daily, W.D., A. Ramirez, D. LaBrecque and Nitao, J., 1992, *Electrical resistivity tomography of vadose water movement*, Water Resources Res. **28**, pp. 1429-1442.

[26] Dennis, J.E., Schnabel, R.B., *Numerical methods for unconstrained optimization and nonlinear equations*, SIAM, 1996.

[27] Dines, K.A., Lytle, R.J., *Analysis of electrical conductivity imaging*, Geophysics 46, 1981, pp. 1025-1036.

[28] Dykhne, A.M., *Conductivity of a two-dimensional two-phase system*, JETP 32, 1971, pp. 63-65.

[29] Ekeland, I., Teman, R., *Convex analysis and variational problems*, Studies in mathematics and its applications, vol. 1, 1976.

[30] Fannjiang, A., Papanicolaou, G.C., *Convection enhanced diffusion for periodic flows*, SIAM J. Appl. Math., 54, 1994, pp. 333-408.

[31] Fannjiang, A., Papanicolaou, G.C., *Convection enhanced diffusion for random flows*, submitted to Journal of Statistical Physics, 1996.

[32] Fletcher, R., 1987, *Practical methods of Optimization*, (New York: Wiley).

[33] Gibiansky, L.V., Milton, G.W., *On the effective viscoelastic moduli of two-phase media. Rigorous bounds on the complex bulk modulus*, Proc. R. Soc. London A, 1993, 440, pp. 163-188.

[34] Gill, P.E., Murray, W. and Wright, M.H., *Practical Optimization*, Academic Press, London, 1981.

[35] Golden, K.M., *Percolation models for porous media*, preprint 1995.

[36] Golden, K.M., Kozlov, S.M., *Critical path analysis of transport in highly disordered random media*, preprint 1995.

[37] Golden, K., Papanicolaou, G., *Bounds for effective parameters of multicomponent media by analytic continuation*, J. Stat. Phys. 40, 1985, pp. 655-668.

[38] Habashy, T.M., Groom, R.W., Spies, B.R., *Beyond the Born and Rytov Approximations: A nonlinear approach to Electromagnetic Scattering*, J. Geophysical Research, Vol. 98, No. B2, pp. 1759-1755, February, 1993.

[39] Halperin, B.I., *Remarks on percolation and transport in networks with a wide range of bond strengths*, Physica D, 38, 1989, pp. 179-183.

[40] Hashin, Z., Shtrikman, S., *A variational approach to the theory of the effective magnetic permeability of multiphase materials*, J. Appl. Phys. 33, 1962, pp. 3125-3131.

[41] Hestenes, M.R. and Stiefel, E., 1952, *Methods of conjugate gradients for solving linear systems*, J. Res. NBS **49**, pp. 409-436.

[42] Isakov, V., *Uniqueness and stability in multi-dimensional inverse problems*, Inverse Problems, 9, 1993, pp. 579-621.

[43] Ito, K. and Kunisch, K., 1990, *The augmented Lagrangian method for parameter estimation in elliptic systems*, SIAM J. Control **28**, 113–136.

[44] Jackson, J.D., *Classical Electrodynamics*, second ed., Wiley, New York, 1974.

[45] Jikov, V.V., Kozlov, S.M., Oleinik, O.A., *Homogenization of Differential Operators and Integral Functional*, Springer-Verlag, Berlin Heilderberg, 1994.

[46] Kaczmarz, S., 1937, Angenäherte Auflösung von Systemen linearer Gleichungen, *Bull. Acad. Polon. Sci. Lett.* **A**, pp. 355-357.

[47] Keller, J.B., *Conductivity of a Medium Containing a Dense Array of Perfectly Conducting Spheres or Cylinders or Nonconducting Cylinders*, J. Appl. Phys., 34 (4), 1963, pp. 991-993.

[48] Keller, J.B., *Effective conductivity of periodic composites composed of two very unequal conductors*, J. Math. Phys., 28 (10), 1987, pp. 2516-2520.

[49] Keller, J.B., *A Theorem on the Conductivity of a Composite Medium*, J. Math. Phys., 5(4), 1964, pp. 548-549.

[50] Kitanidis, P.K., *Quasilinear Geostatistical Theory for Inversing*, Water Resources Res., 31, 1995, pp. 2411-2419.

[51] Kohler, W., Papanicolaou, G.C., *Bounds for the effective conductivity of random media*, Springer Lecture Notes in Physics 154, 1982, pp. 111-130.

[52] Kohn, R., Vogelius, M., *Determining conductivity by boundary measurements*, Comm. Pure App. Math., 38, 1985, pp. 643-667.

[53] Koplik, J., *Creeping flow in two-dimensional networks*, J. Fluid Mech., 1982, Vol. 119, pp. 219-247.

[54] Kozlov, S.M., *Geometric aspects of averaging*, Russian Math. Surveys 44:2, 1989, pp. 91-144.

[55] *LAPACK User's Guide,* SIAM, 1992.

[56] Levenberg, K., 1944, *A method for the solution of certain non-linear problems in least squares*, Quart. Appl. Math. **2**, pp. 164-168.

[57] Lu, Shin-yee and Berryman, J.G., *Inverse Scattering, Seismic Traveltime Tomography, and Neural Networks*, Int. J. of Imaging Systems and Techn., Vol. 2, 1990, pp. 112-118.

[58] Mallat, S. and Zhang, Z., 1993, *Matching pursuit in a time-frequency dictionary*, IEEE Trans. Signal Processing, **41**, pp. 3397-3415.

[59] Marquardt, D.W., 1963, *An algorithm for least-squares estimation of nonlinear parameters*, SIAM J. Appl. Math., **11**, pp. 431-441.

[60] Marquardt, D.W., 1970, *Generalized inverses, ridge regression, biased linear estimation, and nonlinear estimation*, Technometrics, **12**, pp. 591-612.

[61] McCormick, S.F. and Wade, J.G., 1993, *Multigrid solution of a linearized, regularized least-squares problem in electrical impedance tomography*, Inverse Problems, **9**, pp. 697-713.

[62] Milton, G.W., *On characterizing the set of possible effective tensors of composites: The variational method and the translation method*, Communications on Pure and Applied Math., Vol XLIII, 1990, pp. 63-125.

[63] Mitchell, A.R., *Computational methods in partial differential equations*, J. Wiley, New York, 1969.

[64] Natterer, F., *The mathematics of computerized tomography*, John Wiley and Sons, 1986.

[65] Ramirez, A., Daily, D.W., LaBrecque, D., Owen, E. and Chesnut D., 1993, *Monitoring an underground steam injection process using electrical resistance tomography*, Water Resources Res., **29**, pp. 73-87.

[66] Rector, J.W., editor, *Geophysics*, Special Issue on Crosswell Methods, Vol. 60, No. 3, 1995.

[67] Santosa, F. and Vogelius., 1990, *A backprojection algorithm for electrical impedance imaging*, SIAM J. Appl. Math., **50**, pp. 216-243.

[68] Schwartz, L.M., Banavar, J.R., Halperin, B.I., *Biased-diffusion calculations of electrical transport in inhomogeneous continuum systems*, Physical review B, Vol. 40, 13, November 1989, pp. 9155-9161.

[69] Shah, C.B., Yortsos, Y.C., *The permeability of strongly-disordered systems*, Physics of Fluids, vol.8, no. 1, January 1996, pp. 280-282.

[70] Sylvester, J., Uhlmann, G., *A global uniqueness theorem for an inverse boundary value problem*, Ann. Math., 125, 1987, pp. 153-169.

[71] Sylvester, J., Uhlmann, G., *The Dirichlet to Neumann map and applications*, Inverse problems in partial differential equations, editors: Colton, D., Ewing, R., Rundell, W., SIAM, 1990, pp. 101-139.

[72] Tikhonov, A. and Arsénine, V., 1976, *Méthodes de Résolution de Problèmes Mal Posés*, Éditions Mir, Moscow.

[73] Yorkey, T.J., Webster, J.G. and Tompkins, W.J., *Comparing reconstruction algorithms for electrical impedance tomography*, IEEE Trans. Biomed. Engng., **34**, pp. 843-852, 1987.

[74] Zhou, Q., Becker, A., Morrison, H.F., *Audio-frequency electromagnetic tomography in 2-D*, Geophysics, 1993, pp. 482-495.